**The Dissertation Committee for Mo Yu certifies that this is the approved version of the following dissertation:**

# Probing giant-planet forming zones around Solar-like stars with CO

**Committee:**

---

**Adam Kraus, Supervisor**

---

**Neal J. Evans II, Co-Supervisor**

---

**Sarah Dodson-Robinson**

---

**Karen Willacy**

---

**John Lacy**

---

**Daniel Jaffe**

---

**Edwin Bergin**

**Probing giant-planet forming zones around Solar-like stars with CO**

by

**Mo Yu**

**Dissertation**
Presented to the Faculty of the Graduate School of
The University of Texas at Austin
in Partial Fulfillment
of the Requirements
for the degree of
**Doctor of Philosophy**

The University of Texas at Austin
August, 2017

**Probing giant-planet forming zones around Solar-like stars with CO**

Mo Yu, Ph.D.
The University of Texas at Austin, 2017

Supervisors: Adam Kraus, Neal J. Evans II

Protoplanetary disks are dusty disks around young stars where planets are formed. The evolution and composition of protoplanetary disks determine the time, environments and materials available for planet formation. However fundamental properties of protoplanetary disks such as mass, composition, and the angular momentum transfer mechanism are poorly constrained by observations.

In this dissertation, we discuss the thermal and chemical evolution of protoplanetary disks around Solar-type stars, and evaluate methods to measure two key parameters - disk mass and turbulent velocity in the framework of an evolving disk system. We first build a chemical evolution model based on an MRI-active disk around a Solar-type star, and discuss the chemical depletion of CO due to the formation of complex organic molecules (Chapter 2). We then investigate the challenges one faces when measuring disk masses with CO due to the chemical depletion of CO and optical depth effects (Chapter 3). We propose strategies to correct for the CO depletion effect and constrain the disk mass within factor of a few accuracy. We also investigate the possibility of constraining turbulent velocities with CO line profiles in Chapter 4. Peak-to-trough ratios of CO rotational lines have been proposed as a robust probe for turbulent velocity. However we show that the peak-to-trough ratio could vary by 25% due uncertainties in effects of CO depletion. One would underestimate the degree of turbulence if the chemical depletion of CO is not properly accounted for.

# Acknowledgements

This dissertation would not be possible without guidance and support from my advisors Neal Evans and Sarah Dodson-Robinson. They are advisors who helped me explore astronomy research and also mentors who guided me through my six years of journey in graduate school. They are brave explorers, generous teachers and lifelong learners. I appreciate and treasure everything they taught me and aspire to be like them one day.

I would like to thank my long-term collaborators Karen Willacy and Neal Turner, and my committee members Edwin Bergin, John Lacy, Daniel Jaffe, and Adam Kraus. I am grateful for many helpful discussions that happened around the office and in conferences all over the world, with Joel Green, Yao-Lun Yang, Kevin Gullicson, Jacob Simon, Karen Öberg, Ilse Cleeves, and Megan Ansdell.

I am grateful for having parents who encourage me to pursue my interests freely and achieve the best I can. I would like to thank my partner for being supportive of my career choices, especially during my last semester in grad school.

Grad school wouldnt have been such a good part of my life without friends and colleagues inside and outside the department. Thank you!

Mo Yu

*The University of Texas at Austin*
*August 2017*

# Contents

# List of Tables

# List of Figures

# Chapter One: Introduction

## 1.1 Time evolution of protoplanetary disks

Protoplanetary disks are accretion disks around newly formed stars where planets are formed (Williams & Cieza, 2011). The physical and chemical evolution of protoplanetary disks determine the time, conditions and materials available for planet formation. However, fundamental properties such as the mass, temperature, composition, and turbulent velocities of protoplanetary disks are poorly constrained observationally due to the lack of effective tracers.

Protoplanetary disks are natural by-products of the star formation process, and their properties and evolution are closely related to the evolution of the central star. During a few million years of a protoplanetary disk's life time, the central star evolves along the Hayashi track, shrinking and becoming less luminous. The disk therefore cools down due to less heating from the central star over time. Moreover, the disk dissipates due to angular momentum transfer - the inner part being accreted onto the central star, while the outer part spreads towards large radii. The evolution of temperature and density profiles along with sources of ionization control the chemical evolution. To properly understand the chemistry of protoplanetary disks, we need to study it from an evolutionary point of view.

Besides the thermal emission from the central star, protoplanetary disks are also exposed to UV, X-ray and cosmic rays. UV and X-ray radiation can come from both the central star and the surrounding environment, while cosmic rays act as a background radiation. Ionizations powered by X-ray and cosmic rays are crucial for chemical reactions in protoplanetary disks. Densities in protoplanetary disks are low enough for neutral-neutral reactions to be rare, so ion-neutral reactions are the dominant form of reactions in the gas phase.

## 1.2 Observations of protoplanetary disks

Gas makes up 99% of the disk mass, and solids such as dust grains make up the other 1%. The main constituent $H_2$ is not observable in typical disk environments, and disk masses have mostly been measured from continuum dust continuum emission in (sub)mm wavelengths. The conversion from dust mass to gas mass depends strongly on the grain size distribution. Dust grains can grow from $\mu$m size to larger sizes efficiently within the disk life time (Oliveira et al., 2010; Pérez et al., 2012; Birnstiel et al., 2011; Garaud et al., 2013); therefore one could be underestimating disk mass assuming a constant dust-to-gas ratio.

Another alternative is to measure the disk mass by observing gaseous molecules such as CO and HD. Three disk masses have been measured (Bergin et al., 2013; McClure et al., 2016) with HD observed by the *Herschel* space telescope, and the masses are in general greater than estimates from dust emission. Although the GREAT instrument on the far-IR observatory SOFIA[1] covers the frequency of the HD transition, it is not sensitive enough to observe HD in nearby disks.

In the absence of the capability to observe the HD $J = 1 \rightarrow 0$ transition in disks, CO has been the standard tracer of the gas mass because it is believed to have simple chemistry and to stay in the gas phase wherever $T > 20$ K in disks around Sunlike stars (Öberg et al., 2011b; Qi et al., 2013b). However recent surveys of disk mass (Ansdell et al., 2016) have found low gas mass and gas-to-dust ratios in nearby star formining regions, suggesting efficient depletion of gaseous CO molecules (Dutrey et al., 2003; Favre et al., 2013; Miotello et al., 2017; McClure et al., 2016), or dispersing of the gas components (e.g., Hollenbach et al., 2000; Alexander et al., 2014; Gorti et al., 2016).

Correcting for the joint effects of freeze-out and isotope-selective photodissociation still does not bring the estimated gas-to-dust ratios up to 100, according to the chemical models of Miotello et al. (2017). We investigate the chemical depletion of CO over a few million years of disk life time in Chapter 2 and evaluate the effect of CO depletion on measuring disk mass from CO in Chapter 3.

[1] https://www.sofia.usra.edu/

## 1.3 The angular momentum transport problem in protoplanetary disks

Another important property, the degree of turbulence, is poorly constrained observationally due to the lack of tracers. Keplerian disks threaded by weak magnetic fields such as protoplanetary disks are predicted to be unstable against the magneto-rotational instability (MRI; Balbus & Hawley, 1991, 1998; Hawley, 2001; Fromang & Nelson, 2006; Salmeron & Wardle, 2008). The MRI turbulence can act as the angular momentum transport mechanism that controls the dissipation time scale of the propoplanetary disks and the time available for planet formation. However, non-ideal MHD effects such as Ohmic resistivity, ambipolar diffusion and the Hall effect could potentially suppress the level of turbulence, resulting in the formation of magnetic dead zones. The turbulent properties affect the dust coagulation (e.g. Dominik & Tielens, 1997; Blum & Wurm, 2008; Birnstiel et al., 2010; Zsom et al., 2011) and fragmentation timescales (e.g. Brauer et al., 2008; Birnstiel et al., 2009; Güttler et al., 2010; Kothe et al., 2010; Beitz et al., 2011), and are therefore important for the formation of rocky planet cores.

The ratio of the peak line flux to the flux at the line center (peak-to-trough ratio) of CO has been proposed as a robust diagnostic of the MRI turbulence (Simon et al., 2015a). Flaherty et al. (2015a) estimated the degree of turbulence from CO observations of HD 163296 and found the turbulent speeds to be far below what fully-developed MRI turbulence would produce. However, Simon et al. (2015a) and Flaherty et al. (2015a) assumed a constant $CO/H_2$ ratio of $10^{-4}$ in locations where CO is not frozen-out or photo-dissociated. In a chemically evolving disk, the $CO/H_2$ ratio is a complex function of both radius and time, and CO abundance gradients may affect the peak-to-trough ratio of CO emission lines and therefore estimations of turbulent velocities.

In this dissertation, we discuss disk chemistry, measurements of disk mass, and turbulence in the framework of thermally and chemically evolving disks. We first build a chemical evolution model based on an MRI-active disk around a Solar-type star, and then we discuss the chemical depletion of CO due to the formation of complex organic molecules. We then look into challenges one faces when trying to measure disk masses with CO. Finally, we investigate the possibility of constraining

turbulent velocities with CO line profiles, pointing out complications and potential ways to overcome the problems.

# Chapter Two: Probing Planet Forming Zones with Rare CO Isotopologues [1]

The gas near the midplanes of planet-forming protostellar disks remains largely unprobed by observations due to the high optical depth of commonly observed molecules such as CO and $H_2O$. However, rotational emission lines from rare molecules may have optical depths near unity in the vertical direction, so that the lines are strong enough to be detected, yet remain transparent enough to trace the disk midplane. Here we present a chemical model of an evolving T-Tauri disk and predict the optical depths of rotational transitions of $^{12}C^{16}O$, $^{13}C^{16}O$, $^{12}C^{17}O$ and $^{12}C^{18}O$. The MRI-active disk is primarily heated by the central star due to the formation of the dead zone. CO does not freeze out in our modeled region within 70AU around a sunlike star. However, the abundance of CO decreases because of the formation of complex organic molecules (COM), producing an effect that can be misinterpreted as the "snow line". These results are robust to variations in our assumptions about the evolution of the gas to dust ratio. The optical depths of low-order rotational lines of $C^{17}O$ are around unity, making it possible to see into the disk midplane using $C^{17}O$. Combining observations with modeled $C^{17}O/H_2$ ratios, like those we provide, can yield estimates of protoplanetary disks' gas masses.

## 2.1 Introduction

The mass and surface density of the inner 30AU of protoplanetary disks are critical parameters that control disk evolution and planet formation. Disk masses are currently determined by (sub)millimeter observations of dust, because the optical depth of continuum emission is low at radii much larger than 10AU (Williams & Cieza, 2011). However, observations begin to lose sensitivity to grains as they grow beyond

[1]This chapter was published in Astrophysical Journal as Yu, M., Willacy, K., Dodson-Robinson, S. E., Turner, N. J., Evans, II, N. J. 2016, ApJ, 822, 53. Mo Yu was the leading author of the paper. Sarah Dodson-Robinson was my thesis advisor and the main supervisor for this work. Karen Willacy provided the chemistry code and contributed to the chemical model section of the paper. Neal J. Evans II and Neal Turner provided useful comments and other contributions.

the observing wavelength; millimeter wave observations may thus underestimate solid masses in the inner disk, where dust settling and higher densities lead to more rapid growth (Pérez et al., 2012).

On the other hand, commonly observed molecular lines often suffer from high optical depth, and are therefore unable to probe gas near the midplane. Molecules that are important mass contributors to outer Solar System objects, such as $H_2O$ and $NH_3$, freeze out very close to the central star from the perspective of observers $> 100$ pc away. Thus, gas phase lines are hard to observe and most do not probe the giant planet-forming region. Here we seek a molecule that can be used to probe the conditions in planet-forming midplanes with rotational transitions observable from the ground. It must be present in the gas phase, even in a cold disk, and be optically thin enough that the disk is transparent in its rotational line emission. CO is volatile enough not to freeze out within a few tens of AU of the central star, so is able to probe a large disk area. Ali-Dib et al. (2014b) even find that, like $H_2O$, CO may be an important planet-building molecule for ice giants. While rotational emission from $^{12}C^{16}O$ is optically thick due to the molecule's high abundance, rare isotopologues of CO may provide optically thin lines due to their low abundances (Miotello et al., 2014). If so, CO isotopologue observations could lay the foundation for empirically determining the mass available for gas giant formation in nearby disks.

A clue that overall disk masses may be much larger than the MMSN (minimum-mass solar nebula) came from Bergin et al. (2013), who measured the mass of TW Hya using the optically thin $J = 1 \rightarrow 0$ transition of HD with the Herschel Space Observatory. The 10Myr -old transitional disk is estimated to have a mass of $0.05\,M_\odot$, much heavier than the $0.01 M_\odot$ of the MMSN, and larger than many measurements estimated from dust emission. This study has demonstrated the importance of measuring gas mass directly. However, the HD $J = 1$ state has a high excitation energy of $E/k_b = 128.5$ K ($k_b$ is the Boltzmann constant), so the line intensity depends on not only the mass available but also the temperature of the gas. Moreover, this transition is not accessible from the ground. Since there is no far-infrared space mission available, this method cannot be generally applied in the near future.

Extrapolating from line intensities to total disk mass requires knowledge of both the abundances and the isotopic ratios in the molecules being observed. Abundances are not constant throughout the disk, as freezeout rate, UV intensity, and X-ray intensity all change with distance from the star. Some chemical reactions are isotope-

selective, so the isotope ratio in molecules is also a function of distance from the star. Miotello et al. (2014) have shown that the abundance ratio of rare isotopologues of CO to $^{12}C^{16}O$ (If not specified, CO means the most common isotopologue of CO - $^{12}C^{16}O$ - hereafter) can deviate from the atomic ratio significantly due to isotope-selective photodissociation; the extent of the effect depends on the strength of UV radiation and dust properties. Finally, disk temperature and density change over time, bringing changes in the molecular inventory as the disk evolves. Here we present chemical evolution models of protostellar disks to build a framework for translating observed fluxes into mass densities available for planet formation.

The disk model consists of three main components—the thermodynamic model, the chemical model, and the optical depth estimation. The workflow of the disk model is sketched in Fig. 2.1, and the structure of this paper follows the model workflow. The thermodynamic model (Section 2) calculates the evolution of the disk thermal structure for 3 Myr by adding the passive heating from the stellar irradiation to the viscous heating from the magnetorotational instability (MRI) turbulence (Balbus & Hawley, 1991). We construct 2D dust radiative transfer models with RADMC (Dullemond & Dominik, 2004) to calculate the passive heating, and adopt the viscous heating profile from an MRI-active disk model (Landry et al., 2013), which includes a viscosity prescription for accretion driven by MRI turbulence. The chemical model (Section 3) then uses the density and temperature profiles from the thermodynamic model as input to calculate the disk's chemical evolution for 3Myr . After analyzing chemical model results and discussing the model dependencies on initial molecular cloud abundances, uncertainties in reaction rates, and different grain evolution scenarios in section 4, we estimate optical depths of various rotational emission lines from CO isotopologues (Section 5), and calculate the optical depths contributed by dust at corresponding locations. Finally, we summarize the main results in section 6. A list of symbols and definitions used can be found in Table 2.1.

## 2.2 The Thermodynamic Model

The thermodynamic model provides density and temperature evolution profiles for both the chemical model and the optical depth calculation. Our thermodynamic model is built upon the 1 + 1D disk model by Landry et al. (2013), who calculated

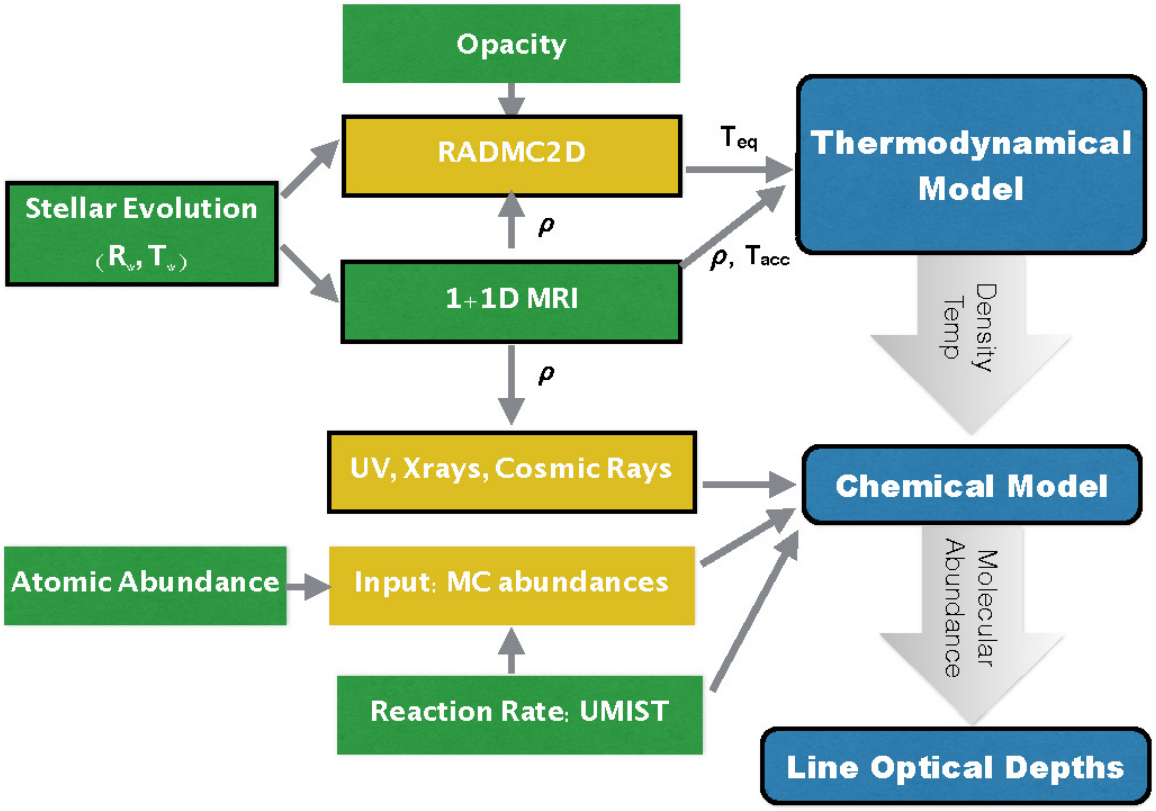


Figure 2.1: Workflow of our disk modelBlue boxes show three major components of our disk model. Green boxes show the model inputs taken directly from the literature, and yellow boxes are showing intermediate results computed in our study. Quantities in boxes with black borders evolve as a function of time, and the quantities in boxes without borders do not change over time.The arrows and variables next to the arrows are showing how information is passed between different model components.

the structure and evolution of a disk with $0.015\,M_{\odot}$ within 70AU of the star. The central star follows the evolutionary track of a $0.95\,M_{\odot}$ star (D'Antona & Mazzitelli, 1994) from 0.1Myr ($T_{\star} = 4600K$, and $R_{\star} = 5.5\,R_{\odot}$), roughly the beginning of the T-Tauri phase (Dunham & Vorobyov, 2012), to 3Myr ($T_{\star} = 4500K$, and $R_{\star} = 1.5\,R_{\odot}$). Landry et al. (2013) followed the viscous evolution of the inner 70AU of the disk. Because our goal is to probe the giant planet-forming regions, we focus our study on the inner 70AU of the disk.

The disk is heated passively by stellar irradiation, and actively by viscous heating due to accretion. In order to determine the degree of viscous heating, Landry

Table 2.1: A summary of parameters and definitions of variables

| Symbol | Definition or Value |
|---|---|
| ISRF | Interstellar radiation field |
| | $1ISRF = 1.6 \times 10^{-3} ergs^{-1}cm^{-2}$ for the ionizing UV radiation |
| COM | Complex organic molecules |
| MRI | Magneto-rotational instability |
| Stellar mass | $0.95\,M_\odot$, we follow the stellar evolution from 0.1Myr ($T_\star = 4600K$, and |
| | $R_\star = 5.5\,R_\odot$), to 3Myr ($T_\star = 4500K$, and $R_\star = 1.5\,R_\odot$). |
| Disk mass | $0.015\,M_\odot$ within 70AU from the central star |
| $n_{H_2}$ | number density of hydrogen molecules |
| $f_H$ | 0.735, mass fraction of hydrogen |
| Abundance | number density with respect to the number density of hydrogen nuclei |
| - A(B) | $(n_H + 2n_{H_2})$. A(B) stands for A$\times 10^B$ |
| T | disk temperature (same for dust and gas) |
| $T_{eq}$ | equilibrium temperature contributed by stellar irradiation |
| $T_{acc}$ | accretion temperature contributed by the MRI turbulence |
| $\zeta_{abs}$ | $6 \times 10^{-12}$ s$^{-1}$, ionization rate for direct x-ray absorption |
| $\zeta_{sca}$ | $10^{-15}$ s$^{-1}$, ionization rate for scattered x-ray photons |
| $L_{X,29}$ | 20, stellar X-ray luminosity in units of $10^{29}\,ergs^{-1}$ |
| $\Sigma_{cr}$ | 96 gcm$^{-2}$, characteristic column density of attenuation for cosmic rays |
| $\zeta_{cr}$ | cosmic ray ionization rate, $1.2 \times 10^{-17}$ s$^{-1}$ for $H_2$ molecules when calculating the reactions lead by cosmic ray induced photons, the total ionization rate is taken as $1.3 \times 10^{-17}$ s$^{-1}$. |

et al. (2013) evaluated whether MRI is present or not in each individual grid cell by considering both Ohmic resistivities and ambipolar diffusion. The MRI is shut down by Ohmic resistivity on the midplane, forming a deadzone extending to about 16AU. The disk has an MRI active layer near the surface, which provides an accretion rate of $10^{-9}\,M_\odot yr^{-1}$ even when a dead zone is present. However, unlike models with assumed uniform turbulent efficiency [with a constant $\alpha$ parameter, where viscosity $\nu = \alpha c_s H$, $c_s$ is the sound speed, and $H$ is the scale height; Shakura & Sunyaev (1973)], heating contributed by MRI (extracted from the energy of shear flow) only contributes slightly to the total heat budget of the disk because the power is deposited in the disk atmosphere at low optical depths.

Landry et al. (2013) calculated the heating from stellar irradiation in a 1 + 1D geometry using Rosseland mean opacities. Following Chiang & Goldreich (1997), Landry et al. (2013) considered stellar radiation entering the disk at a grazing angle, heating up the disk surface. Reprocessed stellar flux then traveled vertically from the

disk surface to the midplane. However, long-wavelength radiation emitted by dust grains at the disk surface should travel unimpeded to the midplane, causing heating that is not captured by using Rosseland mean opacities. By assuming that heating propagates only vertically from the heated surface, one also neglects the heat transfer in the radial direction within the disk, which can be important when the wavelength of the re-emitted light is long enough to allow radial propagation. One therefore underestimates the disk temperature by using a 1 + 1D geometry and Rosseland mean opacities.

The stellar irradiation cannot heat the disk enough to ionize the disk interior, so the 1 + 1D approximation with Rosseland mean opacity in Landry et al. (2013) was useful to calculate ionization, making the disk evolution model tractable. However, the missing heating can be crucial for the disk chemistry. We improved the treatment of the stellar irradiation by including 2D dust radiative transfer models built with the publicly available code RADMC (Dullemond & Dominik, 2004). We then calculated the total temperature by taking a flux-weighted sum of the accretion temperature ($T_{acc}$) calculated from the MRI model and the equilibrium temperature ($T_{eq}$) from stellar irradiation calculated from the 2D dust radiative transfer model at every point of the disk (as demonstrated in the upper half of Fig. 2.1.):

$$T^4 = T_{eq}^4 + T_{acc}^4, \tag{2.1}$$

The 2D dust radiative transfer models are set up with gas density profiles calculated by Landry et al. (2013) and a constant gas/solid ratio throughout the disk. The main focus of Landry et al. (2013) was to study the mass transport. The disk is truncated at about two scale heights above the midplane. The model thus includes the majority of the disk mass, but the dust above the original disk surface in Landry et al. (2013) could affect disk thermal properties by absorbing the stellar radiation. We therefore extrapolate the density profile vertically with Gaussian distributions down to a background density of $10^{-26} g\ cm^{-3}$ as input for the radiative transfer calculation.

Landry et al. (2013) found that if the mean grain size is as small as 0.1$\mu$m, the MRI shuts down completely. If the MRI drives accretion in the T-Tauri phase, some grain growth must have occurred, consistent with the findings of Oliveira et al. (2010). (See Gressel et al. (2015) for updated models suggesting that accretion is driven by winds, not MRI.) Evidence for rapid growth of solids in disks has been accumulating

in the following ways: direct evidence from long-wavelength observations Isella et al. (2010), Guilloteau et al. (2011), Banzatti et al. (2011), Pérez et al. (2012), Pérez et al. (2015), and Tazzari et al. (2015); observations of forming planets in the LkHa 15 disk by Kraus & Ireland (2012); and the HL Tau images from the ALMA Partnership et al. (2015), which show gaps possibly sculpted by forming planets or resonances with planets.

The wavelength-dependent dust opacities that we use are taken from the website[2], which provides models whose Rosseland and Planck mean opacities are described by Semenov et al. (2003), who updated earlier models by Henning & Stognienko (1996) for dust in protoplanetary disks. The available dust models include those with different assumptions about the iron mixture in the silicates, different models of grain growth, and different grain topologies. The dust grains are aggregated from "sub-grains, which themselves follow an MRN distribution extended up to 5$\mu$m (Mathis et al., 1977; Pollack et al., 1985). The dust model that we use assumes a "normal" mix of iron [Fe/(Fe+Mg) = 0.3] and that grain growth has occurred through particle cluster aggregation (PCA in the nomenclature of Semenov), which leads to roughly spherical grains. We use the multishell spheres topology and take the models for temperatures up to 155 K, in which ices and volatile organics are retained. Figure 2.2 shows the opacity per gram of gas versus wavelength for the adopted dust properties. There are a number of resonances and a relatively slowly declining opacity out to a wavelength of about 1.5 mm, beyond which the opacity declines rapidly. The opacities are given per gram of gas.

In our standard model, the dust has already grown and aggregated at the start of disk evolution - 0.1Myr after the formation of the central star. We further assume that 90% of the dust has grown to still larger sizes (pebbles, rocks, etc.), which we no longer describe as dust. This further growth decreases the grain surface area for chemical reactions and makes these solids essentially invisible even to millimeter wavelength observations (Birnstiel et al., 2011; Garaud et al., 2013). Consequently, we take a gas to dust ratio of 1000, so we divide the opacities from Semenov et al. (2003) by 10. In this model, there is a constant replenishment of dust by collisions between larger objects and the size distribution of dust does not evolve. We consider a different model for grain evolution as a variation of our standard assumptions in

[2]http://www.mpia.de/homes/henning/Dust_opacities/Opacities/opacities.html

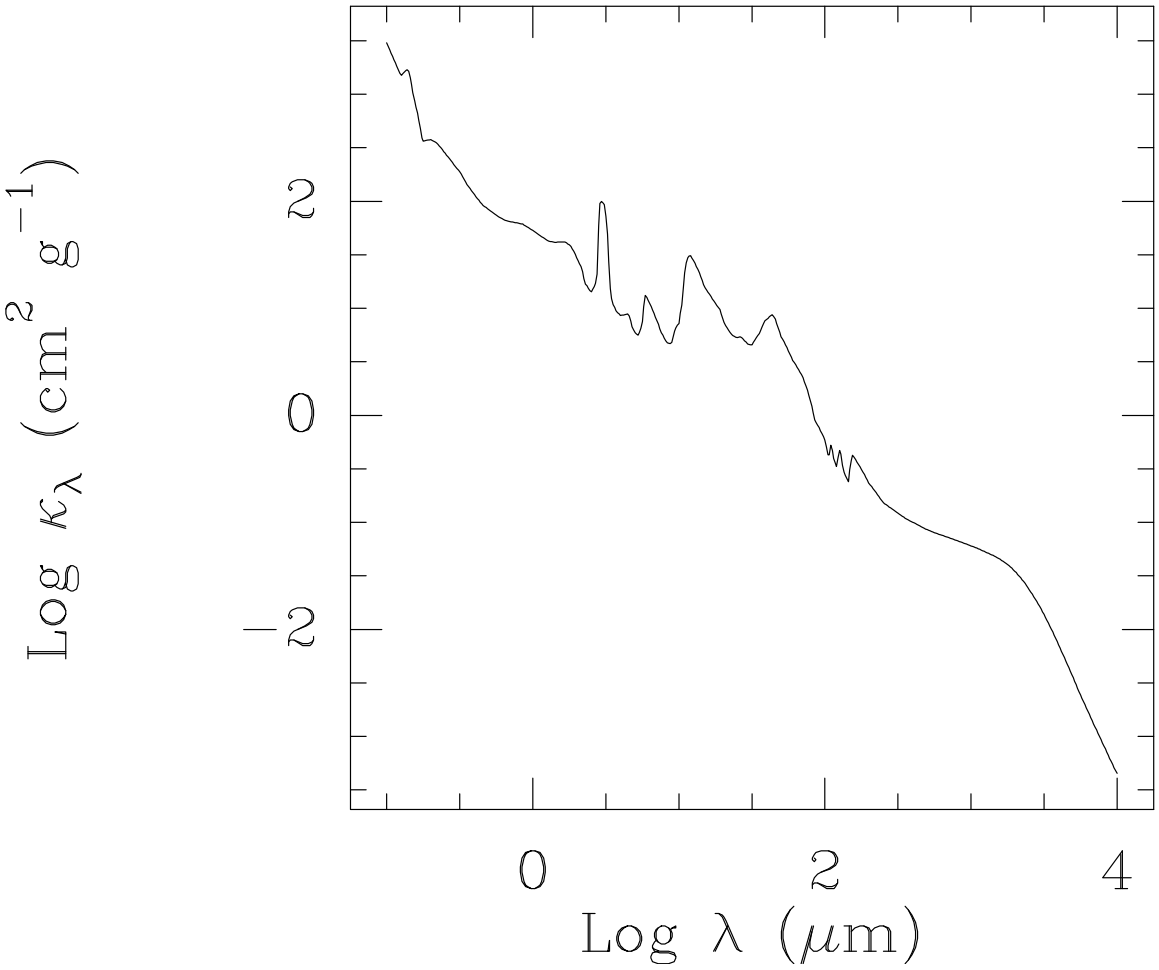


Figure 2.2: Opacity as a function of wavelength for the 5-layer multishell grain model of Semenov et al. (2003). The grain temperature used for this plot is 155 K.

§2.4.5.3.

The temperature color coded plots (at the beginning and end of the evolution) with $T_{eq}$ computed from the 2D dust radiative transfer model are shown in the upper panels of Fig. 2.3. In both cases, the temperature is the highest on the disk surface due to the heating from the central star, and gradually decreases at larger radius and into the disk interior. The temperature almost everywhere in the disk decreases due to the star evolving down the Hayashi track ($L_\star$ decreases from $12.1\,L_\odot$ to $0.8\,L_\odot$) and the flattening of the disk itself (cf. the top two panels in Fig. 2.3). The accretion heating ($T_{acc}$) contributed by the MRI turbulence is shown in the lower left panel of Fig. 2.3. Accretion heating contributes less then 3K in the majority of the disk,

rising to about 4K within 2AU from the central star.

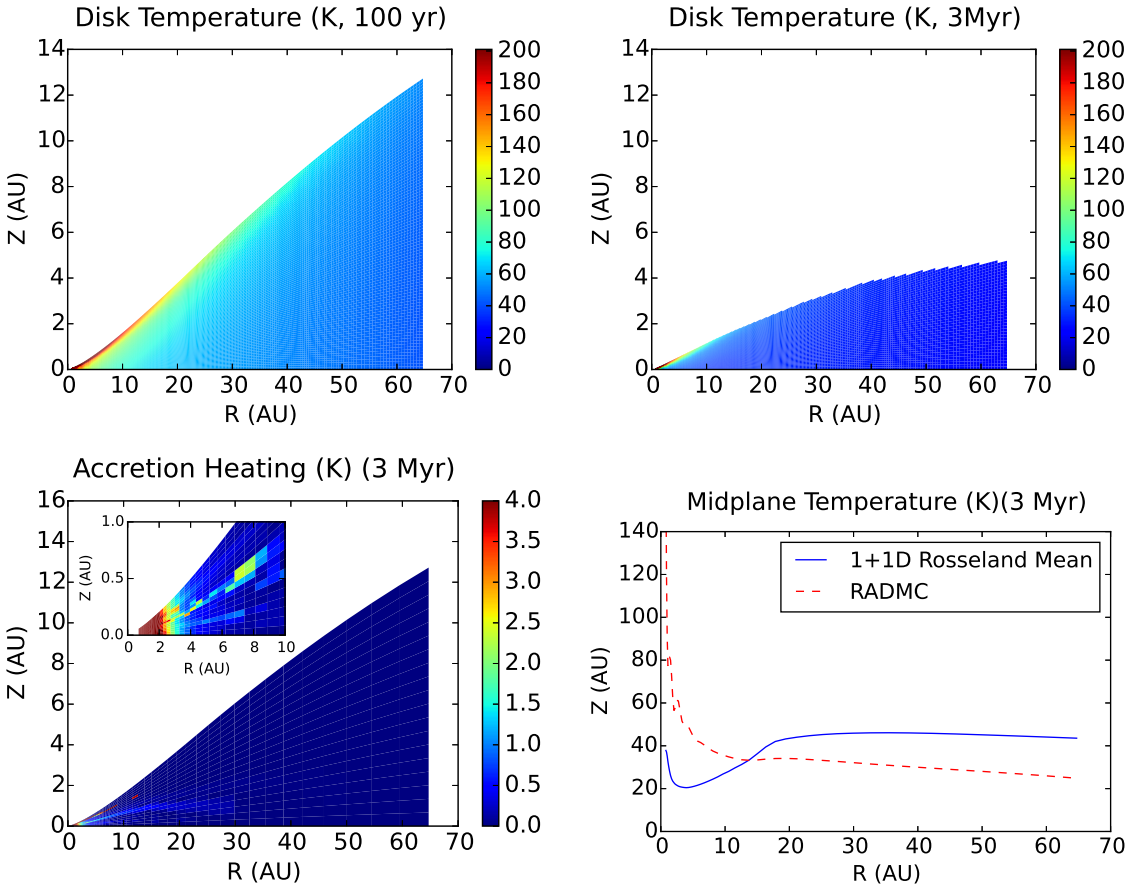


Figure 2.3: Upper left panel: Disk temperature (100yr) as a function of the radial distance to the central star (R) and height above the disk midplane (Z); Upper right panel: Disk temperature (3Myr); Lower left panel: Accretion heating ($T_{acc}$) contributed by the MRI turbulence (3Myr); The patches on the three color coded plots are interpolation artifacts, although the "arc" of light blue at $\sim$ 1AU above the midplane going from $5-30$ AU is real heating due to the MRI turbulence. Lower right panel: A comparison of the midplane temperature (Teq only) computed by RADMC and the 1+1D model with Rosseland mean opacities (3Myr). The $1+1$D model does not capture the heating contributed by longer wavelength radiation and underestimates the disk temperature in the inner 20AU. This effect is more severe at smaller radius due to larger optical depth, resulting in a lower temperature at smaller radius on the disk midplane - even though its surface temperature is higher.

We compare the midplane temperature with $T_{eq}$ computed from the $1+1$D model after 3Myr years of evolution in Landry et al. (2013) and the one computed from the

2D dust radiative transfer model in the lower right panel of Fig. 2.3. The temperature is much higher in the 2D model in the inner 20AU. The $1+1$D model misses heating in the inner part of the disk where the optical depth is larger, and therefore produces artificially lower temperature on the midplane closer to the central star. For example, the Rosseland mean optical depth is $\sim 12$ at 5 AU, but $\sim 4$ at 15 AU, so 5 AU is more severely affected—even though its surface temperature is higher. Moreover, once the temperature is down to $\sim 50$ K, the black-body radiation re-emitted from dust peaks at far-infrared wavelengths. The mean free path is a significant fraction of the scale height and the assumptions used to justify using Rosseland mean opacity breaks down.

Our treatment of temperature is not ideal in the sense that the vertical density structure and the temperature structure are not calculated consistently. However, as an experiment we artificially increased the scale height everywhere in the disk by 20 percent and did not find significant changes to the midplane temperature. We also assume the gas and dust are well mixed and have the same temperature in this paper, which is a valid assumption except for the very surface of the disk. Since the purpose of this project is to find an optical depth in the vertical direction and we mainly focus on the disk midplane where most of the disk mass resides, the combined accretion and passive heating models, assuming the same temperature for the gas and dust, meet our needs.

In the next sections, we describe our standard model and results. Then we describe two variations in the chemistry and one variation in the model of dust evolution.

## 2.3 Chemical model

The disk temperature and density evolution described in Section 2.2 allow us to compute the chemical evolution of the disk.

We also need initial chemical abundances, which we obtain from a simplified model of the molecular cloud.

We construct chemical evolution models including C, H, O, N, and different C and O isotopes based on the UMIST database RATE06 (Woodall et al., 2007), and follow the chemistry of 588 species, 414 gas-phase and 174 ices. The reaction network contains 13116 reactions, including gas-phase reactions, grain-surface reactions,

freezeout, thermal desorption, and reactions triggered by UV, X-rays and cosmic rays, such as isotope-selective photodissociation. The carbon isotopic chemistry network was developed by Woods & Willacy (2009) and was extended to include oxygen isotopes for this work.

We calculate the chemical evolution at each grid point independently. By doing this, we assume that the radial and vertical motions of gas and dust are slow compared to chemical reaction timescales, and that mixing is not important in determining the chemistry. This is a valid assumption for gas-grain reactions or grain surface reactions due to their short reaction timescale, but might not work as well for gas-phase reactions. However, given that turbulence in the inner 15 AU is restricted to the disk surface, we do not expect vertical mixing to contribute much to disk chemistry.

In order to calculate the chemical evolution over a 3Myr lifetime, we use an extension of the computationally efficient rate-equation method to compute reaction rates for grain-surface reactions under the "mean field" approximation (as used by Dodson-Robinson et al. 2009). Rate equations neglect the stochastic variation of abundances on different grains and are not appropriate when the number of reacting particles per grain is less than one. We modify our reaction rates following the method of Garrod & Pauly (2011), which considers the competition between thermal hopping of mobile species and reactions on the grain surfaces. We assume that only atoms and simple hydrides are mobile on the grains. Our treatment of gas phase reactions, freezeout, and thermal desorption is similar to that of Dodson-Robinson et al. (2009). After describing the molecular cloud preprocessing model in section 2.3.1, we focus the rest of this section on the treatment of photochemical and cosmic-ray reactions, which are new to this work.

### 2.3.1 Preprocessing in the molecular cloud

We model the chemical evolution in the molecular cloud stage to derive input abundances for the protoplanetary disk models.

The input abundances are listed in Table 2.2 (Graedel et al., 1982). Throughout this paper, abundances are presented as the number density normalized to the number density of hydrogen nuclei, $n_x/(n_H + 2n_{H_2})$.

The molecular cloud model is run for 1 Myr with a density of $2 \times 10^4$ cm$^{-3}$, at a temperature of 10K and with a visual extinction of 10 magnitudes.

The abundances at the end of the molecular cloud phase are given in Table 2.5. The $^{12}C/^{13}C$ is $\sim$ 46 in CO gas, $\sim$ 63 in CO ice and $\sim$ 58 in $CO_2$ ice at the end of the molecular cloud model – all lower than the initial elemental $^{12}C/^{13}C$ ratio. The reduction is caused by the preferential formation of heavier isotopomers of CO arising from the small energy different in the ion exchange reaction.

$$^{13}C^{+} + CO \leftrightarrow ^{13}CO + C^{+} + 35K. \tag{2.2}$$

$^{13}CO$ has a lower ground-state vibrational energy due to its slightly larger mass compared to CO, and is therefore more energetically favorable. At 10 K Equation 2.2 dominates the carbon fractionation, leading to lower $^{12}CO/^{13}CO$ than the elemental $^{12}C/^{13}C$ ratio (see also Visser et al. 2009a, Langer & Penzias 1993). In other molecules, such as $CH_4$ ice, the opposite effect is seen, with enhanced abundances of condensed $^{12}C$ leading to higher $^{12}CH_4/^{13}CH_4$ ratios in the ice.

Table 2.2: Input abundances of the molecular cloud model

| Species | Abundance [1,2] | Element | Abundance |
|---|---|---|---|
| H | 1.00 (-2) | He | 1.40 (-1) |
| $C^+$ | 7.21 (-5) | $^{13}C^+$ | 9.34 (-7) |
| O | 1.76 (-4) | $^{18}O$ | 3.51 (-7) |
| $^{17}O$ | 7.64 (-8) | N | 2.14 (-5) |
| $Si^+$ | 3.00 (-9) | | |

[1] Number density with respect to the number density of hydrogen nuclei ($n_H + 2n_{H_2}$). The abundances are taken from Graedel et al. (1982).
[2] A(B) stands for $A \times 10^B$

### 2.3.2 UV ionization, photodissociation and photodesorption

In addition to ionizing and dissociating gas phase species, UV photons also desorb molecules from grain mantles. The UV flux generated by a young star has been observed by France et al. (2014) who found a median value of 1000 ISRF (1 ISRF = $1.6 \times 10^{-3}$ ergs$^{-1}$ cm$^{-2}$; Habing (1968)) at 100 AU. Theoretical studies of Alexander et al. (2006) suggest a UV flux of $\sim$ 50 ISRF at 100 AU is required to drive photoevaporation of the disk. We choose a UV flux between these two values of 500 ISRF at 100 AU.

The UV field is attenuated by the disk and the resulting visual extinction can be related to the column density by

$$A_V(r,z) = 5.2 \times 10^{-22} \times \frac{f_H \Sigma_r(r,z)}{2m_H}, \tag{2.3}$$

where $f_H = 0.735$ is the mass fraction of hydrogen in the Sun (Grevesse & Sauval, 1998), and $\Sigma_r(r,z)$ is the horizontal column density integrated from the inner edge of the disk.

For photodesorption we adopt the reaction rate of Hollenbach et al. (2009)

$$k(r,z) = F(r,z) \times 10^8 \times (\pi a^2) \times Y, \tag{2.4}$$

where F(r,z) is the UV flux in ISRF, $\pi a^2$ is the grain cross-section and Y is the photodesorption yield. The average grain radius $a$ is taken to be $1\mu$m, and $Y$ is assumed to be $10^{-3}$ for all molecules (based on laboratory measurements of $H_2O$ photodesorption by Ly$\alpha$ photons (Westley et al. 1995a, b).

For the self-shielding of CO and $H_2$ we use the method of van Dishoeck & Black (1988) and Lee et al. (1996) respectively.

### 2.3.3 X-ray photoionization

We follow the X-ray ionization prescription of Bai & Goodman (2009), using a value of the ionization rate for direct absorption of X-rays, $\zeta_{abs} = 6$ x $10^{-12}$ s$^{-1}$, and for scattered photons, $\zeta_{sca} = 10^{-15}$ s$^{-1}$ (Igea & Glassgold, 1999). We assume a stellar X-ray luminosity $L_X = 20 \times 10^{29}$ erg s$^{-1}$ based on the median observed value from a Chandra survey of solar mass young stars in the Orion Nebula (Garmire et al., 2000). Similar values have also been observed in the Taurus-Auriga complex by Telleschi et al. (2007) and Robrade et al. (2014). The X-ray ionization rate is assumed to be the same for all reactions because of the lack of laboratory measurements.

### 2.3.4 Cosmic Rays

Cosmic rays can ionize and dissociate molecules in the gas directly, or by producing secondary photons (Gredel et al., 1989). The intensity of cosmic rays decreases exponentially with a characteristic attenuation depth of 96 g cm$^{-2}$ (Umebayashi & Nakano, 1981, 2009). The large penetration depth means that our model disk is

transparent to cosmic rays outside of 4 AU at the beginning of the T Tauri phase and outside of 3 AU at the end of 3Myr evolution. Cosmic ray reaction rates are taken from UMIST06 with an assumed cosmic ray ionization rate of $1.3 \times 10^{-17}$ s$^{-1}$.

### 2.3.5 A summary of ionization processes

Ionization rates contributed by the above three ionizing sources are shown in Fig. 2.4. The upper left panel shows an order-of-magnitude estimate of the UV ionization rate based on the $H_2O$ molecule, which is the molecule most commonly ionized by UV. The ionization rate decreases very rapidly due to the small penetration depth of UV photons, and it is negligible except for the very surface layer of the disk. X-rays are able to reach most of the disk except for the inner 10AU near the disk midplane (shown in the upper right panel in Fig. 2.4). They provide ionization rates of $10^{-14}$ s$^{-1}$ to $10^{-13}$ s$^{-1}$ near the disk surface, and a modest ionization rate around $10^{-17}$ s$^{-1}$ in the disk interior due to scattering. In the lower left panel, we show the cosmic-ray ionization rate of $H_2$, the most common cosmic-ray reaction partner. Cosmic rays provide a steady ionization rate around $10^{-17}$ s$^{-1}$ throughout the disk. The fractional contribution of X-ray ionization is plotted in the lower right panel of Fig. 2.4. Roughly speaking, X-rays dominate the ionization rate above one scale height of the disk where the vertical column density is less than a few g cm$^{-2}$, and the cosmic ray ionization dominates the disk interior within one scale height of the midplane. Cosmic ray-induced photons are abundant enough to cause ionization and photodissociation throughout the disk due to the efficient penetration of cosmic rays. Ionization rates due to cosmic ray-induced photons are different for each reactant and are not shown in Fig. 2.4. However, cosmic ray-induced photons are important contributors to the chemical evolution.

Cleeves et al. (2013a) showed that stellar winds can power a "T-Tauriosphere that shields the disk from external cosmic rays, leading to cosmic ray ionization rates of $10^{-18}$ s$^{-1}$ or lower. A decreased cosmic-ray flux would reduce the rates of reactions with both cosmic rays and cosmic ray-induced photons. On the other hand, the decay of shortlived radionuclides (SLRs) such as $^{26}$Al can provide an ionization rate on the order of $10^{-19}$ s$^{-1}$ to $10^{-18}$ s$^{-1}$ (Cleeves et al., 2013b), which may help to drive the chemistry in the disk interior. Since our chemical evolution models are computationally expensive, we do not explore different values of ionization rates.

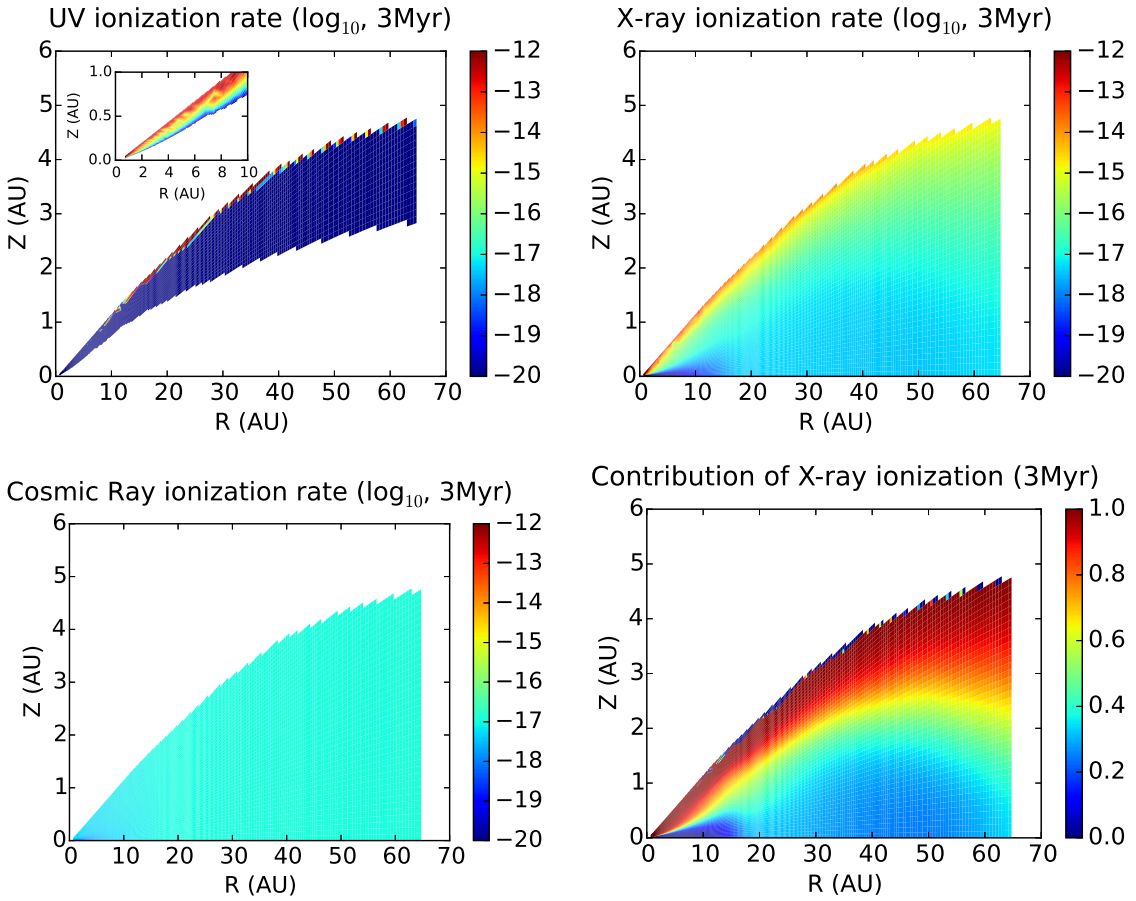


Figure 2.4: Estimated ionization rates contributed by various mechanisms at the end of our disk evolution. Upper left panel: UV ionization rate (an order of magnitude estimation for the $H_2O$ molecule, the ionization rate in the disk interior is lower than $10^{-20}s^{-1}$, and therefore does not show up in the plot.); Upper right panel: X-ray ionization; Lower left panel: cosmic ray ionization (an order of magnitude estimation considering only the $H_2$ molecule); Lower right panel: fraction contributed by X-ray ionization. X-ray ionization dominates at z/r $>$ 0.1, and cosmic rays account for most of the ionization for z/r $<$ 0.1, where the UV and X-ray radiation from the central star are sufficiently attenuated.

## 2.4 Chemical model results

The results of our chemical model give the abundances of CO isotopologues that we need for the optical depth calculation. First, we discuss the ice line locations for different volatiles (Section 2.4.1). Knowing the ice line locations is important for interpreting observed radial abundance gradients. Second, we discuss the active

reaction network involving carbon-bearing molecules, which causes the CO abundance to change with both radius and time (Section 2.4.2). In Section 2.4.3, we demonstrate that dissociation of CO and subsequent formation of complex organic molecules (COM) can produce CO depletion that mimics an ice line. In Section 2.4.4, we assess how computational limits on the number of species in our reaction network impact our COM abundances. We discuss our model's dependence on initial cloud abundances, reaction rates, and grain evolution in Section 2.4.5. We show that despite the uncertainty in the exact end product of COM formation, the formation of ices as carbon sinks on grain surfaces is robust, and leads to the depletion of CO in the gas phase. In order to connect the abundances of rare CO isotopologues with the overall disk mass, we examine the carbon fractionation in CO and other major carbon-bearing molecules in section 2.4.6.

### 2.4.1 Locations of ice lines

Due to efficient heating from the central star, CO and $CH_4$ do not freeze out in our modeled region—the inner 70AU of the disk—at any time in our 3 Myr of evolution (though disks with different grain properties or less luminous host stars may be colder than our model disk). Using CO isotopologues to estimate planet-forming mass therefore does not require correcting for CO freezeout, at least in disks surrounding proto-Sunlike stars. However, as we will see in Section 2.4.3, freezeout of other organic molecules affects the gaseous CO abundance. $H_2O$ and $CO_2$ freeze out at 1.5AU and 18AU at the beginning of disk evolution, and their condensation fronts move inward to 1AU and 2AU as the disk becomes cooler. We see ices of hydrocarbons and other carbon-bearing molecules formed from CO after a few hundred thousand years of disk evolution. The abundance of an ice depends on both condensation temperature and formation pathway: a molecule may have been chemically destroyed and simply not be present to freeze out. Our discussion of ice lines focuses only on locations where the relevant molecule exists. We defer the discussion of molecule formation and destruction to the next two sections.

The binding energies and the locations where different ice species exist after 3 Myr of disk evolution are shown in Table 2.3. Species with larger binding energy can form stronger bonds with the grain surface, and therefore freeze out at higher temperature. In our model, species with binding energy larger than $E_B/k = 2.5 \times 10^3$ K can freeze

out well within the giant planet-forming region at around 15AU (Tsiganis et al., 2005; Thommes et al., 2002); species with binding energy of $2.1 \times 10^3$ K can only freeze out in the outer part of the disk or at later stage of evolution when the temperature is lower, and species with binding energy lower than $10^3$ K—including CO—do not freeze out.

Table 2.3: Binding energies and ice locations for carbon-bearing molecules

| Species | Binding Energy (K) [1,2] | Ice line (100 yr) [3] | Ice line (3Myr ) [3] |
|---|---|---|---|
| $H_2O$ | 5.77 (3) | 1.5AU | 1AU |
| $CO_2$ | 2.86 (3) | 18AU | 2AU |
| CO | 8.55 (2) | > 70AU | > 70AU |
| $CH_4$ | 1.08 (3) | > 70AU | > 70AU |
| Species | Binding Energy (K) | Ice location (3Myr ) [4] | |
| $CH_3$ | 1.16 (3) | | |
| $CH_3OH$ | 4.23 (3) | r= 5 − 20AU, z=0.2 − 2AU, and r> 40AU | |
| $C_2H_2$ | 2.40 (3) | 2 − 25AU surface | |
| $C_2H_3$ | 1.76 (3) | | |
| $C_2H_4$ | 2.01 (3) | | |
| $C_2H_5$ | 2.11 (3) | > 40AU | |
| $C_2H_6$ | 2.32 (3) | | |
| $H_2CCO$ | 2.52 (3) | most of the disk 5 − 45AU | |
| $CH_3CHO$ | 2.87 (3) | r= 8 − 25AU, z= 0.5 − 2.5AU | |
| $H_2CO$ | 1.76 (3) | | |

[1] Binding energy is cited in energy (E in erg) divided by Boltzmann's constant ($k_B$ in erg/K) for easy interpretation, therefore has a unit of Kelvin.
[2] A(B) stands for $A \times 10^B$
[3] The ice line (condensation front) location on the disk midplane.
[4] For $CH_3OH$, $C_2H_2$, $C_2H_5$, $H_2CCO$, and $CH_3CHO$, we mark the location where we see certain ice species, which depend on both the condensation temperature and the ability to form the molecule. The change of abundance can be very gradual. Here we quote the boundary location where 10% of carbon is stored in corresponding species. We are only showing results for the end of evolution (3Myr ) because those molecules are not formed until about 1Myr into the disk evolution.

The condensation of volatiles is important for the growth of planets due to the increase of available solid surface density (Dodson-Robinson & Bodenheimer, 2010; Ali-Dib et al., 2014b), and is crucial for determining the chemical composition of giant planets (Öberg et al., 2011b). Moreover, the effect of radial drift and gas accretion

may cause further movement of ice lines and changes in chemical composition (Ali-Dib et al., 2014a; Piso et al., 2015). However, the above studies assumed CO to be a major carrier of carbon and oxygen, which may not be true throughout the disk evolution. Our results indicate that it is important to take into account the possibility that CO ice is not a mass source for giant planets in some systems. Instead, $CO_2$, hydrocarbons, and methanol may be the major carbon ice reservoirs that contribute to planet growth.

Furthermore, because of the unprecedented sensitivity and resolving power of (sub)mm interferometers such as the Atacama Large Millimeter/submillimeter Array (ALMA), the location of the CO ice line has been considered an important temperature tracer of giant planet-forming regions (Qi et al. 2011, 2013a). Qi et al. (2013a) use observations of $N_2H^+$, which CO destroys, to infer a CO snow line radius of $\sim$ 30 AU in the disk surrounding TW Hya. If some combinations of grain size, star luminosity and UV/X-ray/cosmic-ray flux push CO ice lines outside of 70 AU, CO freezeout may not trace the region of giant planet formation. Even TW Hya, at 0.8 $M_\odot$ and 10 Myr, is luminous enough to push its disk's CO snow line beyond the likely formation locations of Uranus and Neptune in the solar nebula.

### 2.4.2 Time evolution and spatial distribution of CO gas

Inferring disk structure based on CO line intensity is complicated by the fact that the abundance of CO evolves significantly as a function of time. In the inner 20AU from the central star when the temperature is high enough for $CO_2$ to be in the gas phase, $CO_2$ is dissociated into CO + O by cosmic ray-induced photons at a rate around $10^{-18}$ per second, which leads to an increase of CO abundance on a 1Myr time scale. On the other hand, although CO does not freeze out in our modeled region within 70AU, the abundance of CO drops beyond 15AU because carbon is tied up in hydrocarbons, methanol, and ketene (complex organic molecules or COMs), mimicking the effect of CO freezeout. Abundant carbon-bearing species include $C_2H_2$ (acetylene), $C_2H_5$, $CH_3CHO$ (acetaldehyde), $CH_3OH$ (methanol), and $H_2CCO$ (ketene). The CO depletion rate is driven by the ionization rate of $He^+$ from X-rays and cosmic rays, as $He^+$ drives the breakup of CO (section 2.4.3). The depletion of CO beyond 15AU happens on a 1Myr time scale. As a result, the CO abundance depends strongly both on location and time. As long as the disk is opaque to the UV photons that

dissociate CO, the column density of CO can increase in the inner part of the disk even as the overall disk mass is decreasing.

Color-coded plots of abundances of major carbon-bearing molecules are shown in Fig. 2.5 and Fig. 2.6. We see abundant CO within 15 AU from the central star, and abundant $CO_2$ ice in parts of the disk where the temperature is low enough for it to stay on the grain surface. $H_2CCO$ (ketene) ice is found to be the major carbon sink between 5 AU and 45AU from the central star in our model. Other COMs such as $C_2H_x$, $CH_3OH$ (methanol) and $CH_3CHO$ (acetaldehyde) exist in a layer between $2-30$ AU, closer to the disk surface, or the whole disk thickness beyond 40 AU from the central star (lower right panel of Fig. 2.5). Again, the change of abundance can be very gradual. Here we quote the boundary location where 10% of carbon is stored in corresponding species. At the end of our 3 Myr disk evolution, 13.6% of available carbon is contained in CO gas, 36.2% in $CO_2$ ice, and 44.8% in complex organic molecules. The above values are integrated over the entire disk, weighted by the disk mass in different locations. A detailed breakdown of abundances of various species can be found in the first column of Table 2.4. We present abundances in the form of percentage of carbon contained in each species, integrated over the entire disk, and weighted by disk mass in different locations.

The time evolution of the $CO/H_2$ abundance ratio (Fig. 2.7) over 3 Myr is substantial. The variation is not well-represented by a step function as in simple freeze-out models. Models of CO abundance versus radius appropriate to the star's age must be used to compute available planet-forming mass from CO isotopologue line intensities.

While this paper does not contain a parameter study of $CO/H_2$ abundance ratio as a function of disk mass and UV/X-ray/cosmic-ray flux, we suggest that flux in high-velocity line wings (produced by CO gas near the star) may increase as the star ages, even despite an overall reduction in disk mass. Furthermore, depletion of CO gas in the outer disk does not necessarily mean there is CO frozen on grain surfaces, an idea we explore further in the next section.

### 2.4.3 CO depletion due to the formation of complex organic molecules

Here we investigate the causes of CO depletion in the outer disk, beyond 15 AU. As we can see in Fig. 2.5 and Fig. 2.6, $H_2CCO$ (ketene) ice is the dominant form of

Table 2.4: Output abundances from different models

| Ice | Standard[1] | Low $H_2CCO$[2] | c2d[3] | evolving D/G |
|---|---|---|---|---|
| $CO_2$ | 36.2 | 37.6 | 31.0 | 38.4 |
| $CH_3OH$ | 8.1 | 7.4 | 24.6 | 10.1 |
| $CH_3CHO$ | 3.9 | 4.4 | 5.6 | 3.01 |
| $H_2CCO$ | 15.2 | 0.0 | 3.4 | 9.0 |
| $C_2H_x$ [4] | 16.1 | 25.9 | 3.1 | 21.0 |
| COM [5] | 44.8 | 39.4 | 37.0 | 45.0 |
| Gas | | | | |
| CO | 13.6 | 17.3 | 18.3 | 11.8 |
| $CH_4$ | 1.6 | 1.7 | 0.2 | 1.9 |

[1] Model with original reaction rates and the input from our cloud model abundances. The percentage of total available carbon contained in each species is shown in the table. All the results are values integrated over the entire disk at the end of our modeled disk evolution at 3Myr .
[2] Model with small $H_2CCO$ formation rates and the input from our cloud model abundances.
[3] Model with original reaction rates and the input adjusted to the c2d fractional abundances. See Table 2.5 for details.
[4] Hydrocarbons that contain two carbon atoms.
[5] The total abundance of complex organic molecules, including $CH_4$, $CH_3OH$, $H_2CCO$, $CH_3CHO$, and $C_2H_x$.

carbon within 45AU from the central star in the CO-depleted region. Beyond 45 AU, $CH_3OH$, $C_2H_x$, and $CH_3CHO$ ice are more abundant. To demonstrate the chemical evolution in these two different locations, we plot the abundances of major carbon-bearing molecules as a function of time in Fig. 2.7 for two locations of the disk: 38AU on the midplane and 60AU on the midplane.

At 38AU on the midplane, the depletion of CO happens in three stages. In stage 1, the first 0.6Myr , $CH_4$ and CO react to form $C_2H_2$ through two different paths (Path 1 and Path 2, see the next paragraph for details), both of which depend on the existence of $CH_4$ gas. This leads to a net destruction of CO and methane and increase in $C_2H_2$ abundance. $C_2H_2$ freezes out on grain surfaces, but because of the low binding energy of $C_2H_3$, $C_2H_2$ can not efficiently hydrogenate until the temperature decreases. The formation of more complex organic molecules such as $H_2CCO$ and $C_2H_5$ happens roughly between 0.6 to 1.5Myr (Stage 2) and only after

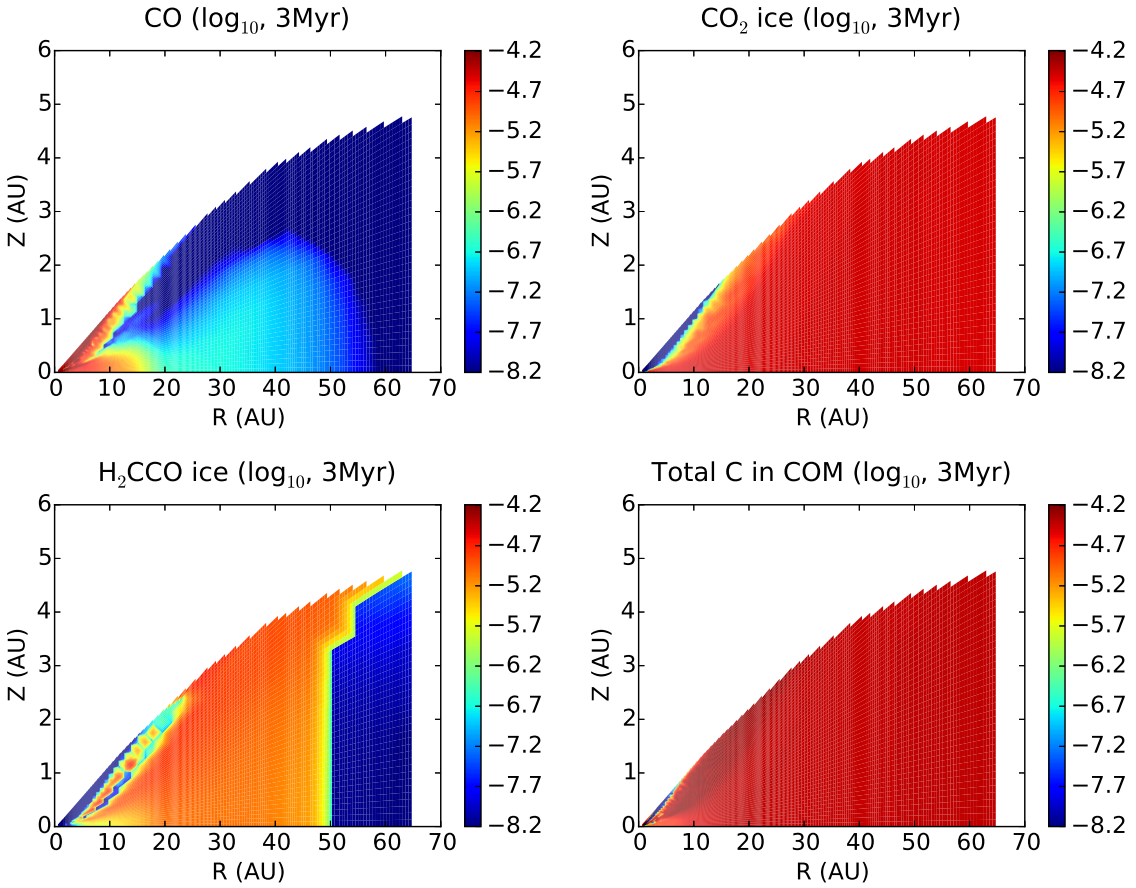


Figure 2.5: Fractional abundances at the end of the 3Myr evolution (the number density with respect to the number density of hydrogen nuclei, $n_H + 2n_{H_2}$). The color scale is in logarithm. Upper left: CO exists in a large abundance for r$<$ 15AU; Upper right: $CO_2$ ice exists in most part of the disk where the temperature is low enough for it to stay on grain surfaces; Lower left: $H_2CCO$ (ketene) ice is the major carbon sink beyond 15 AU from the central star; Lower right: Other complicated organic molecules such as $C_2H_x$, and $CH_3CHO$ (acetaldehyde) exist in a layer between $10-30$ AU, closer to the disk surface.

the reactions in Stage 1 have already begun to deplete CO. $CH_3OH$ ice forms in Stage 3 after the formation of $H_2CCO$ and $C_2H_5$ ices. The CO gas abundance continues to decrease through all three stages. At 60AU on the midplane where temperature is lower, $C_2H_3$ can stay on the grain surface and hydrogenate to $C_2H_5$ early in the disk evolution. We see rapid $C_2H_5$ formation in the first 0.6Myr , and the formation of hydrocarbons stops after $CH_4$ is depleted. Instead, the net transfer of carbon is from

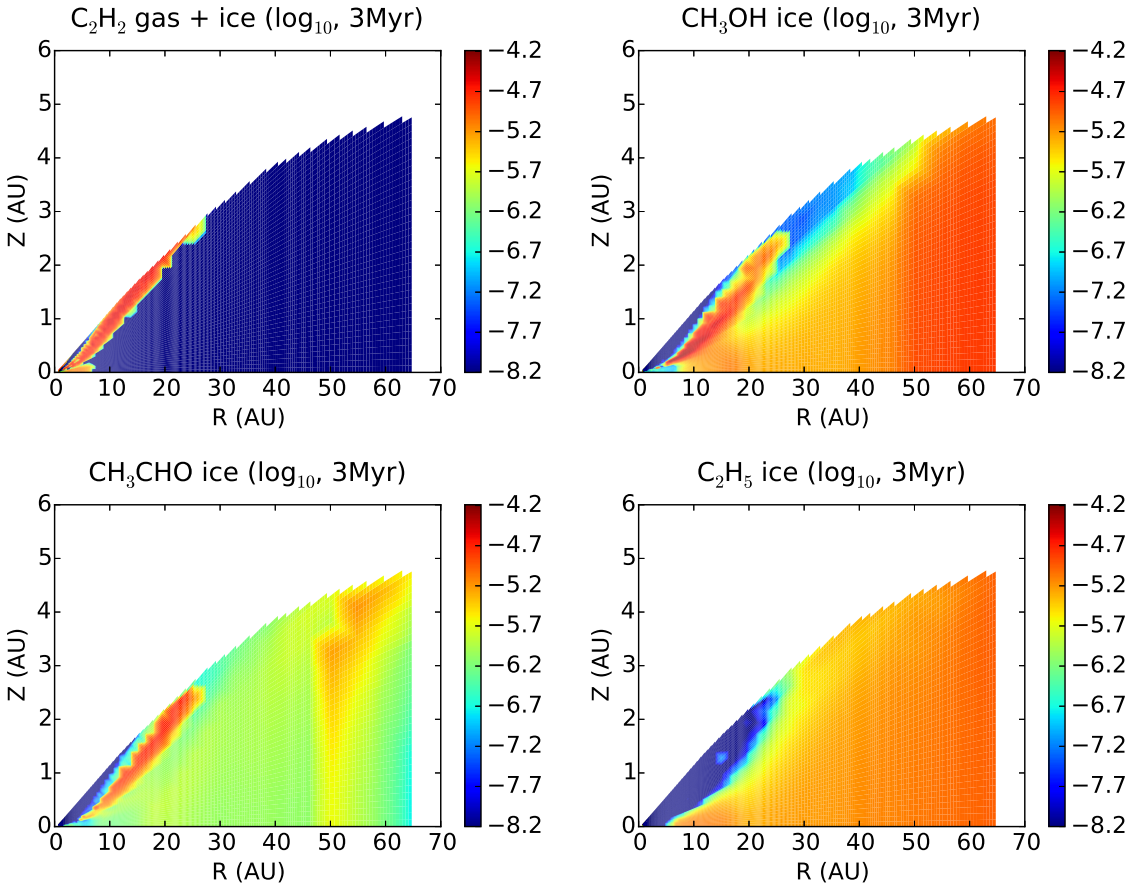


Figure 2.6: Fractional abundances continued. The figure setup is the same as in Fig. 2.5. Upper left: $C_2H_2$ is abundant where the temperature is too high for any carbon-bearing ices to freeze out; Upper right and lower left: $CH_3OH$ and $CH_3CHO$ serve as the carbon sinks where the temperature is high enough to evaporate $H_2CCO$ (ketene) ice; Lower right: $C_2H_5$ is able to form where the temperature is low enough for $C_2H_3$ to stay on grain surface and hydrogenate.

CO to $CH_3OH$.

The formation of COM primarily follows two paths: reactions between $CH_x$ radicals (Path 1), and ion-neutral reactions between $C^+$ and $CH_x$ (Path 2). The first pathway starts from $CH_4$ dissociation by secondary photons ($h\nu$) generated by cosmic ray ionization:

$$h\nu + CH_4 \rightarrow CH_2 + H_2. \tag{2.5}$$

$CH_2$ then reacts to form CH and subsequently combines with $CH_4$ to form $C_2H_4$.

$$\mathrm{H} + \mathrm{C}H_2 \rightarrow \mathrm{CH} + \mathrm{H_2} \tag{2.6}$$

$$\mathrm{CH} + \mathrm{C}H_4 \rightarrow \mathrm{C_2H_4} + \mathrm{H}. \tag{2.7}$$

Similar reactions involving other $CH_x$ radicals include:

$$\mathrm{CH_2} + \mathrm{C}H_2 \rightarrow \mathrm{C_2H_3} + \mathrm{H} \tag{2.8}$$

$$\mathrm{C} + \mathrm{C}H_3 \rightarrow \mathrm{C_2H_2} + \mathrm{H}. \tag{2.9}$$

In a relatively high temperature and hydrogen rich environment, $C_2H_3$ and $C_2H_4$ formed in above reactions quickly react into a more stable form - $C_2H_2$.

$$\mathrm{C_2H_3^+} + \mathrm{C_2H_4} \rightarrow \mathrm{C_2H_5^+} + \mathrm{C_2H_2} \tag{2.10}$$

$$\mathrm{H} + \mathrm{C_2H_3} \rightarrow \mathrm{C_2H_2} + \mathrm{H_2}. \tag{2.11}$$

While the major carbon source for the first pathway is $CH_4$, this pathway also creates molecules that react with byproducts of CO destruction. Since CO abundance is our focus in this work, we direct our attention to the second pathway. The reaction network that moves carbon from CO into COM is sketched in Fig. 2.8. The formation of COM following CO destruction is primarily driven by helium ionized by cosmic rays and X-rays. Of the resulting $He^+$ ions, more than half go on to dissociate CO (creating $C^+$ and O), while other $He^+$ ions end up ionizing molecules such as $H_2$, $C_2H_2$, $N_2$ and $CH_4$. $C^+$ rapidly reacts with $CH_4$ and $CH_3$ to form hydrocarbon ions. Hydrocarbon ions can go through a series of charge-exchange reactions until they eventually recombine with an electron to form neutral hydrocarbons. If the binding energy of the resulting neutral molecule is large enough, the neutral will quickly freeze onto the grain surface and remove carbon from the gas-phase chemistry. Key reactions that initiate hydrocarbon formation are:

$$\mathrm{H}e^+ + \mathrm{CO} \rightarrow \mathrm{O} + \mathrm{C^+} + \mathrm{H}e \tag{2.12}$$

$$\mathrm{C^+} + \mathrm{C}H_4 \rightarrow \mathrm{C_2H_3^+} + \mathrm{H} \tag{2.13}$$

$$\mathrm{C^+} + \mathrm{C}H_4 \rightarrow \mathrm{C_2H_2^+} + \mathrm{H_2} \tag{2.14}$$

$$\mathrm{C^+} + \mathrm{C}H_3 \rightarrow \mathrm{C_2H^+} + \mathrm{H_2}. \tag{2.15}$$

This full reaction chain terminates in frozen-out methanol, acetaldehyde, and ketene sinks (see Fig. 2.8).

The electrons with which the $C_2$-based hydrocarbon ions eventually recombine come mostly from cosmic-ray and X-ray ionization of $H_2$. However, unlike $He^+$, $H_2^+$ does not contribute to hydrocarbon formation directly. The majority of $H_2^+$ initiates $HCO^+$ formation through:

$$H_2^+ + H_2 \rightarrow H_3^+ + H \tag{2.16}$$

$$H_3^+ + CO \rightarrow HCO^+ + H_2. \tag{2.17}$$

Reactions involving $HCO^+$ often change the charge and/or saturation of a hydrocarbon (e.g. $C_2H_2 + HCO^+ \rightarrow CO + C_2H_3^+$), but do not contribute to the initial formation of the carbon-carbon bond.

After hydrocarbon ions recombine with electrons, the resulting neutral molecules may freeze onto grain surfaces. The dissociative recombination reactions

$$C_2H_3^+ + e^- \rightarrow C_2H + 2H \tag{2.18}$$

$$C_2H_3^+ + e^- \rightarrow C_2H_2 + H \tag{2.19}$$

$$C_2H_4^+ + e^- \rightarrow C_2H_2 + 2H \tag{2.20}$$

$$C_2H_5^+ + e^- \rightarrow C_2H_2 + H_2 + H \tag{2.21}$$

$$C_2H_5^+ + e^- \rightarrow C_2H_3 + 2H \tag{2.22}$$

contribute the most to the total neutral $C_2H_x$ abundance, and to the $C_2H_x$ ice budget (recombination pathways are marked with $e^-$ in figure 2.8). As a result, the reaction of CO with $He^+$ starts a chain that moves carbon atoms from CO to hydrocarbons on million-year timescales.

### 2.4.4 Chemical pathways in the formation of complex organic molecules

We have seen how the CO abundance beyond 20 AU decreases over time due to complex organic molecule (COM) formation. Here we trace the chemical pathways that transfer carbon from CO to COM and assess whether the outer-disk CO depletion is robust given the construction of our reaction network.

#### 2.4.4.1 Ketene as a carbon sink

Our chemical model does not include any molecule with more than two carbon atoms. Without more complex species available for reaction outcomes, $H_2CCO$ (ketene) is the most abundant two-carbon molecule found in our model and serves as a "sink" for frozen-out carbon on the grain surfaces (as seen in Fig. 2.5). The low binding energy of $C_2H_3$ also contributes to the $H_2CCO$ abundance by shutting off the hydrogenation pathway from $C_2H_3$ to $C_2H_6$ on the grain surfaces and ensuring that saturation must take place in the gas phase. (The binding energies of abundant COMs are shown in Table 2.3.) Finally, the activation barrier of $E/k_B = 1210$ K for the reaction $C_2H_2 + H \rightarrow C_2H_3$ (Hasegawa et al., 1992), which has to break the strong C–C triple bond, means that at the cold temperatures required for acetylene to freeze onto grain surfaces, hydrogenation proceeds slowly.

The most common reaction for $C_2H_3$ in the gas phase is

$$C_2H_3 + H \rightarrow C_2H_2 + H_2, \tag{2.23}$$

followed by $C_2H_2$ re-freezing onto grain surfaces. A small fraction of $C_2H_3$ gas reacts with ions such as $C_2H_3^+$, $HCO^+$, and forms more saturated hydrocarbons, then refreezes onto dust grains:

$$C_2H_3 + C_2H_3^+ \rightarrow C_2H_5^+ + C_2H, \tag{2.24}$$

$$C_2H_3 + HCO^+ \rightarrow C_2H_4^+ + CO. \tag{2.25}$$

At the same time, a small fraction of $C_2H_3$ forms a double bond with free oxygen released in Eq. 2.12:

$$C_2H_3 + O \rightarrow H_2CCO + H. \tag{2.26}$$

Since $H_2CCO$ has very high binding energy (only slightly smaller than $CO_2$), and we are not including destruction of $H_2CCO$ ice other than desorption, $H_2CCO$ ice serves as a sink for COM in our model. Although the rate for reaction 2.26 is low, ketene can nevertheless accumulate on million-year timescales. The reaction pathway leading to ketene formation is sketched in the lower left part of Fig. 2.8, with the sink molecule $H_2CCO$ enclosed in a solid box. One should note that ketene is a representative of the presence of complex organic molecules in our model. In a real disk, other forms of COM will likely exist.

Densities on grain surfaces are usually much higher than in the gas phase, so reactions such as hydrogenation on grain surfaces typically happen very quickly. However, due to the rapid thermal desorption of $C_2H_3$ from the grain surface, more saturated hydrocarbons cannot be formed efficiently. In most of the disk within 40AU, only a small amount of more saturated $C_2$ hydrocarbons can be formed in the gas phase through ion-neutral reactions, with a negligible amount formed though hydrogenation on the grain surface.

#### 2.4.4.2 Acetaldehyde as a carbon sink

Ketene is no longer the sink in regions where the temperature is high enough for it to be in the gas phase, or where the temperature is low enough for $C_2H_3$ to stay on the grain surface and continue hydrogenating to form more saturated hydrocarbons. In those regions, ice molecules such as $CH_3CHO$ (acetaldehyde), $CH_3OH$ (methanol), and $C_2H_5$ (ethyl) serve as the carbon sinks, keeping carbon from re-entering the gas phase.

Green lines in Fig. 2.8 show the ketene recycling pathway in a small region below the disk surface between $10 - 30$AU, where the temperature is high enough that $H_2CCO$ stays in the gas phase and the ionization rate is $\geq 10^{-15}$ s$^{-1}$. $H_2CCO$ gas reacts with $C^+$ to form $CH_2CO^+$:

$$C^+ + H_2CCO \rightarrow CH_2CO^+ + C. \tag{2.27}$$

$CH_2CO^+$ then recombines with an electron and undergoes one of three dissociative recombination reactions to form $C_2$, $C_2H_2$, or CO, with roughly equal branching ratios (see green lines leading from $CH_2CO$ molecule in lower left corner of Fig. 2.8). Moreover, due to the high ionization rate, the rate of reaction 2.12 can be as much as twice the value on the disk midplane. The abundance of free hydrogen atoms is also high due to photodissociation of $H_2$ and $H_2O$. Efficient $C^+$ production and high atomic hydrogen abundance speed the production of $C_2H_2$ and allow more saturated hydrocarbons to form on grain surfaces, despite the volatility of $C_2H_3$. The temperature in the region is high enough for $C_2H_5$ to evaporate into the gas phase once it is formed. $C_2H_5$ then reacts with atomic oxygen to from the more stable molecule $CH_3CHO$ (acetaldehyde), which refreezes on to the grain surface due to its

high binding energy and serves as another carbon sink:

$$\mathrm{O} + \mathrm{C_2H_5} \rightarrow \mathrm{C}H_3\mathrm{C}HO + \mathrm{H}. \tag{2.28}$$

To summarize, the acetaldehyde-forming reaction pathway (Fig. 2.8) differs from the ketene-forming pathway simply because of the warmer temperature that keeps ketene in the gas phase, the high $C^+$ abundance from reaction 2.12, and the high atomic hydrogen abundance. Note that our reaction network does not include the grain-surface hydrogenation pathway $C_2H_5 + H \rightarrow C_2H_6$ (ethane ice). However, Dodson-Robinson et al. (2009) found low grain-surface hydrogenation efficiency, leading to significant amounts of ethane ice only near the acetylene sublimation temperature of 55 K.

#### 2.4.4.3 Ethyl and methanol as carbon sinks

In the outer disk where $r > 50$ AU, and after 1Myr in most of the disk, $C_2H_3$ is able to stay on the grain surface and hydrogenate to $C_2H_5$, and $C_2H_5$ serves as a carbon sink.

Due to the lack of $C_2H_3$ in the gas phase, and the low temperature that allows $H_2CO$ to freeze out, the reaction

$$\mathrm{O} + \mathrm{C}H_3 \rightarrow \mathrm{H_2C}O + \mathrm{H} \tag{2.29}$$

becomes the dominant reaction with atomic oxygen, rather than reaction 2.26. $H_2CO$ then freezes onto the grain surface, reacts with H atoms on the grain surface, and finally forms $CH_3OH$ (methanol), another carbon sink in our model, as follows (letter G denotes species that are frozen out on grain surfaces):

$$\mathrm{GH} + \mathrm{GH_2C}O \rightarrow \mathrm{G}CH_2\mathrm{O}H \tag{2.30}$$

$$\mathrm{GH} + \mathrm{G}CH_2\mathrm{O}H \rightarrow \mathrm{G}CH_3\mathrm{O}H. \tag{2.31}$$

This reaction path explains the evolution of abundances of carbon-bearing molecules demonstrated in the lower panel of Figure 2.7. These reactions start to happen at $r > 60$AU where the temperature is about 35K, and at 20AU on the midplane at 2.5Myr when the temperature drops below 44K.

In summary, as Fig. 2.5 and Fig. 2.6 show, $H_2CCO$ dominates in most of the COM-forming region where the temperature is low enough for $H_2CCO$ to remain on

the grain surface, but high enough for $C_2H_3$ to evaporate into the gas phase. In the small region above the disk midplane (r = 10 − 35AU, z = 1 − 4AU), where the temperature is high enough for $H_2CCO$ and $C_2H_5$ to stay in the gas phase and atomic hydrogen is abundant, $CH_3CHO$ serves as the sink for carbon chemistry. In the outer region where the temperature is low enough for $C_2H_3$ to stay on the grain surface and hydrogenate to $C_2H_5$, we are seeing $CH_3OH$ and $C_2H_5$ as the end products of COM chemistry.

The reaction pathways described above demonstrate how $H_2CCO$, $CH_3CHO$, $C_2H_2$ and $CH_3OH$ stand in for complex organic molecules in our model. In reality, organic molecules may grow more complex as ketene, acetaldehyde, ethyl, and methanol ice react with other species in ways not included in our model. Despite our upper limit of two carbon atoms per molecule, the net movement of carbon from CO to ices should be a robust result for ionized regions that contain $CH_4$ gas. In order to demonstrate that our reaction network does not falsely predict carbon depletion from the gas phase, we investigate an alternative network with a low ketene formation rate in the next section. We also compare our model abundances with results from the c2d (cores to disks) *Spitzer* Legacy Program as summarized by Öberg et al. (2011a), and discuss the effect of different assumptions about grain evolution.

### 2.4.5 Model dependence on reaction rates, initial conditions, and grain evolution models

Our model results depend on the disk physical conditions, initial cloud phase abundances, and reaction rates. In this section, we present a detailed study of how results depend on reaction rates, initial abundances, and grain evolution. In section 2.4.5.1, we verify that our ketene ice sink does not artificially remove carbon from the gas phase by running a model with the ketene formation rate decreased by 10 orders of magnitude. In Section 2.4.5.2, we compare the abundances from our molecular cloud preprocessing model with the ice abundances observed by the *Spitzer* c2d team in the envelopes of low-mass protostars (Öberg et al., 2011a). In Section 2.4.5.3, we investigate the effects of grain evolution on the disk temperature and chemistry.

Our current model cannot consider gaps or inner holes without significant modifications. The effects of such structures on chemical evolution requires further study.

#### 2.4.5.1 Models with low $H_2CCO$ formation rates

The formation of carbon sinks such as ketene greatly reduces the gas-phase CO abundance in our model and suggests that observations of CO depletion may trace complex-molecule formation instead of freezeout of CO. In this section, we test the robustness of our result by artificially suppressing ketene formation rates. The CO abundance is independent of the exact form of carbon-bearing ice as long as our model does not artificially remove carbon from the gas phase. However, having $H_2CCO$ ice instead of $C_2H_x$ ice as a sink in the model can potentially reduce the amount of oxygen in the gas phase, therefore affecting the CO abundance. To test the effect of $H_2CCO$ formation rate on CO abundance, we ran the chemical model with $H_2CCO$ formation rates artificially turned down by ten orders of magnitude while keeping other parameters the same.

We compare output abundances at the end of the 3 Myr evolution of this experiment with those from our fiducial COM-forming model (described in Section 2.4.3) in Table 2.4.

The $H_2CCO$ formation is strongly suppressed as expected, resulting in a negligible abundance. Without the pathways that convert hydrocarbons ($C_2H_x$) to ketene, the abundance of hydrocarbons ($C_2H_x$) is significantly higher, but most other abundances show little change. The gas-phase CO abundance increases from 13.6% to 17.3% of the elemental carbon.

To summarize, the choice of end-member species in the chemical reaction network can affect the gaseous CO abundance. Translating observed CO isotopologue line intensities into disk surface densities would include an uncertainty of at least a factor of two for any given disk annulus. However, the effect of the ketene sink on the CO gas abundance in our modeled 70 AU disk as a whole is small. One would be able to translate a measurement of the mass of $C^{17}O$ or $C^{18}O$ gas in the planet-forming region of a disk into a total mass available for giant planet formation without large uncertainties due to the chemistry of complex organic molecule formation.

#### 2.4.5.2 Comparing with the c2d cloud abundances

We test the sensitivity to initial conditions in our chemical reaction network by comparing the abundances at the end of our molecular cloud preprocessing model with measured ice abundances in low-mass protostellar envelopes. Öberg et al. (2011a)

combined *Spitzer*/ IRS spectra for about 50 low-mass protostars with infrared ice features with near-infrared ground-based observations of ice features such as 3$\mu$m $H_2O$, 4.65$\mu$m CO, and 3.53$\mu$m $CH_3OH$, presenting an overview of the ice inventory during the embedded phase of star formation. Because the absolute ice abundances vary from source to source, Öberg et al. (2011a) presented the median ice abundance ratio with respect to water ice abundance in the combined sample. The chemical compositions observed in low-mass protostellar envelopes are expected to be similar to those at the end of the molecular cloud phase, because the materials are not yet heavily heated by the central star or processed by shocks.

We compare c2d observed ice abundance ratios and outputs of our cloud phase model (as described in Section 3.1) in the first two columns of Table 2.5. The $CO_2$, $CH_4$, and CO abundances with respect to the water ice abundance in our cloud model are about 1.2, 5, and 0.5 times the values observed in nearby star-forming regions, respectively (Öberg et al., 2011a). While not an exact match, our computed abundances relative to water ice are of the same order of magnitude as observed values for major carbon-bearing species.

Table 2.5: Abundances at the end of the cloud phase

| Ice species | MC fraction [1] | c2d fraction [2] | MC abundance [3] | c2d abundance [4] |
|---|---|---|---|---|
| $H_2O$ | 100 | 100 | 9.1(−5) | 9.1(−5) |
| $CO_2$ | 35 | 28 | 3.2(−5) | 2.7(−5) |
| $CH_4$ | 24 | 5 | 2.2(−5) | 4.6(−6) |
| CO | 15 | 29 | 1.3(−5) | 2.7(−5) |
| Gas species | | | | |
| CO | | NA [5] | 1.9(−6) | 1.9(−6) |

[1] Fractional abundances in our molecular cloud model, normalized to the $H_2O$ ice abundance.
[2] Fractional abundances in the c2d result, normalized to the $H_2O$ ice abundance.
[3] Output abundances in our molecular cloud model.
[4] Abundances scaled according to the c2d result, using the $H_2O$ abundance as the reference.
[5] Öberg et al. (2011a) does not include gaseous species.

To test how our disk model varies based on small changes in input abundances, we conduct an experiment using the Öberg et al. (2011a) observed abundances as

the initial conditions for the chemical evolution, while keeping other parameters the same. We keep the same abundances as predicted by our molecular cloud model for $H_2O$ ice and minor species not observed by the c2d team, but scale the abundances of other c2d-observed ices to match the c2d results. The abundances predicted by the molecular cloud model, and the abundances adjusted according to c2d ratios, are listed in the last two columns of Table 2.5. This experiment is only to demonstrate the model dependence on initial input abundances. We do not conserve the total number of C and O atoms per hydrogen atom by artificially scaling the molecular abundances.

The change of input abundances does not change CO abundance significantly in our experiment. Integrated over the entire disk, the total available carbon in the form of CO gas increases from 13.6% to 18.3%, while the carbon locked in COM decreases from 44.8% to 37.0% However, the dominant kind of COM is different from that of the standard model. Due to the significantly lower input methane abundance, the percentage of molecules that contain two carbon atoms is only one third of the value in the fiducial model, and the methanol abundance is three times the original value. The paucity of ices that contain two carbon atoms when the initial methane abundance is low suggests that even though the formation of the carbon-carbon bond relies on both $CH_4$ and $C^+$ liberated from CO, the formation of carbon chain depends largely on the methane abundance the disk inherits from the cloud.

We find that the abundances predicted by our molecular cloud model agree with observational results within a factor of two. In our experiment, adjusting the abundances inherited by the disk to match observed abundances in cold protostar envelopes can lead to a higher abundance of methanol and a smaller overall COM abundance than in our fiducial model. However, the computed CO abundance is only 1.35 times higher.

#### 2.4.5.3 Different models of grain evolution

In the fiducial model, we assume 90% by mass of the of dust has already grown to larger than mm size, and use a gas to dust ratio of 1000 throughout. However, grain evolution could be slower than what we assume. Specifically, the disk could have a larger portion of dust than what we assumed at the beginning of the evolution. Small dust grains provide most of the opacity that is important for heating and

attenuating UV and x-ray radiation, and they also provide most of the surface area available for freeze-out and grain surface reactions. Miotello et al. (2014) have found that the evolution of dust grains can change the disk opacity, which can further increase the significance of isotopologue-selective photodissociation, and change the CO fractionation.

To investigate the effect of grain evolution, we construct a series of models with gas to dust ratio gradually evolving from 100 to 1000, assuming the same opacity profile for the dust grains. We choose to change the gas to dust ratio to trace the loss of solid material to bigger bodies, rather than changing the grain size distribution, because a balance between collisional aggregation and fragmentation yields a size distribution whose slope at the small end is insensitive to the dust abundance (Birnstiel et al., 2011).

In the models considering grain evolution, the total dust opacities are larger than those in the fiducial model, resulting in lower disk temperature. On average, the disk temperature is 10% lower at 100 yr where the gas-to-dust ratio is 10 times the fiducial value, and 5% lower at 1Myr when the gas-to-dust ratio is one third of the fiducial value.

The output abundances averaged over the entire disk are presented in the last column of Table 2.5. Despite the decrease of temperature, the carbon content in the grain evolution model is very similar to that in our fiducial model by the end of the 3Myr evolution. This is because CO depletion happens on a Myr time scale when grain evolution has already started, and the grain surface area is not limiting the freeze-out time scale as long as some dust grains are present. The final CO abundance relative to total carbon decreases from 13.6% in the standard model to 11.8% in this model, a change in the opposite direction to that found in the other model variations. The difference between the two models is largest at 1 Myr, when the CO/C ratio is 27.5% in the standard model and 21.8% in the grain evolution model. Unlike in Miotello et al. (2014), considering grain evolution does not significantly change abundance ratios of CO isotopologues in our models. We defer detailed discussions on isotopic ratios to section 2.4.6.

### 2.4.6 Fractionation of CO isotopologues

In addition to understanding the formation and destruction pathways of CO, one also needs to know how C and O isotopes fractionate among different molecules in order to link $^{13}$CO, C$^{17}$O, and C$^{18}$O observations with disk masses. The isotopologue ratio in CO and the major carbon sink $H_2CCO$ are presented in Figure 2.9. The CO/$^{13}$CO ratio is close to the elemental isotopic value of 77.15 in the inner 15AU where CO gas is abundant. In regions where CO is depleted, the CO/$^{13}$CO ratio is about 45, much smaller than the input atomic abundance ratio. The low CO/$^{13}$CO ratio is inherited from the molecular cloud model.

In the inner disk, where new CO molecules are forming from recycled ketene that originally gained its carbon atoms from both $CH_4$ and CO, the CO/$^{13}$CO ratio approaches the input, atomic C/$^{13}$C ratio. Integrated over the entire disk, the average CO/$^{13}$CO ratio is 59.15. Disk mass estimates based on optically thin $^{13}$CO rotational emission (possible beyond $\sim$ 18 AU; see Section 2.5) should account for isotopic fractionation.

In the shielded interior of our disk, we predict C$^{16}$O/C$^{17}$O and C$^{16}$O/C$^{18}$O ratios similar to those measured by Smith et al. (2009) from observations of the envelope of protostar Reipurth 50. Our computed CO/C$^{17}$O and CO/C$^{18}$O ratios are slightly smaller than the input $^{16}$O/$^{17}$O = 2300 and $^{16}$O/$^{18}$O = 500 ratios throughout most of the disk, though the recycling of ketene back to CO pushes C$^{16}$O/C$^{17}$O and C$^{16}$O/C$^{18}$O higher near the disk surface. The CO oxygen isotope fractionation identified in our model has an average effect of less than 14% (averaged over mass). We find that oxygen isotope fractionation would not significantly bias disk mass estimates based on C$^{17}$O or C$^{18}$O emission.

We also caution against over-interpretation of the oxygen isotope fractionation found in this model, as variations in UV flux that are well within observed ranges (France et al., 2014) can affect isotope ratios. In Miotello et al. (2014), UV radiation is not attenuated efficiently in disks with only larger grains. Rare CO isotopologues only exist in a smaller region further below the disk surface due to photo-dissociation, resulting in larger CO to rare CO ratios. In contrast, our models include a population of small dust grains even for models with grain evolution (Section 2.4.5.3), and therefore the UV radiation is sufficiently absorbed. Moreover, following Landry et al. (2013), our disk models only follow the disk up to about two scale heights, and do not

follow the disk atmosphere, where photochemical reactions matter the most. This explains why unlike in Miotello et al. (2014), considering grain evolution does not significantly change the CO isotopologue ratios.

Having verified that our predicted $^{13}$CO, C$^{18}$O, and C$^{17}$O abundances are robust results that (1) do not depend heavily on our reaction network choice and (2) closely track observed values, we are now ready to calculate the optical depths of rotational emission lines.

## 2.5 Optical depth of rotational emission from CO isotopologues

Our goal is to demonstrate that rare CO isotopologues can provide a window into the planet formation zone through their rotational emission lines. The ideal emission line would be optically thin all the way to the disk midplane, but still detectable with ALMA. We calculate the optical depth of CO rotational emission lines at each disk radius by integrating the absorption efficiency through the disk. We first calculate the total absorption efficiency across the emission line as

$$\int k_\nu d\nu = \frac{h\nu_{ij}}{c}\left(n_i B_{ij} - n_j B_{ji}\right), \tag{2.32}$$

in which

$$B_{ji} = \frac{g_i}{g_j} B_{ij}, \tag{2.33}$$

$$B_{ij} = \frac{8\pi^3}{3h^2}|\mu_{ij}|^2, \tag{2.34}$$

$$n_i = f_i n_x. \tag{2.35}$$

$k_\nu$ is the absorption coefficient, $n_i$, and $n_j$ are the number of molecules in states i and j (i is the lower state), and $f_i$ and $f_j$ are the fraction of molecules in states i and j. $g_i$ and $g_j$ are the degeneracies; $\nu_{ij}$ is the frequency of the transition; $\mu_{ij}$ is the matrix element of the electric dipole moment for the transition; and $B_{ij}$ and $B_{ji}$ are the Einstein coefficients of the transition. Substituting into equation 2.32, we have:

$$\int k_\nu d\nu = \frac{h\nu_{ij}}{c} f_i n_x \frac{8\pi^3}{3h^2}|\mu_{ij}|^2 \left[1 - exp\left(\frac{-h\nu_{ij}}{kT}\right)\right]. \tag{2.36}$$

We take $f_i$ as the local thermodynamic equilibrium (LTE) value set by the Boltzmann distribution.

To estimate the absorption at the line center $k_0$, we divide the total absorption efficiency by the full-width half-maximum $\Delta\nu$ of the Doppler broadening profile:

$$\Delta\nu = 2.355 \times \sqrt{\frac{\nu_0^2 kT}{Mc^2}}, \tag{2.37}$$

where $M$ is the mass of the molecule. We then have

$$k_0 = \frac{\int k_\nu d\nu}{\Delta\nu}. \tag{2.38}$$

Finally, we compute face-on optical depths as a function of distance from the star by integrating the absorption efficiency $k_0$ over the disk's vertical direction as

$$\tau_0 = \int_0^{z_{surface}} k_0 dz. \tag{2.39}$$

The optical depths of J= $1 \rightarrow 0$ lines for CO isotopologues are shown in the upper panels of Figure 2.10. The upper-left panel shows optical depths after 100 years of disk evolution (i.e., a disk surrounding a just-emerged T-Tauri star), and the upper-right panel shows the disk after 3 Myr of evolution. We highlight the J= $1 \rightarrow 0$ transition because the temperature of CO gas is relatively high compared to the energy needed to excite the J = 1 rotational level ($5.5K$), therefore J = $1 \rightarrow 0$ line is the most optically thin line among low order rotational lines observable with ALMA. We can immediately see that $C^{17}O$ traces the disk midplane outside 8 AU, and $C^{18}O$ traces the midplane outside 12 AU. Observations of $C^{17}O$ and $C^{18}O$ emission from nearby disks would provide estimates of the amount of mass available to form planets like Uranus and Neptune, and place a lower limit on the mass available to form Jupiter and Saturn.

The optical depth of $C^{17}O$ as a function of radius is plotted for several epochs in the lower left panel of Figure 2.10. The optical depth is a strong function of radius and time. The optical depth in the inner part of the disk increases as the disk evolves due to the dissociation of $CO_2$ into CO, while the optical depth beyond 15AU first increases, but then decreases and falls below the initial value due to the formation of more complex carbon-bearing molecules (sections 2.4.2, 2.4.3). At 3Myr the optical depth remains above one out to about 42AU for CO, 18AU for $^{13}CO$, 12AU for $C^{18}O$, and 8AU for $C^{17}O$. The possibility that CO abundance changes over time due to

chemical reactions means that disk masses measured by CO emission are degenerate with age.

Continuum emission from dust also contributes flux at the frequencies of CO emission lines. Even if the emission from a CO isotopologue is optically thin, high optical depth in the dust could prevent us from seeing the disk midplane. To estimate the optical depth contributed by the dust, we integrate the dust opacity at the relevant wavelength over the disk height. We use opacities from Semenov et al. (2003), for grains with a 5-layered sphere topology. As in the thermodynamic model (see Section 2.2 for details), we use a gas to dust mass ratio of 1000. We assume the dust has undergone some degree of grain growth, with remaining solids locked into larger bodies, consistent with our RADMC dust radiative transfer models. Optical depth contributed by dust is plotted in the lower right panel of Figure 2.10. The optical depths contributed by dust are almost the same for all isotopologues due to the small shift in frequency between emission lines, so we are only showing the frequency at the center of CO transitions. The optical depths contributed by dust are smallest for the J$= 1 \rightarrow 0$ line due to lower frequency - less than one beyond 2AU, and less than 0.1 beyond 10AU. The dust optical depth for higher order transitions become less then one within 10AU.

For low-mass disks that have experienced some grain growth, $C^{17}O$ is a promising tracer of the disk midplane in the giant planet-forming region. Outside of 10 AU, where analogs to the Kuiper Belt may be forming (Bryden et al., 2009), $C^{18}O$ and $^{13}CO$ may be useful midplane tracers. Note, however, that our fiducial model is a low-mass disk ($0.015\,M_{\odot}$), and the actual midplane locations traced by CO gas may therefore fall somewhat outside of 10 AU. However, our results demonstrate the value of observing CO isotopologues to reconstruct the mass distributions in the inner 30 AU of nearby disks.

## 2.6 Conclusions

Our chemical model of an MRI-active protoplanetary disk has led to the following conclusions.

CO does not freeze out anywhere in our modeled region - the inner 70AU of the disk - due to efficient heating by stellar irradiation. Instead, the abundance of CO

is a complex function of both radius and time. This dependence must be modeled correctly in order to deduce gas properties from observations of CO isotopologues.

The fate of CO is tied up in the formation of complex organic molecules. While the detailed chemical evolution depends on the input abundances from the molecular cloud and which species are included in the network, the main result is robust to these variations. Different models of grain evolution also produce small changes in the outcomes. For three different chemical assumptions and two different scenarios for grain evolution, the partition of carbon, integrated over the modeled inner 70 AU of the disk, ranges from 11.8% to 18.3% in CO gas, 31.0% to 38.4% in $CO_2$ ice, and 37.0% to 45.0% in complex organic molecules.

Fractionation of oxygen isotopes appears not to play a major role in $C^{17}O$ abundances, though stars with unusually strong UV accretion luminosity may have disks depleted in $C^{17}O$. The optical depth of low-J rotational lines of $C^{17}O$ are around unity in the giant planet forming region, while more common isotopologues are quite opaque. With our computed $C^{17}O/H_2$ abundance as a function of radius and an age, one would be able to translate the observed $C^{17}O$ line intensity into available planet-forming mass, to within a factor of a few. The optical depth of dust in the CO isotopologue (J= $1 \rightarrow 0$) transition wavelengths is small enough to allow observations of the mid-plane beyond a few AU; for higher transitions the dust will be opaque within 5-8 AU. However, this result relies on our assumption of grain evolution, in which 90% of the solid mass has accumulated in pebbles and larger solid objects at the start of disk evolution at 0.1 Myr , but our experiment with slower evolution of the gas to dust ratio produce similar results in the end.

Looking ahead to future work, we emphasize that emission lines from the CO isotopologues all have different optical depths and can probe different vertical layers of a target disk. Comparing line profiles of emission from multiple isotopologues could reveal vertical variations in turbulent velocity, and therefore constrain the angular momentum transfer mechanism that drives the disk evolution. The current leading angular momentum transfer mechanism—MRI turbulence—predicts non-turbulent "dead" zones on the disk midplane, which leads to a decrease of the turbulent velocity toward the midplane (Fromang & Nelson (2006), Simon et al. (2011)). However, new models by Bai & Stone (2013) and Gressel et al. (2015) suggest that magnetocentrifugal winds are more likely to drive accretion than the MRI. Aside from possibly driving accretion, turbulence also determines the behavior of dust grains to a great extent.

An observational investigation of gas velocities in the midplanes of planet-forming disks would have profound implications for planetesimal growth models. ALMA is able to detect emission from multiple CO isotopologues in one observation. With its new long baselines and large collecting area, it is sensitive to the inner regions of disks, which have small emitting areas but contribute appreciably to line wings. CO observations may be able to probe not only the mass distribution in planet-forming regions, but the gas dynamics as well.

We conclude that CO isotopologue rotational emission can probe the mass distribution and chemical evolution of the inner radii of protostellar disks, allowing observers to peer directly into planet nurseries.

Acknowledgments: Work by MY, KW, SDR and NJT was supported by NASA grant NNX10AH28G. NJE and MY were supported in part by NSF Grant AST-1109116 to the University of Texas at Austin. This work was performed in part at the Jet Propulsion Laboratory, California Institute of Technology. NJT was supported by grant 13-OSS13-0114 from the NASA Origins of Solar Systems program. We are grateful to the referee for helpful suggestions. We would like to thank Edwin Bergin, Jacob Simon, Ilse Cleeves, Jeong-Eun Lee, Seok-Ho Lee, Jeffrey Cuzzi, Paul Estrada, Colette Salyk, Karin Öberg, and Raquel Salmeron for useful discussions.

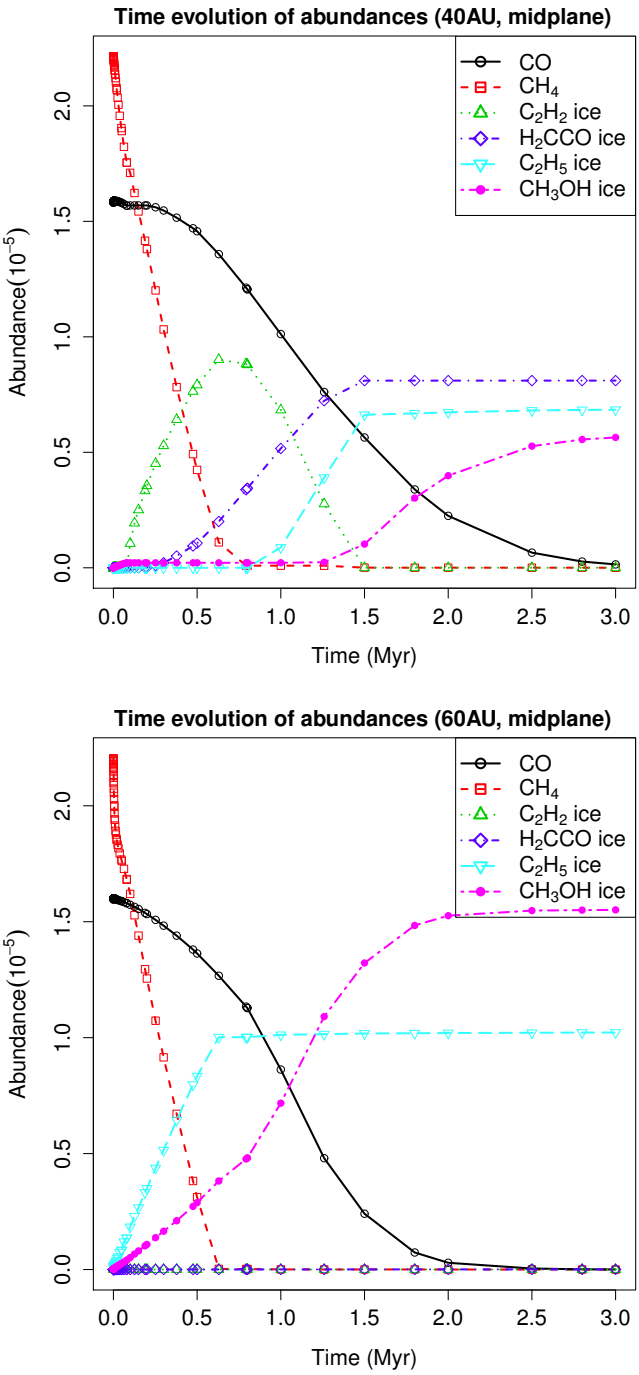


Figure 2.7: Abundances of major carbon-bearing molecules as functions of time. Upper panel: 38AU on the disk midplane; lower panel: 60AU on the disk midplane. Points show the values of actual data points in our models.

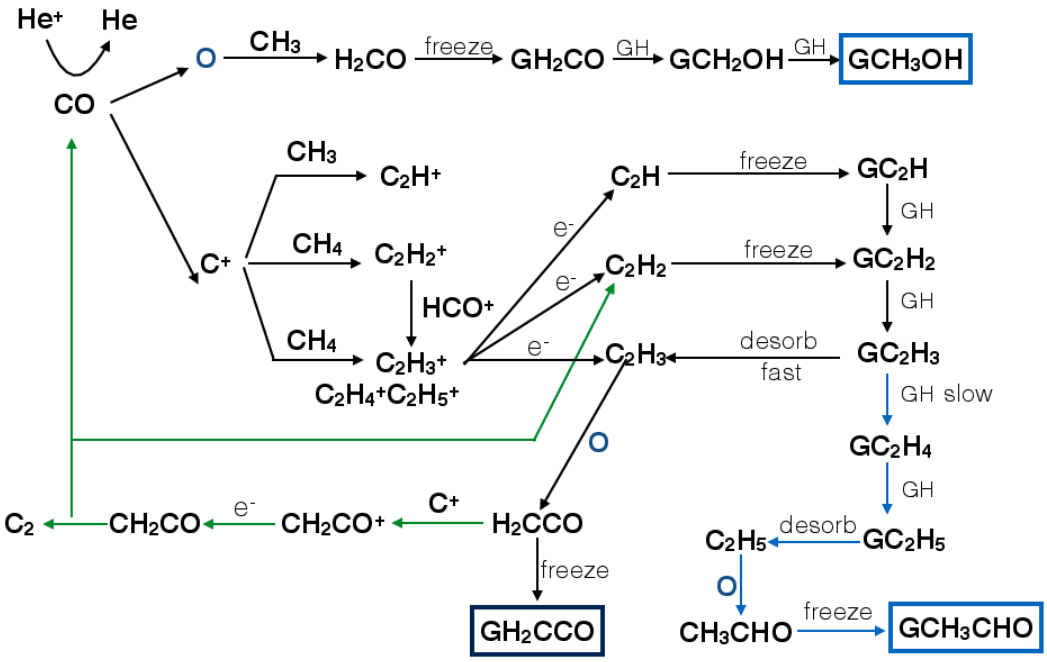


Figure 2.8: Reaction network for major carbon-bearing species. The species with boxes drawn around them are sinks, and letter G denotes species that are frozen out on grain surfaces. Starting from the upper left side the the figure: (1) The dissociation of CO is initiated by $He^+$; (2) The topmost pathway shows methanol formation in relatively hot regions of the disk, where $H_2CCO$ molecules are not able to stay on the the grain surface. (3) The blue lines represent processes that move carbon from $C_2H_3$ to $GCH_3CHO$ (acetaldehyde); (4) The green lines trace a path for removing carbon from ketene in warm parts of the disk; To summarize, $C_2H_2$ gas exists where the temperature is too high for icy carbon sinks to form. GCH3CHO and GCH3OH are the carbon sink in warm regions, GH2CCO in the majority part of the disk where the temperature is lower.

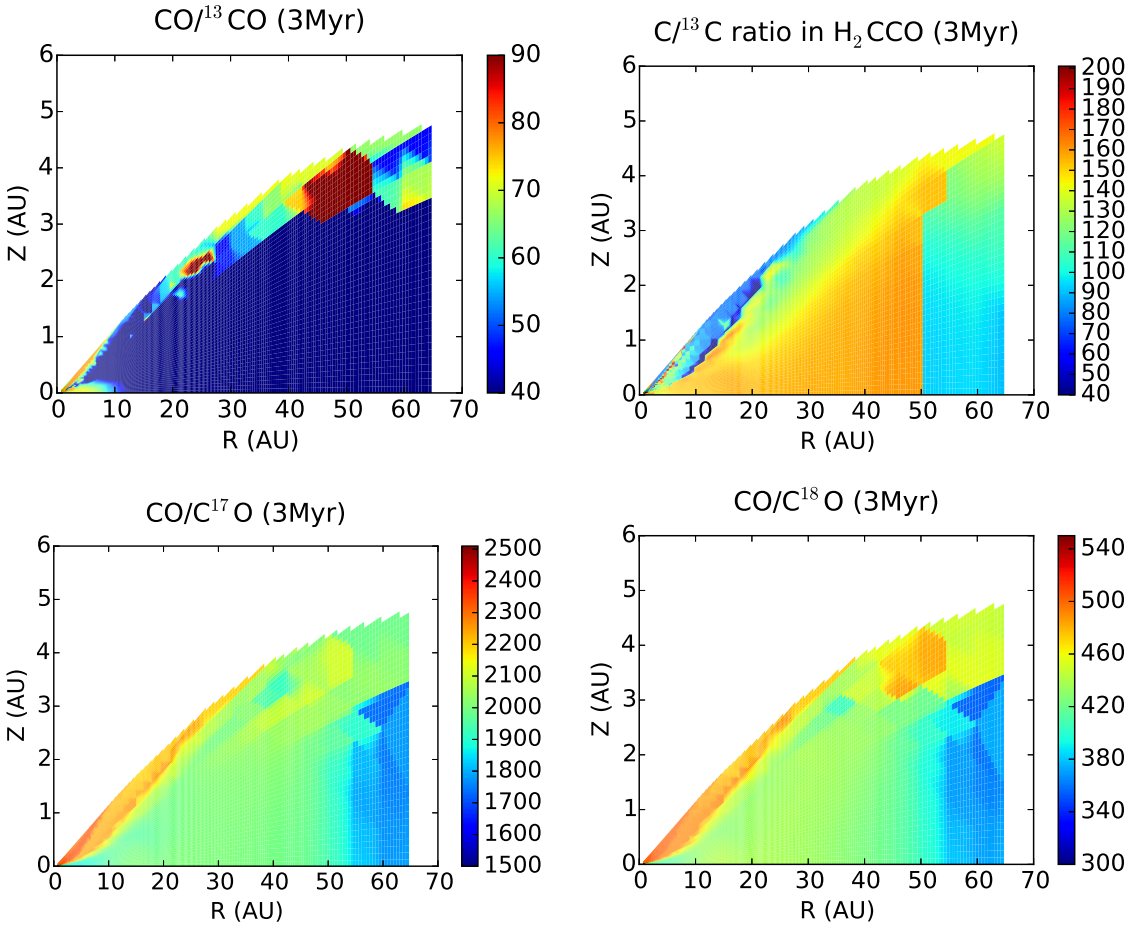


Figure 2.9: Upper left: CO/$^{13}$CO ratio (all four plots are for the end of the 3Myr evolution); Upper right: C/$^{13}$C ratio in $H_2CCO$ ice; Lower left: CO/C$^{17}$O ratio; Lower right: CO/C$^{18}$O ratio. Unsuperscripted species denote the most common isotopologue.

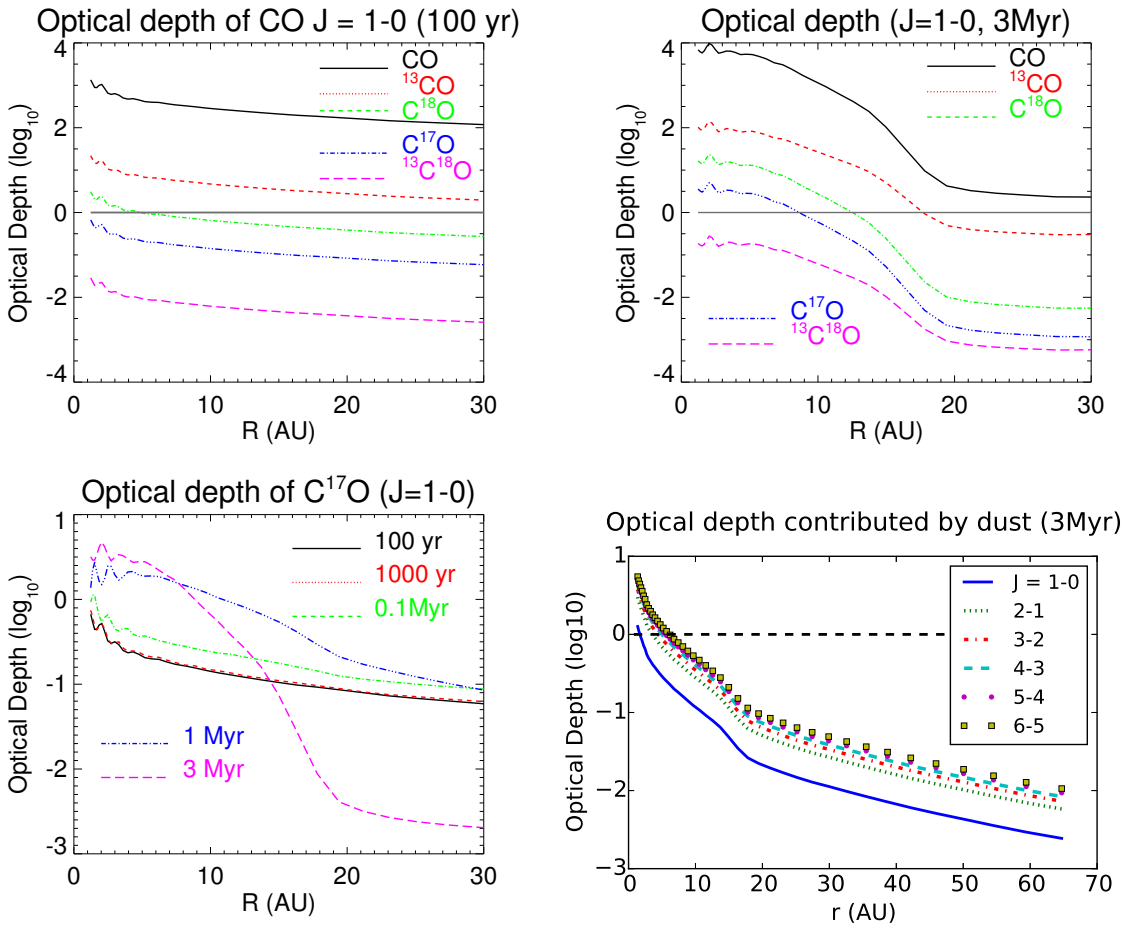


Figure 2.10: Upper left panel: Optical depth of various CO isotopologues J = 1 → 0 (100 yr). Upper right panel: Optical depth of various CO isotopologues J = 1 → 0 (3 Myr). Lower left panel: Optical depth of $C^{17}O$ J = 1 → 0 (time evolution). The optical depth increases over time roughly in r < 20 AU due to the photodissociation of $CO_2$ lead by cosmic ray-induced photons, and the optical depth at r > 20 AU decreases over time due to the formation of COMs. Lower right panel: Optical depth contributed by dust emission at the wavelength of various CO transitions. Dust emission should not contribute much to observed fluxes in low-order CO rotational emission lines beyond 10AU.

# Chapter Three: Disk masses around solar-mass stars are underestimated by CO observations [1]

Gas in protostellar disks provides the raw material for giant planet formation and controls the dynamics of the planetesimal-building dust grains. Accurate gas mass measurements help map the observed properties of planet-forming disks onto the formation environments of known exoplanets. Rare isotopologues of carbon monoxide (CO) have been used as gas mass tracers for disks in the Lupus star-forming region, with an assumed interstellar $CO/H_2$ abundance ratio. Unfortunately, observations of T-Tauri disks show that CO abundance is not interstellar—a finding reproduced by models that show CO abundance decreasing both with distance from the star and as a function of time. Here we present radiative transfer simulations that assess the accuracy of CO-based disk mass measurements. We find that the combination of CO chemical depletion in the outer disk and optically thick emission from the inner disk leads observers to underestimate gas mass by more than an order of magnitude if they use the standard assumptions of interstellar $CO/H_2$ ratio and optically thin emission. Furthermore, CO abundance changes on million-year timescales, introducing an age/mass degeneracy into observations. To reach factor of a few accuracy for CO-based disk mass measurements, we suggest that observers and modelers adopt the following strategies: (1) select the low-$J$ transitions; (2) observe multiple CO isotopologues and use either intensity ratios or normalized line profiles to diagnose CO chemical depletion; and (3) use spatially resolved observations to measure the CO abundance distribution.

[1]This chapter was published in Astrophysical Journal in 2017 as Yu, M., Evans, II, N. J., Dodson-Robinson, S. E., Willacy, K., Turner, N. J. 2017, ApJ, 841, 39. Mo Yu was the leading author of that paper. Neal J. Evans II, Sarah Dodson-Robinson were the main supervisors for this work. Karen Willacy provided the chemistry code that this work is based on. Neal Turner provided useful comments.

## 3.1 Introduction

Solar System formation models that allow the giant planets to form within observed protostellar disk lifetimes of a few million years (Haisch et al., 2001) often require density enhancements up to an order of magnitude above the minimum-mass solar nebula (MMSN) (Pollack et al., 1996; Hubickyj et al., 2005; Thommes et al., 2008; Lissauer et al., 2009; Dodson-Robinson & Bodenheimer, 2010; D'Angelo et al., 2014). Indeed, planet accretion may be a fundamentally inefficient process, with both collisional fragmentation (e.g., Stewart & Leinhardt, 2012) and planetesimal scattering (e.g., Ida & Lin, 2004) contributing to mass loss during solid embryo growth. Yet disk masses inferred from dust emission in (sub)millimeter often do not reach the MMSN mass of $0.01 M_{\odot}$ (Weidenschilling, 1977; Hayashi, 1981), and are more commonly of order 1-10 Jupiter masses (Andrews & Williams, 2007; Williams & Cieza, 2011). Reporting on a survey of T-Tauri stars in Lupus, Ansdell et al. (2016) suggested that 80% of the disks had dust-derived total masses of $< 0.01 M_{\odot}$. However, dust-based disk mass estimates may be systematically low, because dust continuum observations lose sensitivity to solids that are much larger than the observing wavelength (Williams & Cieza, 2011). In addition, the standard assumptions that the dust has a single temperature and that the sub-mm emission is optically thin everywhere in the disk may not be correct. Finally, gas masses may not be related to the dust masses by the usual interstellar ratio of 100. It is essential to measure the gas mass of disks directly.

One such gas mass measurement came from Bergin et al. (2013), who used *Herschel* observations of the HD ($J = 1 \rightarrow 0$) transition to calculate a mass of $0.06 M_{\odot}$, or 6 MMSN, for the disk surrounding TW Hydra—a surprisingly large mass given the star age of $\sim 10$ Myr. The HD lines have since been detected in two more disks (McClure et al., 2016), and are consistent with gas masses of 1-4.7 MMSN (DM Tau) and 2.5-20.4 MMSN (GM Aur). Although the GREAT instrument on the far-IR observatory SOFIA[2] covers the frequency of the HD transition, it is not sensitive enough to observe HD in nearby disks. In the absence of the capability to observe the HD $J = 1 \rightarrow 0$ transition in disks, CO has been the standard tracer of the gas mass because it is believed to have simple chemistry and to stay in the gas phase wherever $T > 20$ K in disks around Sunlike stars (Öberg et al., 2011b; Qi et al.,

[2]https://www.sofia.usra.edu/

2013b), a region that includes the entire vertical column in the inner 30 AU and the warm surface layers of the outer disk. While the emission from $^{12}C^{16}O$ is typically optically thick, it has been suggested (van Zadelhoff et al., 2001; Dartois et al., 2003) that rare isotopologues of CO could be used to probe the disk midplanes. Yu et al. (2016) (hereafter Paper 1) have shown that the vertical optical depth of low-J rotational emission lines of $C^{17}O$ is around unity in the inner $\sim$ 20 AU of a 1.5-MMSN disk, meaning observers could see emission from the disk midplane—where most of the mass is concentrated—using $C^{17}O$ lines. Unfortunately, Paper 1 also revealed some complexities in the CO chemistry that would interfere with disk mass measurements. First, the CO abundance varies with distance from the star within the planet-forming region. Second, the $CO/H_2$ ratio drops to an order of magnitude below the interstellar value well inside the CO freeze-out radius because of chemical depletion of CO. Finally, the CO abundance is a function of time, which introduces an age-mass degeneracy into the interpretation of the observations.

Recent attempts to calculate gas-to-dust mass ratios using observations of rare CO isotopologues have also revealed problems. In their survey of disks in the Lupus star-forming region, Ansdell et al. (2016) found gas-to-dust ratios, calculated assuming a constant $CO/H_2$ ratio of $10^{-4}$, to be much lower than the interstellar value of 100. Yet the stars in the Lupus sample are still accreting, indicating that abundant gas is present. Studies of a more massive disk and star (2.3 $M_\odot$) also found very low gas-to-dust ratios (Boneberg et al., 2016). Correcting for the joint effects of freeze-out and isotope-selective photodissociation still does not bring the estimated gas-to-dust ratios up to 100, according to the chemical models of Miotello et al. (2017). Either the disks are in the process of dispersing—unlikely given the rapid depletion timescale of $\sim 10^5$ years once photoevaporation dominates the disk dynamics (e.g., Hollenbach et al., 2000; Alexander et al., 2014; Gorti et al., 2016)—or additional pathways to remove gaseous CO (hereafter referred to as chemical depletion) become important in disks, as suggested by Dutrey et al. (2003), Favre et al. (2013), Miotello et al. (2017), and McClure et al. (2016). Some disks around HAeBe stars also appear to have $CO/H_2 < 10^{-4}$ (e.g. Chapillon et al., 2008; Bruderer et al., 2012).

Also challenging the assumption of simple CO chemistry and a constant $CO/H_2$ ratio in regions where CO is not frozen out are the TW Hya observations of Schwarz et al. (2016), which show a drop in CO column density at $\sim$ 20 AU, while the dust column density remains roughly constant with radius. In Paper 1, we found that

CO chemical depletion due to dissociation by $He^+$ and subsequent complex organic molecule (COM) formation causes the $CO/H_2$ abundance ratio to drop far below the interstellar value of $10^{-4}$ at $r > 20$AU, well inside the CO freeze-out radius in the model (see figure 3.1). For disks with similar chemistry to the Paper 1 models, using interstellar abundance ratios to extrapolate from CO to $H_2$ column density would result in large underestimates of disk mass.

In this work we use radiative transfer models of CO rotational emission to assess the usefulness of rare CO isotopologues as disk mass indicators, given the possibility of chemical CO chemical depletion. We summarize the key results from our chemical evolution models in section 3.2, including a new model for a more massive disk. We present the setup for and results of our line radiative transfer models in section 3.3. In section 3.4, we demonstrate that standard gas-mass measurement methods—based on integrated fluxes of lines assumed to be optically thin—fail when applied to the simulated CO emission from our model disk. We also evaluate the performance of published optical-depth correction methods (Williams & Best, 2014; Miotello et al., 2016), showing that they are inadequate for disks with non-uniform CO abundance. In section 3.5 we further highlight the age-mass degeneracy problem caused by CO chemical depletion. Next we show that (1) combining observations of multiple isotopologues, (2) using information on line profiles, and (3) examining the spatial distribution of CO can diagnose CO chemical depletion (section 3.6). In section 3.7, we explore whether our predicted $CO/H_2$ abundance ratios can increase observed masses up to MMSN or higher when applied to the Lupus disk sample of Ansdell et al. (2016). Section 4.6 summarizes our results.

## 3.2 Disk Model

We adopt the chemical-dynamical model from Paper 1 as the basis for our line radiative transfer models. Paper 1 presented the chemical evolution of a $0.015\,M_\odot$ disk around a Solar-type star for 3 Myr. In this paper, we add a chemical evolution model for a disk that is twice as massive, at $0.03\,M_\odot$. The mass distributions and accretion temperatures of both model disks were presented by Landry et al. (2013), and we find the stellar contribution to the disk heating from the dust radiative transfer code

RADMC[3]. Because our goal is to measure disk masses in giant planet-forming regions, we focus our study on the region covered in Landry et al. (2013) – the inner 70 AU of the disk. (As the disk ages, the amount of mass in the inner 70 AU decreases due to viscous spearing and accretion – all disk masses reported in this paper are calculated as $\int 2\pi r\Sigma \, dr$, where $\Sigma$ is the column density, out to 70 AU.) The chemical reaction network is run locally at each independent (r, z) grid point for 3 Myr, under the assumption that the chemical reaction timescale is much shorter than the viscous timescale—an assumption that is true for freezeout, desorption, and grain-surface reactions, but which may fail for gas-phase reactions. Each disk gridpoint starts with gas and ice abundances resulting from a 1 Myr simulation of the chemical evolution of a parent molecular cloud; as a result, a substantial fraction of the carbon is tied up in $CO_2$ and other ices at the start of disk evolution.

The chemical evolution models include C, H, O, N based on the UMIST database RATE06 (Woodall et al., 2007). Woods & Willacy (2009) extended the network to include C isotopes, and we included both C and O isotopes in Paper I. The chemical models follow the chemistry of 588 species, 414 gas-phase and 174 ices, for 3Myr from the beginning of the T-Tauri phase. The reaction network contains gas-phase reactions (including those that lead to C and O fractionation), grain-surface reactions, freezeout, thermal desorption, and reactions triggered by UV, X-rays and cosmic rays, such as isotope-selective photodissociation. To make our simulations computationally tractable, we include only molecules with two or fewer carbon atoms, which limits the network to 11316 reactions. Some grain-surface hydrogenation reactions, such as $(C_2H_5\ ice) + H \rightarrow (C_2H_6\ ice)$, are not included because they only lead to sinks; we can save computational time by not computing the associated reaction rate and letting $C_2H_5$ ice be the sink instead of $C_2H_6$ ice.

The simplifications we have made to the reaction network do not artificially remove carbon from the gas phase. In Paper 1 we demonstrated that using a range of chemical networks, input chemical abundances and dust properties does not change the evolution of CO abundance significantly. We take the temperatures and abundances from the fiducial model in Paper 1 as the foundation for this study and refer readers to Paper 1 for detailed discussions of disk model assumptions. The most debatable assumption from Paper 1 is that abundances in gas and icy components

[3]http://www.ita.uni-heidelberg.de/ dullemond/software/radmc-3d/; developed by C. Dullemond

are inherited from the molecular cloud without modification as they enter the disk. Indeed, Drozdovskaya et al. (2016) suggest that disk midplane composition is largely determined by the conditions during cloud collapse. Visser et al. (2009b) find that CO ice formed in molecular clouds desorbs during cloud collapse, though it re-freezes without significant abundance modification where the disk temperature is $< 18$ K.

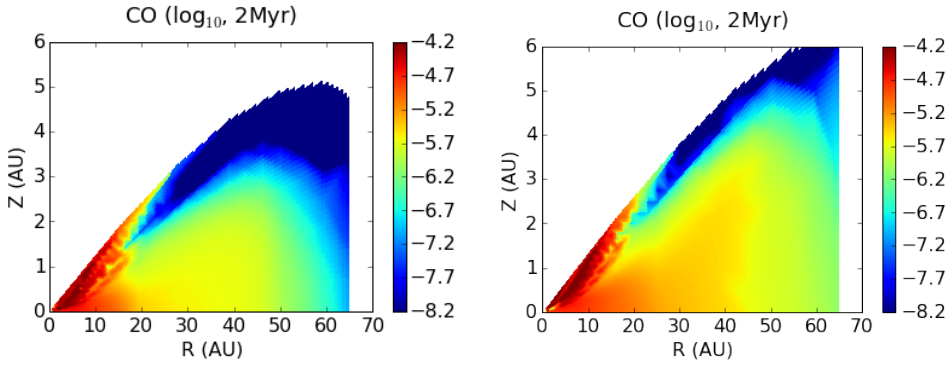


Figure 3.1: CO abundance as a function of disk radius (R) and height (Z) at 2 Myr. We show results from the $0.015\,M_{\odot}$ model on the left and the $0.03\,M_{\odot}$ model on the right. The abundance is defined as the number density with respect to the number density of hydrogen nuclei ($n_H + 2n_{H_2}$).

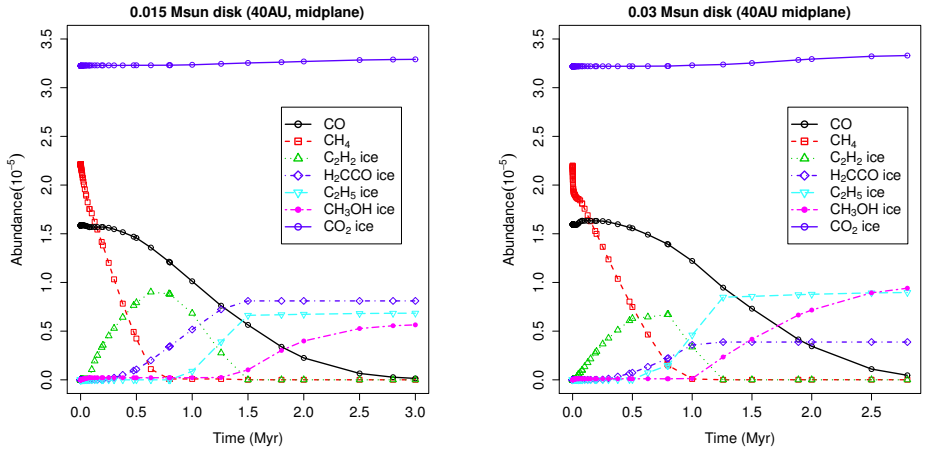


Figure 3.2: Abundances of major carbon-bearing molecules as a function of time at 40 AU on the disk midplane. We show results from the $0.015\,M_{\odot}$ model on the left and the $0.03\,M_{\odot}$ model on the right.

The disk is primarily heated passively from stellar irradiation; accretion con-

tributes very little to the energy budget (Landry et al. 2013, Paper 1). For the temperature calculation, we use the dust opacities computed by Semenov et al. (2003), adjusted for our gas/dust ratio. We assume the dust has already grown and aggregated at the start of the T-Tauri phase of disk evolution (Oliveira et al., 2010; Pérez et al., 2012; Birnstiel et al., 2011; Garaud et al., 2013), and 90% of the solids have grown to still larger sizes (pebbles, rocks, etc.), that contribute very little submillimeter emission. We distinguish these *solids* from *dust* and take a gas/dust mass ratio of 1000. In Paper 1, we demonstrated that the CO abundance is only weakly sensitive to evolution of the gas/dust ratio from 100 to 1000. Our grain model assumes that there is a constant replenishment of small grains by collisions between larger objects (see Dullemond & Dominik (2005); Brauer et al. (2008); Birnstiel et al. (2009); Wada et al. (2008, 2009); Windmark et al. (2012); though Zsom et al. (2010) argues against replenishing micron-size dust grains through collisions) and the size distribution of dust does not evolve. The theory that most of the solid mass has aggregated into pebbles and larger objects invisible to submillimeter wave observations is the second major, non-standard assumption in our model (though Andrews et al. (2012) and Cleeves et al. (2015) modeled the TW Hya disk with two distinct grain populations, small grains that provide the visible/infrared opacity and large grains with a maximum size of 1 mm that provide the submillimeter opacity). Following Cleeves et al. (2015), we assume the 90% of solid mass that has grown to pebble and larger sizes provides negligible surface area for chemical reactions and exclude it from the chemical model.

As the central star dims during its time on the Hayashi track, the disk cools and its scale height shrinks. The computational surface of our model grid, defined as the layer where the optical depth to the disk's own radiation is $\tau = 0.2$ (Landry et al., 2013), moves from about two pressure scale heights to about one scale height above the midplane as the disk becomes cooler and thinner over time. The chemical model therefore contains fewer grid cells at the end of evolution than at the beginning, as grid layers high above the midplane begin to empty out. In appendix 3.9, we show that our line profile and intensity calculations are only weakly sensitive to the changing disk surface.

Stellar heating is efficient enough to prevent CO from freezing out in our modeled region—the inner 70 AU of the disk—at all vertical heights and at any time in the 3 Myr of evolution. However, CO is depleted beyond 20 AU from the central star due

to the formation of complex organic molecules. The CO chemical depletion is driven by ionization of helium from X-rays and cosmic rays and happens over a million-year time scale. As a result, the CO abundance changes both with location in the disk and with time. We show the color map of CO abundance at 2 Myr of the disk evolution in Fig. 3.1 for both the Paper 1 disk (0.015 $M_\odot$; left) and the new model of the more massive disk (0.03 $M_\odot$; right). The abundance is defined as the ratio of the number density of CO with respect to the number density of hydrogen nuclei ($n_H + 2n_{H_2}$). After 2 Myr, the CO chemical depletion front moves inward to 20 AU, with the surface layers more depleted than the disk midplane. Fig. 3.2 shows the abundances of major carbon-bearing species as a function of time for the midplane at 40 AU in each disk, demonstrating the gradual chemical depletion of CO and subsequent sequestration of carbon into organic ices. We note that our network is not extensive enough to determine the exact end-product of organic ice formation. The most complex hydrocarbon we include is $C_2H_5$, which in reality should hydrogenate to form ethane, and radicals of the form $C_2H_x$ should react with carbon atoms or hydrides to form longer carbon chains. However, these complex products of organic grain surface chemistry are all less volatile than the $C_2H_x$ species and would stay on the grain surfaces unless the grains drift radially inward (e.g. Birnstiel & Andrews (2014)) or experience a transient heating event (e.g. Cody et al. (2017); Cieza et al. (2016a); Vorobyov & Basu (2015)). Since almost all resolved T-Tauri disks detected in dust continuum emission have radii much larger than the $\sim$ 40 AU $C_2H_5$ ice line (Paper 1) in our models[4], we do not expect radial drift to deposit a significant amount of organic gas that could be recycled to form CO in the inner disk. To the extent that there are real astrophysical disks that evolve quiescently during the T-Tauri phase, our conclusion that carbon liberated by CO chemical depletion becomes sequestered in ices is robust. The more massive disk shows a similar pattern of CO chemical depletion to the disk presented in Paper 1, though the depletion timescale is a bit longer because the higher column density decreases the ionization fraction—and thus the abundance of ionized helium—in the midplane.

The net result of all chemical models presented here and in Paper 1 is that CO becomes severely depleted well inside the CO freeze-out radius in disks with masses above the minimum needed to form planetary systems. Similar effects have been seen

[4]See the catalog of resolved disk images at www.circumstellardisks.org

in other chemical evolution calculations (Aikawa et al. 1997, 1999; Furuya & Aikawa 2014; Walsh et al. 2014; Bergin et al. 2014). Aikawa et al. (1997) and Aikawa et al. (1999) first pointed out that CO can react to form less volatile molecules such as $CO_2$, HCN, $H_2CO$, $CH_4$ and larger hydrocarbons over Myr timescales. Aikawa et al. (1997) used a static disk (not evolving), and Aikawa et al. (1999) used a vertically isothermal model and found a larger number of simple molecules as products (as opposed to a few complex molecules), but the essence of the chemical depletion of CO is the same as found here and in Paper 1. Walsh et al. (2014) simulated the composition of complex organic molecules in a disk with no temperature evolution for about 1 Myr and found the formation of complex organic molecules in the disk midplane via grain-surface reactions, while Bergin et al. (2014) found gas-phase organic formation and subsequent freezeout onto grain surfaces. Furuya & Aikawa (2014) investigated the carbon and nitrogen chemistry during turbulent mixing, and found that volatile transport enhances COM formation near the surface and suppresses it in the disk midplane. It is difficult to compare our results directly with the earlier calculations because our models have different central star properties and less accretion heating, but it is clear that a variety of chemical processes can force a disk's $CO/H_2$ abundance ratio far from the interstellar value.

In Figure 3.3 we show the fraction of our model disk's carbon atoms contained in CO gas ($f_{CO}$) as a function of time. The fraction is initially low because evolution in the molecular cloud has sequestered carbon in ices; for a while these evaporate, increasing $f_{CO}$, but then CO chemical depletion and formation of icy organics cause $f_{CO}$ to decrease. To complicate matters, the abundance of CO actually increases with time at small radii, as $CO_2$ ice desorbs and dissociates to form CO gas. Although the $0.015\,M_\odot$ disk suffers more CO chemical depletion at larger radii, the re-formation of CO gas in the inner disk also proceeds at a higher rate than in the $0.03\,M_\odot$ disk, leading to a higher disk-averaged $f_{CO}$ for the $0.015\,M_\odot$ disk. These facts will compromise attempts to measure disk masses using CO isotopes (§3.4). Worse yet, the CO abundance is a function of time, leading to an age-mass degeneracy in interpreting observations (§3.5).

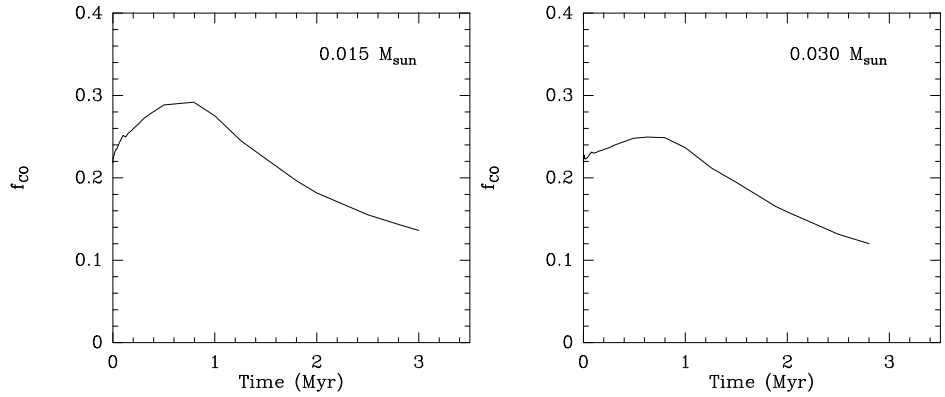


Figure 3.3: The fraction of C in CO versus time, averaged over the disk, for both the disks, 0.015 $M_\odot$ on the left, 0.030 $M_\odot$ on the right.

## 3.3 Line radiative transfer model and mass estimates

In order to understand the effects of chemical evolution on CO emission, we set up radiative transfer models with the publicly available code LIME (LIne Modeling Engine; Brinch & Hogerheijde, 2010). LIME calculates either non-LTE or LTE line excitation and solves the radiative transfer problem for molecular gas in arbitrary 3D geometries. For recent examples of studies using LIME, see Walsh et al. (2016) and Öberg et al. (2015). We adopt the energy levels from the Leiden Atomic and Molecular Database (LAMDA)[5]. As a first order approximation, we do not consider the hyperfine splitting in $C^{17}O$ emission.

As in Paper 1, we model emission from within a radius of 70AU of the central star, which corresponds to a 1 arcsec beam diameter for an assumed distance of 140pc from the Sun. We consider line broadening due to Keplerian rotation, thermal velocity and micro-turbulence. Thermal velocities are calculated assuming a Maxwell-Boltzmann speed distribution based on the disk's temperature structure from Paper 1. For the micro-turbulence, we again assume an isotropic Maxwell-Boltzmann speed distribution with RMS of 100m/s, consistent with the upper limit to microturbulent speed found by Flaherty et al. (2015b) in a fit to multiple CO emission lines in the HD 163296 disk. For computing the level populations, we set a minimum scale of 0.07AU to guarantee sub-pixel sampling of both Keplerian speeds and CO abundance

[5]http://home.strw.leidenuniv.nl/ moldata/

gradients. We first generate the synthetic datacube of intensity as a function of $x$, $y$, and velocity for a disk around a $0.95\,M_{\odot}$ star at 30° inclination, similar to the disk surrounding AS 209. In velocity space, the spectra have 300 channels of 125m/s resolution. At any specific velocity, the synthetic image contains $600 \times 600$ pixels of $0.003'' \times 0.003''$ in size. Finally, we generate the synthetic spectra presented here by integrating each velocity component over a square with $1.2''$ sides ($400 \times 400$ pixels), larger than the angular size of the disk. The pixels not covered by the disk contribute no flux and are included simply for ease of integration—here we assume that the sky background contains negligible flux compared with the disk at all wavelengths.

Our current models assume that the gas temperature is the same as the dust temperature. This is a valid assumption in estimating the optical depth of $C^{17}O$ and $C^{18}O$, as done in Paper 1, because the emission primarily comes from disk midplane and the midplane is strongly shielded from UV radiation. However, hot gas on the disk surface is more emissive, and we would need to consider the difference between the gas and dust temperature in order to use our models to fit high-J spectral lines emitted from the disk surface. Similarly, we would need to revisit the temperature calculation for a disk surrounding a star with a stronger UV field, which could decouple the gas and dust temperatures. In Appendix 3.9, we demonstrate that the LTE approximation is adequate for computing the energy level populations, and show that the decreasing disk scale height has little effect on the computed line profiles (see §3.2). For our purposes, we have adequately modeled the CO rare isotopologue emission, even though our models do not extend vertically to a large number of scale heights. For the rest of the paper, we focus our line profile discussion on $J = 3 \rightarrow 2$ and $J = 2 \rightarrow 1$, which are the most commonly observed transitions.

Figure 4.2 shows one set of results from our line radiative transfer models—the time evolution of the $J = 3 \rightarrow 2$ line profiles for three isotopologues and two model disks. Line profiles in Janskys are plotted as well as *normalized* profiles, which better show the evolving *shape* of the lines (see §3.6.2 for more on diagnosing CO chemical depletion by comparing line profiles from multiple isotopologues). Figure 3.5 shows the total intensities (integrated in velocity space) of $J = 3 \rightarrow 2$ emission from all CO isotopologues as a function of time. The decline with time is quite dramatic, especially for the rarer isotopologues where it exceeds an order of magnitude over 3 Myr. The emission from rarer isotopologues is very weak at later times, which can be expensive to observe, especially if one wants to achieve enough signal-to-noise to

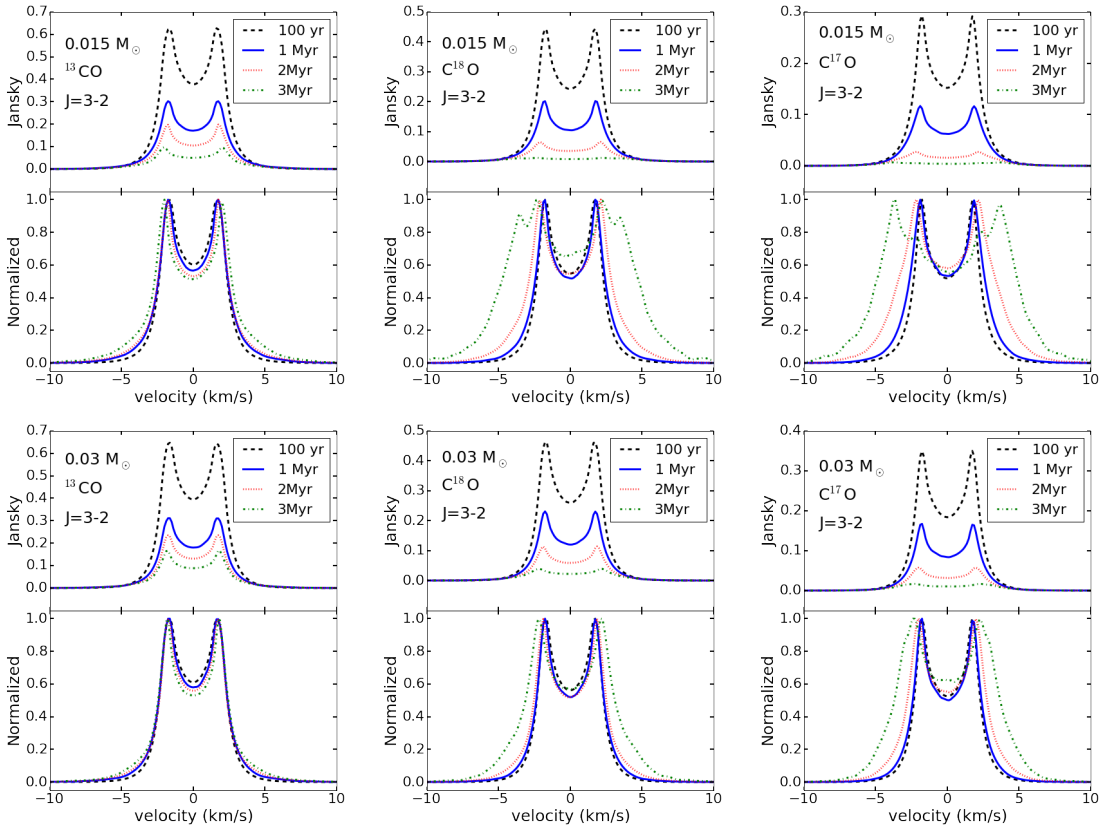


Figure 3.4: Time evolution of emission line profiles, with $^{13}$CO on the left, C$^{18}$O in the middle and C$^{17}$O on the right. The top 6 panels show results for the fiducial 0.015 $M_\odot$ model, and the bottom 6 panels show the results for the comparison 0.03 $M_\odot$ model. In each group, the top panels show the simulated lines, and the lower panels show the line profiles normalized to the peak intensity of each line. The emission becomes weaker, and the line profile becomes wider over time for all isotopologues, but the change is much more significant for the optically thin C$^{18}$O and C$^{17}$O emission.

study the line profiles.

Finally, we use standard observational procedures to try to recover the apparent masses of the disks, as an observer would do. Here we will use the $J = 2 \rightarrow 1$ line, as it is commonly used to obtain disk masses (e.g.,Williams & Best 2014, though Ansdell et al. (2016) use the $J = 3 \rightarrow 2$ line). We show in Appendix 3.11 that higher $J$ transitions underestimate the mass more severely than $J = 2 \rightarrow 1$ and $J = 3 \rightarrow 2$. From our model line profiles we calculate level populations, total number of CO molecules, and finally gas mass. The equations used to derive the number of CO molecules in each energy level ($\mathcal{N}_J$) from integrated line flux, assuming optically thin

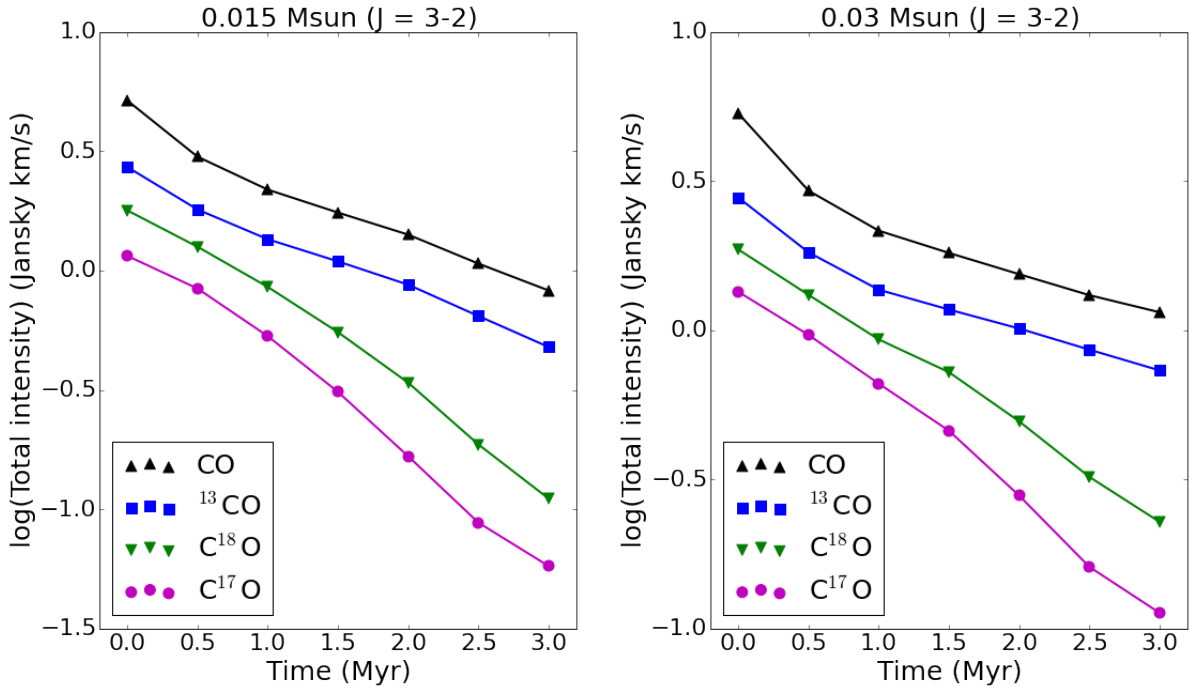


Figure 3.5: Total intensities of J=3 − 2 emission from various CO isotopologues as a function of time. Results from the fiducial with $0.015\,M_\odot$ are presented on the left, and those from the fiducial model with $0.03\,M_\odot$ are presented on the right. In the $0.015\,M_\odot$ model, the intensity of $^{13}$CO drops from $2.72 \mathrm{Jy} - km\ s^{-1}$ by 82% to $0.48 \mathrm{Jy} - km\ s^{-1}$ over the 3 Myr disk evolution, and the intensity of C$^{17}$O drops from $1.15 \mathrm{Jy} - km\ s^{-1}$ by 95% to $0.06 \mathrm{Jy} - km\ s^{-1}$.

emission, are given in Appendix 3.10. Values of $\mathcal{N}_J$ can then be translated to mass with the following equations. The total number of CO molecules in the disk $\mathcal{N}$ is given by

$$\mathcal{N} = \frac{\mathcal{N}_J}{g_J} \times Q \times e^{E_{\mathrm{up}}/T} \tag{3.1}$$

where $E_{\mathrm{up}}$ is the upper-state energy of the transition in K and $Q$ is the partition function, generally approximated by $Q = kT/hB$ (with $B$ in Hz). Note that the temperature of the CO reservoir appears in both the exponential and the partition function in Equation 3.1; in Appendix 3.11.1 we show that no single temperature describes the CO reservoir. We then compute the mass of gas from

$$M = \frac{\mathcal{N} \mu_{\mathrm{H}} m_{\mathrm{H}} f_{iso}}{f_{\mathrm{C}} f_{CO}} = 1.668 \times 10^{-53} \mathrm{M}_\odot\ \mathcal{N} f_{iso}/f_{CO} \tag{3.2}$$

where $\mu_{\mathrm{H}}$ is the mean atomic weight of the ISM including He, $m_{\mathrm{H}}$ is the mass of a

hydrogen atom, $f_{iso}$ is the ratio of the mass of the most common isotopologue ($^{12}C^{16}O$) to that of the one being used, $f_C$ is the abundance ratio of carbon to hydrogen nuclei, and $f_{CO}$ is the fraction of C in CO, averaged over the disk. $\mu_H = 1.43$ and our chemical model has $f_C = 7.21 \times 10^{-5}$.

In the next section we describe how equations 3.1 and 3.2 to obtain the correct mass of our model disk.

## 3.4 Even rare CO isotopologues underestimate disk mass

$^{12}C^{16}O$ and $^{13}C^{16}O$ will be optically thick in disks, so the usual approach is to observe rarer isotopologues. At first glance, the CO chemical depletion we predict might be expected to ameliorate optical depth problems, but the concentration of CO to small radii increases optical depths there. At the same time, the chemical depletion of CO at larger radii causes mass underestimates by lowering the value of $f_{CO}$. The net result is that simple analysis fails for the following reasons.

First, the usual assumption is that $f_{CO} = 1$ inside the CO ice line, but our models challenge that assumption. Figure 3.3 shows how $f_{CO}$ varies with time, never rising above 0.3 (0.015 $M_\odot$ disk) or 0.25 (0.03 $M_\odot$ disk) and approaching 0.12 by 3 Myr. Since our disk does not include radii where CO itself would freeze, the low $f_{CO}$ is due to what we call chemical depletion. Alone, with no other error sources in equations 3.1 and 3.2, it will cause underestimates of disk mass by factors of 3 to 8.

Second, the concentration of CO toward the inner disk means that temperatures, and hence partition functions, are higher than usually assumed for much of the CO reservoir. The most common assumption for temperature is $T = 20$ K (e.g., Ansdell et al. 2016). A temperature averaged over the the model disk and weighted by the number density of CO molecules ranges from 50 to 70 K, decreasing as the star and disk evolve, but stabilizing around 55 K for the 0.015 $M_\odot$ disk after about 1 Myr because the increasing concentration of CO in the inner disk counteracts the dropping luminosity of the star (Figure 3.6). If CO chemical depletion is operating in the outer disk, assuming $T = 20$ K for the gas where CO is concentrated is never a good choice; it will systematically underestimate masses by a factor of about 2. In disks around T-Tauri stars that are less luminous than the proto-sun at 3 Myr, or

that receive a low cosmic-ray flux so that cosmic ray-induced photons do not generate CO from $CO_2$ gas in the inner disk, 20 K may be appropriate, but we recommend constructing model-based temperature estimates for the CO reservoir rather than making any assumptions. As a further complication, we show in Appendix 3.11 that rotation diagrams from multiple transitions are not effective in determining the best temperature to assume.

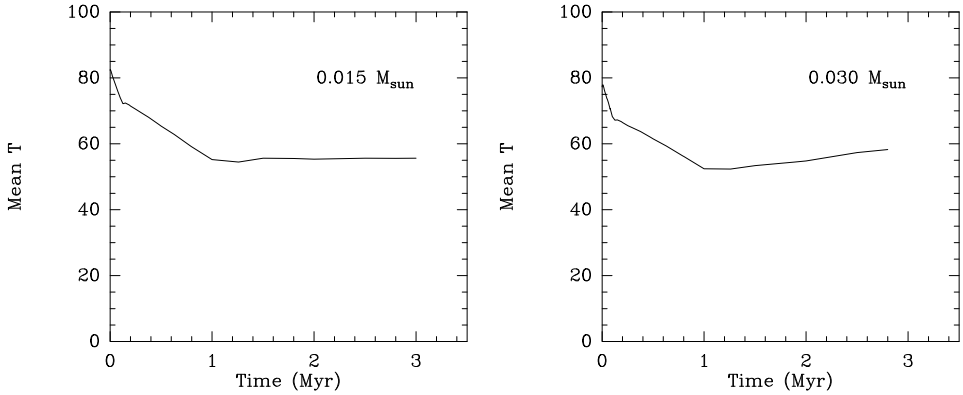


Figure 3.6: The temperature versus time, weighted by the CO density, and averaged over the disk, for both the disks, 0.015 $M_\odot$ on the left, 0.030 $M_\odot$ on the right.

Third, the increase in CO abundance in the inner disk causes optical depth effects where most of the CO actually resides (see Fig. 10 of Paper 1). Even if we correct for the mean $f_{CO}$ and somehow find an accurate value of $T$ averaged over the CO reservoir, the standard analysis still underestimates the mass. Figure 3.7 shows the mass estimates from different isotopes and analysis procedures versus time, along with the actual disk mass, which decreases slightly due to disk spreading and accretion onto the star. The estimates with black symbols are computed with equations 3.1 and 3.2 and based on the assumption of optically thin emission in the $J = 2 \rightarrow 1$ line of the listed isotopologues. They all use the correct $f_{CO}$ and the mass-weighted CO temperature for our model—information that would not be available for astronomical sources—yet they all still underestimate the gas mass substantially. The rarer isotopologues perform best, suggesting that optical depth is the main culprit. The recent analysis of the Lupus disks (Ansdell et al., 2016) by Miotello et al. (2017) also suggests optical depth effects, even after ratios of $^{13}$CO and C$^{18}$O were used to correct for optical depth. The apparent gas to dust ratio declines with increasing dust mass in their Figure 6; if the dust mass is a reasonable proxy for disk mass, a more

massive disk will have larger (and more complicated) effects from optical depth. Our results indicate that models that do not account for the radial dependence of $f_{CO}$ will underestimate the gas mass more severely for more massive disks, as observed in Figure 6 of Miotello et al. (2017).

### 3.4.1 Correcting for optical depth using multiple isotopologues

One approach to dealing with optical depth is to observe the same rotational transition in multiple isotopologues (e.g., Williams & Best, 2014; Miotello et al., 2016). We tried a simple correction for our $^{13}$CO-based mass estimate by comparing with C$^{18}$O, using the C$^{18}$O/$^{13}$CO line intensity ratios plus the initial isotope ratios from the chemical model. This correction yielded the hollow green hexagons in Figure 3.7, which still underestimate disk mass badly, performing only as well as C$^{18}$O observations would on their own.

More sophisticated optical depth corrections can be made with fitting formulae that relate the $J = 2 \rightarrow 1$ line intensity of either $^{13}$CO or C$^{18}$O (or their ratio) to the total disk mass, based on a suite of models (e.g., Williams & Best, 2014; Miotello et al., 2016). We placed our model line luminosities on Figure 3.7 (left panel) of the Williams and Best models to estimate mass, producing the red points, which have no correction for $f_{CO}$. They do well for early times when the CO is more uniformly distributed over the disk, but underestimate the mass badly at later times when $f_{CO}$ drops especially at larger radii. Most of our points lie near the top of their distribution of models, and interpolation between mass models is uncertain by a factor of three. Second, we used the formulae in equation 2 with coefficients in Table A.1 of Miotello et al. (2016) to estimate disk mass from luminosities of the $J = 2 \rightarrow 1$ lines of $^{13}$CO and C$^{18}$O. Those from $^{13}$CO underestimated the mass badly, but those from C$^{18}$O did better (blue octagons). In these comparisons, we adjusted their mass estimates to be consistent with our assumption about the atomic carbon abundance, but not for the fraction of carbon in CO. In a recent paper, Miotello et al. (2017) find the same result; applying their models to the Lupus data (Ansdell et al., 2016) data leads to very low gas to dust ratios (less than 10 in most cases) unless CO is depleted. The Miotello et al. grid of chemical models was optimized to treat CO self-shielding and isotopic fractionation, which our chemical models also include; the low gas/dust

ratios implied by $C^{18}O$ and $^{13}CO$ observations must result from other CO-depletion pathways.

Clearly, both optical depth and CO chemical depletion must be accounted for when measuring disk masses: Figure 3.7 shows that measurements incorporating one correction, but not the other, will fail. For masses based on a single emission line, so that no optical depth correction is possible, the isotopotologue that performs the best is $C^{17}O$, which underestimates the mass by a factor of 2-3 if the correct value of $f_{CO}$ is known (which it will not be in real astrophysical situations). In Appendix 3.11, we show that the $J = 1 \rightarrow 0$ line does much better than the more commonly used $J = 2 \rightarrow 1$ or $J = 3 \rightarrow 2$ lines. We believe that this is primarily due to its lower optical depth and lesser sensitivity to temperature.

The combination of the models of Miotello et al. (2016) and our calculations of $f_{CO}$ would improve the mass estimates. For example, if we use our "insider information" (i.e. model-derived knowledge) about $f_{CO}$ as a function of time for our 0.015 $M_\odot$ disk to further correct the masses from the formulae in Miotello et al. (2016), the resulting masses are accurate to within a factor of two at all ages. Unfortunately, to apply this method to observations, one needs to know the disk age. We explore the issues arising from that fact in the next section.

## 3.5 The Age-Mass Degeneracy

The time dependence of the fraction of C in CO (see Fig. 3.3) implies that one needs to know the disk age to apply a mass correction factor. Ages of host stars are not generally known to better than $\pm 1$ Myr. Worse yet, the "age" in our models is in some sense a chemical age because the speed of chemical evolution will depend on the ionization sources. EXor outbursts and X-ray flares may also introduce brief periods of intense ionization (e.g. Audard et al., 2014). If we don't know the chemical age, there is an age-mass degeneracy—a massive, old disk may look similar to a young, less massive one in CO rare isotopologue emission. Figure 3.8 shows an example of the age-mass degeneracy. The more massive disk reaches the same $C^{18}O/^{13}CO$ total intensity ratio about 0.5 Myr later than the less massive disk for both $J = 3 \rightarrow 2$ and $J = 2 \rightarrow 1$.

CO-based mass measurements are further complicated by the fact that the de-

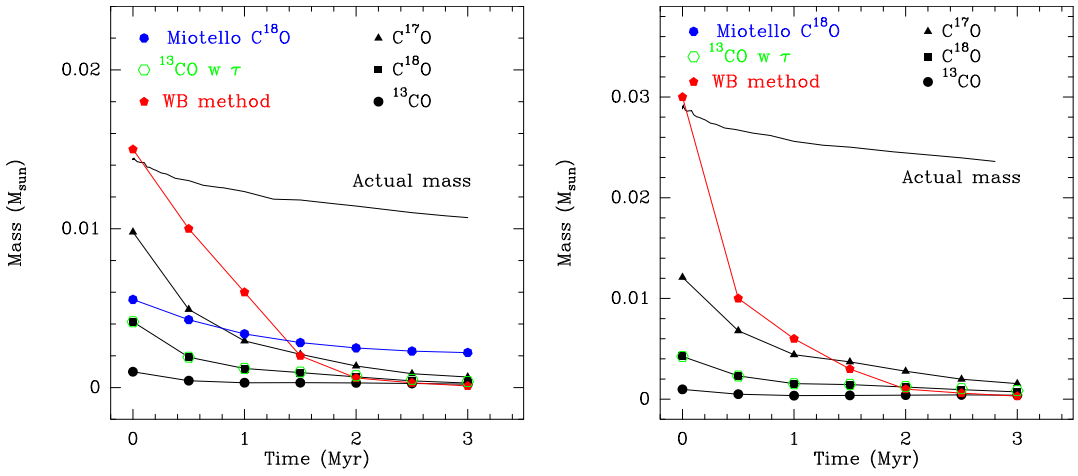


Figure 3.7: The mass of the disk inferred from the simulated observations is plotted versus time. The actual mass is shown as a solid line, while the masses inferred from equation 3.2 and the simulated emission from different isotopes and using different analysis methods are shown as points. Colored points show mass estimates corrected for optical depth but not $f_{CO}$, while black points show masses corrected for $f_{CO}$ but not optical depth. Labels are explained in the text.

pletion occurs in the outer disk, where most of the mass resides. The decline in CO isotopologue line intensity as a function of time is precipitous: in the $0.015\,M_{\odot}$ model, the intensity of $^{13}$CO J=3-2 emission drops from $2.72 Jy - km\ s^{-1}$ by 82% to $0.48 Jy - km\ s^{-1}$ over the 3 Myr disk evolution, and the intensity of C$^{17}$O J=3-2 drops by 95% from $1.15 Jy - km\ s^{-1}$ to $0.06 Jy - km\ s^{-1}$ (Fig. 3.5). For comparison, the total disk mass within 70 AU of the star drops by about 12% over 3 Myr and $f_{CO}$ drops by a factor of 2-3. Clearly, a simple correction for $f_{CO}$ does not capture all of the decrease in line emission with time. Without a good model of CO abundance as a function of radius and time, line-intensity measurements yield disk mass estimates that are accurate to factor of two at best and are systematically underestimated.

## 3.6 Diagnosing CO chemical depletion

In section 3.2 we demonstrated that the CO abundance decreases with both radius and time. In Section 3.4, we showed that other effects add to the underestimation of disk mass and that the underestimate gets worse with age. Given that star ages can be uncertain by over 1 Myr (e.g., Soderblom et al., 2014)—the timescale over which

we observe CO depletion in our model—interpreting CO observations requires a more direct CO chemical depletion indicator than the star age. The need for a disk-based CO chemical depletion indicator is especially evident given the likelihood that disks with different masses or incident cosmic-ray fluxes may evolve at different speeds.

We explore here three types of observations that can diagnose CO chemical depletion . First, isotopologue intensity ratios for a transition change with time, revealing departures from the ISM $CO/H_2$ ratio. Second, line profile shapes for the most optically thin isotopologues, $C^{17}O$ and $C^{18}O$, widen over time as the outer disk loses CO, while $^{13}CO$ and CO profile shapes evolve very little. Third, spatially resolved observations will reveal CO chemical depletion patterns. While using intensity ratios to diagnose CO chemical depletion requires less observing time, high signal-to-noise line profiles or spatially resolved observations contain valuable information that could allow observers to reconstruct the radial distribution of CO gas. We present all three strategies here, beginning with intensity ratios.

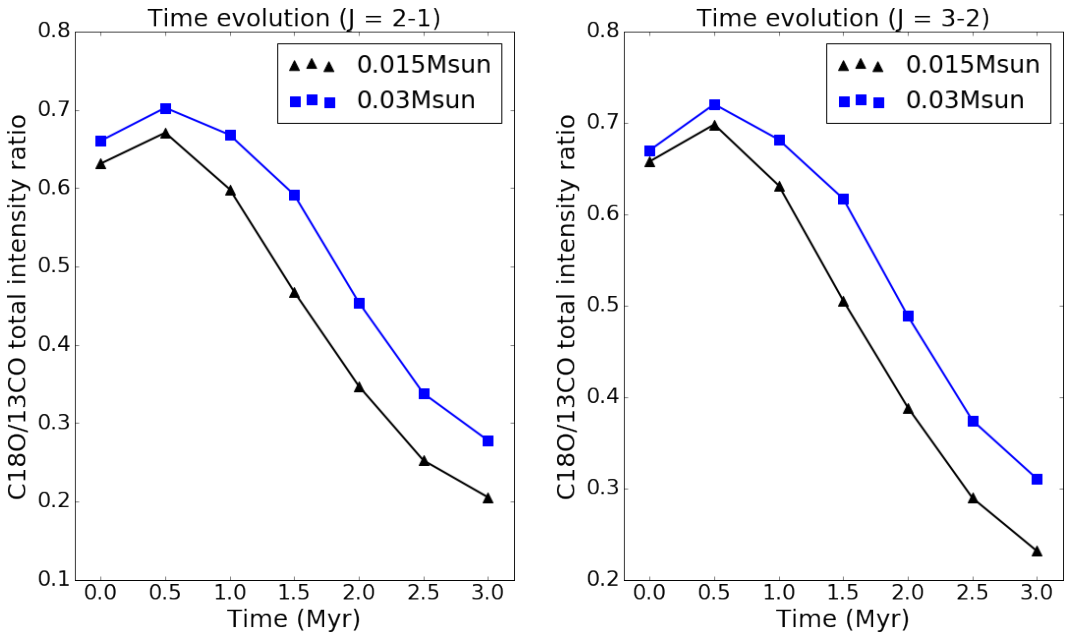


Figure 3.8: Ratio of total intensities of $C^{18}O$ and $^{13}CO$ lines from for the $0.015\,M_\odot$ and the $0.03\,M_\odot$ disks. We show the results for the J=2 − 1 lines on the left, and those for J = 3 − 2 lines on the right.

### 3.6.1 How intensity ratios reveal CO chemical depletion

The relative strengths of emission lines for different isotopologues change significantly over time. This is because different isotopologues react to the change in CO abundance differently due to their various optical depths. Re-examining Figure 3.8, we see that after 1Myr , the $C^{18}O/^{13}CO$ intensity ratios decrease steadily as the disk-averaged CO abundance declines monotonically (Fig. 3.3). One could use Figure 3.8 to estimate the chemical age of an observed disk. However, the predicted intensity ratios are higher for the more massive disk, so there is still a 0.5 Myr uncertainty in age, which propagates into a mass uncertainty.

Intensity ratios are the most rudimentary diagnostic of CO chemical depletion. Williams & Best (2014), Miotello et al. (2014), and Miotello et al. (2016) show how isotope-selective photodissociation, varying disk radii, and CO freezeout (or lack thereof) can affect intensity ratios, leading to a wide dispersion of $C^{18}O/^{13}CO$ for disks of the same mass.

### 3.6.2 How line profiles reveal CO chemical depletion

The line profiles contain information not available in the integrated intensities. Here we demonstrate how a comparison of normalized line profiles from $^{13}CO$ and $C^{18}O$ or $C^{17}O$ can diagnose CO chemical depletion, even over a factor of two range in disk mass. Figure 4.2 shows that the normalized line profiles of the rarer isotopologues become broader than those of the more common isotopologues as time proceeds. Since CO chemical depletion happens primarily in the outer part of the disk where Keplerian velocities are small, the fraction of radiation in the high-velocity line wings increases with time for optically thin lines. Optically thick lines can mask CO chemical depletion: the CO column density has to first decline to the $\tau \approx 1$ threshold (where $\tau$ is the optical depth in the line center) before intensity changes start to track abundance changes. For the $0.015\,M_\odot$ disk, the optically thin $C^{17}O$ and $C^{18}O$ emission tracks the changes in CO column densities well, so that the line profile gets significantly broader after 1 Myr. $^{13}CO$ ($J = 3 \rightarrow 2$) emission is optically thick well beyond the CO chemical depletion radius of $\sim$ 20AU, so does not reveal reductions in CO column density with time. Similar trends are found for the $0.03\,M_\odot$ disk. Because of the relatively high column densities, the change in $C^{18}O$ line profile is not

obvious until 3Myr , but $C^{17}O$ still tracks the reductions in CO column density very well. Clearly, line profiles of rare isotopologues can diagnose CO chemical depletion .

However, emission line profiles reflect not only the $CO/H_2$ abundance ratio, but the temperature and density structure of the disk as well. The temperature of our model disk decreases with time due to the young star's dimming as it moves down the Hayashi track, and the density structure changes as the disk viscously evolves. To isolate the effect of CO depletion from density and temperature effects, we set up control models with a constant $CO/H_2$ ratio throughout the disk and compare the emission line profiles produced by these with those produced by our fiducial, CO-depleted models. In the constant $CO/H_2$ models, all atomic carbon available for gas-phase reactions is assumed to be in CO, and relative abundances of CO isotopologues are determined only by the abundance ratios of the isotopes (see Table 2 of Paper 1). The abundances normalized to the total proton density are $7.21 \times 10^{-5}$ for CO, $9.34 \times 10^{-7}$ for $^{13}CO$, $1.44 \times 10^{-7}$ for $C^{18}O$, and $3.13 \times 10^{-8}$ for $C^{17}O$.

Figure 3.9 shows side-by-side normalized line profiles for the 0.015 $M_\odot$ disk with evolving chemistry and the one with constant $f_{CO}$. By 2 Myr, the profiles of rare isotopologues are noticeably wider than those of more common isotopologues and by 3 Myr, they are quite distinctive. These line profiles comparisons would provide clear evidence for ongoing CO chemical depletion and a potential way to correct for it (though there may be multiple rings of gas in some disks, which would complicate the line profile analysis; see Cleeves 2016). However, the actual (un-normalized) lines are very weak (Fig. 4.2), so diagnosing CO chemical depletion by comparing line profiles would be an expensive method in terms of observing time. Furthermore, variation in turbulent speeds between different layers of the disk could also produce different line profiles for $^{13}CO$, $C^{18}O$, and $C^{17}O$ (Flaherty et al., 2015b; Simon et al., 2015b), an effect we have not explored here.

### 3.6.3 Spatial distributions of CO isotopologues

Our chemical evolution models also predict a characteristic radial dependence of the CO abundance. To translate this dependence into observables, we average the velocity-integrated, continuum-subtracted emission from our model disks in rings of 2 AU in radius, and compare the spatial distributions of the $J = 2 \rightarrow 1$ emission line from the fiducial models to that from the constant CO models in Figure 3.10. The

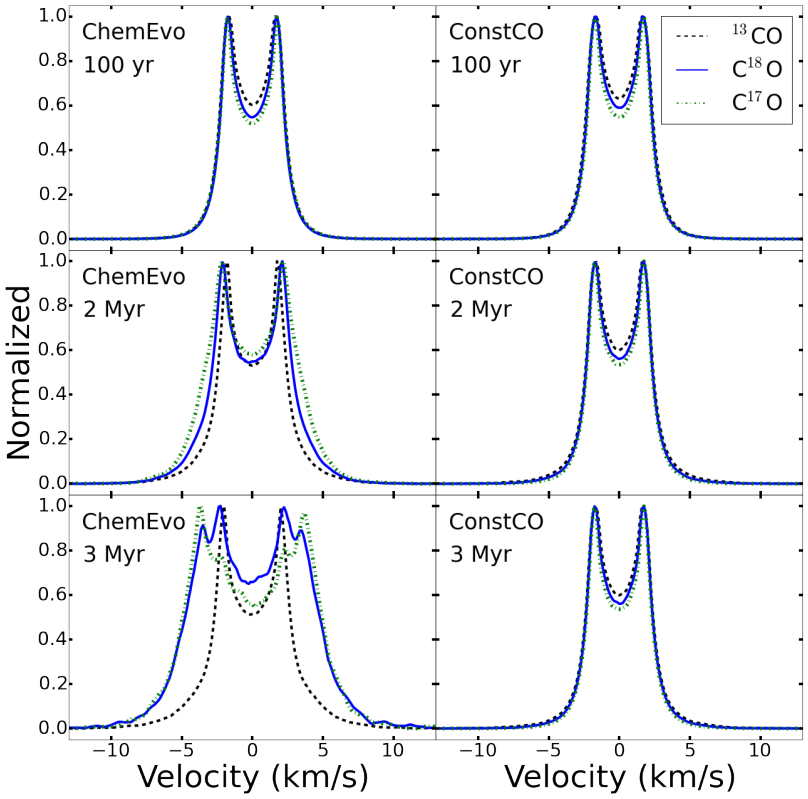


Figure 3.9: A comparison of normalized emission line profiles for various isotopologues are shown for the chemical evolution model and the constant CO model. In the constant CO model, all carbon available for gas phase reactions is assumed to be in CO, and abundances of CO isotopologues are assumed to be determined by atomic abundances of the isotopes.

models shown in Figure 3.10 were run in face-on geometry for simplicity; all other simulated emission in the paper is calculated for 30° inclination. The optical depth effects are enhanced in the face-on disks because the lines are not spread out by rotation. If a disk inclination angle is known, models could be run for that situation.

Results from the fiducial $0.015\,M_{\odot}$ disk are presented in the upper-left (early time), upper-right (2 Myr), and lower-left (3 Myr) panels. At the beginning of the evolution, the integrated intensities are lower in the fiducial model but the profiles are very similar to those in the constant CO disk for all isotopes. This is because part of the carbon is locked in $CO_2$ in the fiducial model, whereas the constant CO model has all available carbon in CO. As the disk evolves, the intensities beyond 20 AU decrease dramatically in the fiducial model due to the depletion of CO, and the differences

between the fiducial model and the constant CO model are the greatest for $C^{17}O$ lines, which have the lowest optical depth. We see sharp drops of intensity in models with $0.03\,M_\odot$ (lower right) as well. However because the chemical depletion happens more slowly in the $0.03\,M_\odot$ disk, the intensity profiles at 3 Myr of the $0.03\,M_\odot$ disk resemble those of the $0.015\,M_\odot$ disk at 2 Myr.

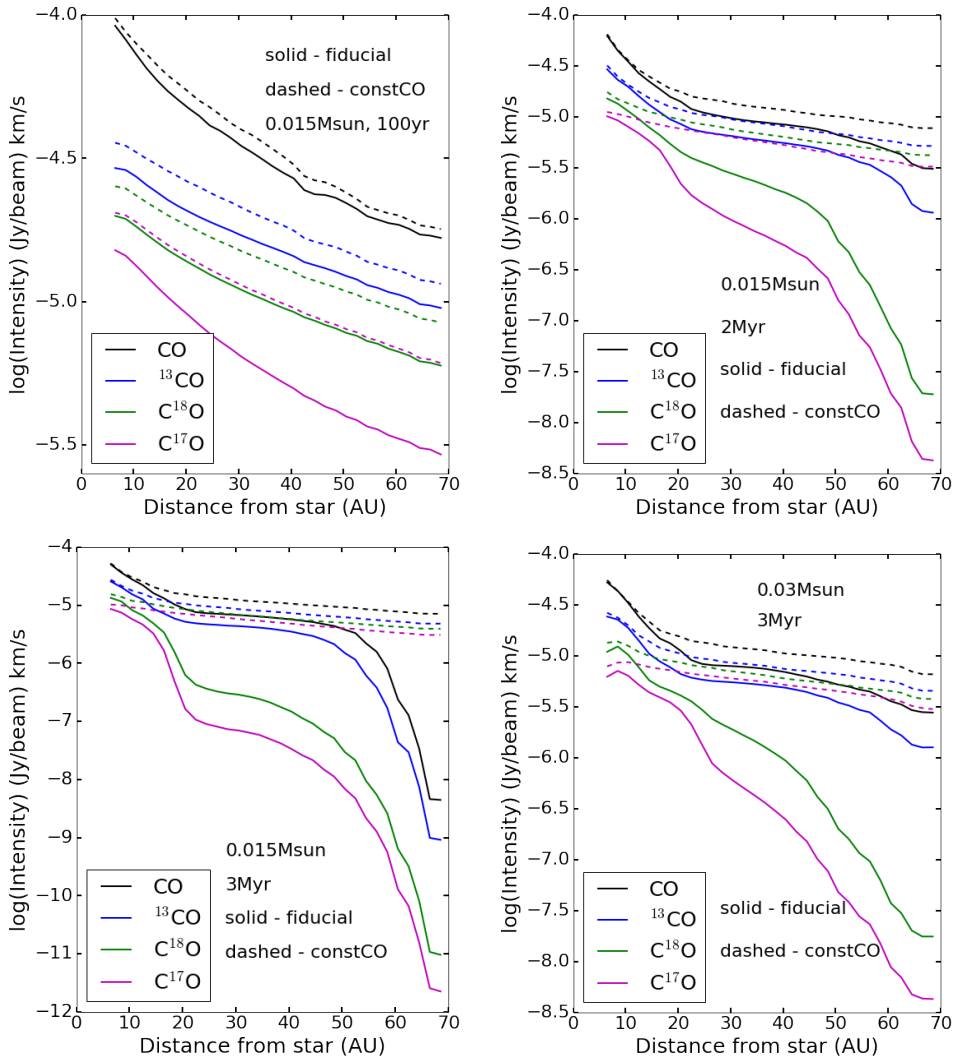


Figure 3.10: Logarithm of the azimuthally averaged, velocity-integrated intensities of the $J = 2 \rightarrow 1$ line as a function of radius. For a 10 km baseline, ALMA has a 0.″03 resolution for the $J = 2 \rightarrow 1$ line.

The effect of age is detectable with ALMA given enough integration time. We plot the time evolution of $^{13}$CO and C$^{18}$O lines for the 0.015M$_\odot$ disk in Figure 3.11,

and the detection limit as a horizontal line at log $= -6.27$. At resolution, we get to 540 mJy in 1 km/s resolution in 10 hours. At 0.″03 spatial resolution, with a velocity channel of width 1 km/s , we reach a sensitivity of 540 mJy per beam in 10 hours. The line width for a perfectly face-on disk could be small, but it only takes a small inclination angle to significantly broaden the lines (for example, it takes only 6 degrees for Keplerian velocity to broaden the line to 1 km/s at 10 AU around a solar mass star). 0.″03 will resolve 4.2 AU at 140 AU and matches our resolution in the figure. For the purpose of illustration, we use the $J = 2 \rightarrow 1$ lines from a disk of 30° inclination. The apparent edge of the disk in $^{13}$CO moves from beyond 70 AU to about 55 AU, and from beyond 70 AU to about 20 AU in C$^{18}$O emission, well within the condensation front of CO in both cases. The migration of the "fake" snowline is a combined effect of the drop of CO emission intensities from the outer disk and the detection limit of the observation.

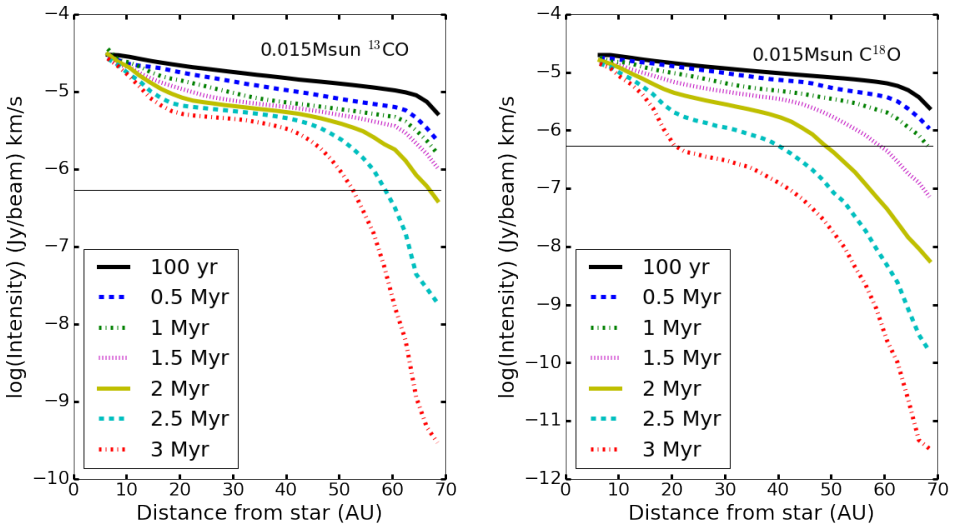


Figure 3.11: Time evolution of $^{13}$CO and C$^{18}$O $J = 2 \rightarrow 1$ lines for the 0.015 $M_\odot$ model at 30 degree inclination. All other parameters are the same as the above figure.

In disks where spatially resolved imaging is possible, a comparison between the C$^{18}$O and the CO or $^{13}$CO spatial distribution should reveal CO chemical depletion, and may even provide enough information to re-construct the CO distribution with the help of a chemical model. Finally, after 3 Myr of evolution, we see that two rings of $C_2H$ have formed in the surface layers of the disk: a narrow ring at $1 - 3$ AU

and a broader ring at $10 - 20$ AU. Bergin et al. (2016) found that $C_2H$ formation is possible only with a strong UV field and C/O$>$ 1, conditions which are replicated in our model disk surface layers due in part to the breakdown of CO molecules. We will explore the detectability of the $C_2H$ rings and the degree to which they may indicate CO depletion in future work.

## 3.7 Consequences for Observations

Our main result is that current observations and interpretations of CO isotopologues toward disks around solar-mass stars likely underestimate gas masses by substantial amounts. The surveys so far have emphasized shallow observations of many disks with modest spatial resolution. For example, Ansdell et al. (2016) surveyed 89 protoplanetary disks in Lupus with ALMA and found very low gas masses when assuming an ISM CO abundance. The analysis of those observations has led to the conclusion that almost no disks have masses that exceed the MMSN. This result would appear to conflict with the high fraction of stars with evidence for planetary systems.

Our predicted line intensities are weak, and deriving correct masses requires deeper integrations to obtain either line profiles of weak lines or very high spatial resolution. Until those observations are available, we can offer only rough estimates of how much more massive the disks may be. As an example, we ask the following question: if we apply a simple correction for $f_{CO}$, how many of the disks in Table 3 of Ansdell et al. (2016) might contain the mass of 0.01 $M_\odot$, the MMSN. If the mean age of stars in Lupus is $3 \pm 2$ Myr, we should use $f_{CO} = 0.136$, the value at 3 Myr for the 0.015 $M_\odot$disk, the closest to a MMSN. After applying this correction factor, 7 of 36 best guess masses exceed the MMSN, and 26 of 36 maximum masses exceed the MMSN, where best guess and maximum masses are defined by Ansdell et al. Within the uncertainties, a significant fraction of the disks in Lupus could contain enough mass to make a planetary system like ours. Recent analysis of similar observations toward disks in Cha I indicate a deficit of gas mass similar to, or worse than, that seen in the Lupus disks (Feng et al. 2017). For an age of 2 Myr and the 0.015 $M_\odot$ disk, the value of $f_{CO}$ is 0.18, which could increase the masses by a factor of about 5, leaving almost all disks in Cha I still short of the MMSN. Almost all these stars are lower in mass than our model star; models tuned to these stellar parameters would be needed

to draw further conclusions.

CO chemical depletion also affects estimates of gas/dust mass ratios. Assuming an ISM-like $CO/H_2$ abundance ratio, Ansdell et al. (2016) found a wide range of gas/dust ratios, with a median ratio of $\sim 15$, which is much smaller than the canonical value of 100 observed in the ISM. Miotello et al. (2017) have shown that this problem persists when their models with radiative transfer and isotope-selective photodissociation are used.

We argue that the low gas-to-dust ratios measured in Ansdell et al. (2016) are likely a result of a low $CO/H_2$ ratio due to CO chemical depletion. In our 0.015 $M_\odot$disk model, the closest to a MMSN, only 13.6% of carbon is contained in CO gas by 3 Myr. If the mean age of stars in Lupus is $3 \pm 2$ Myr, and we apply the simple correction for CO fraction ($f_{CO}$= 0.136) to the Lupus data with both $^{13}$CO and C$^{18}$O detections, we obtain gas-to-dust ratios of 53 to 1700, with a median gas-to-dust ratio of 108. The gas-to-dust ratios correcting for the fraction of C in CO in our models are plotted in Fig. 3.12.

The high values of the gas-to-dust ratios in the $f_{CO}$ corrected gas-to-dust ratios could be a combined result from grain growth, weak-ionizing environments, and young disk ages. Gas/dust mass ratios are not necessarily the same as gas/ *solid* mass ratios: the apparent dust mass is typically calculated from sub-mm dust emission, which is mostly sensitive to dust grains around sub-mm size or smaller. Once dust grains grow into cm-size pebbles, the reduction of observable dust mass could drive the gas/dust mass ratio to *larger* than the canonical molecular cloud value of 100. If only 10% of the solid mass is in the form of dust observable in 890$\mu$m, as we assume in our models, one would have to correct for the "dust fraction" ($f_{\rm dust}$) when measuring the gas-to-dust ratios. We apply the correction for dust fraction on the $f_{CO}$ corrected data, and plot the gas-to-dust ratios as blue squares in Fig. 3.12. Most the disks with high gas-to-dust ratios from the $f_{CO}$ corrections can be come consistent with the ISM value of 100 if additional corrections for grain growth are included.

Instead of assuming that dust evolution or disk clearing drives the variation in observed Lupus gas/dust ratios, we point to the large age spread of pre-main-sequence stars in Lupus. Ansdell et al. quote 1-3 Myr, while Mortier et al. (2011) find either 0.1 to $>$ 15 Myr or 0.3 to $>$ 15 Myr depending on the model isochrones (though the $>$ 10 Myr objects were not detected by Ansdell et al. and are therefore not represented in Figure 3.12). The large spread of gas/dust ratios calculated by Ansdell et al. is

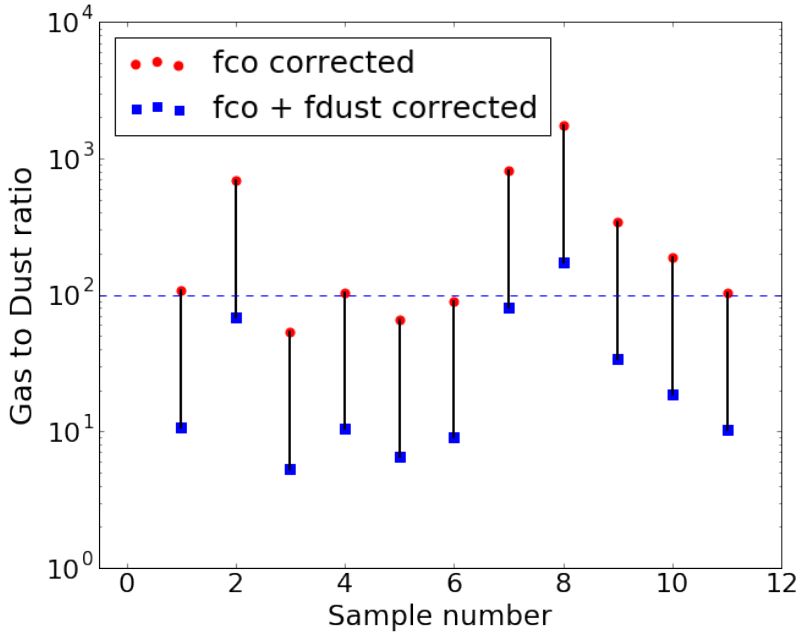


Figure 3.12: Corrected gas-to-dust ratios of the 11 stars in Ansdell et al. (2016) with both $^{13}$CO and C$^{18}$O detections. Red dots are values corrected for the CO fraction of 0.138, and blue squares are values corrected for both the CO fraction and the fraction of solids in dust (10%). The stars are in the order as presented in Ansdell et al. (2016) (shown as the sample number in Fig. 3.12) and the ordering has no particular meaning. The blue dashed line shows the ISM value of 100. The ISM value falls into the possible range of gas to dust ratio for 7 out of 11 stars.

likely the result of the variation of CO/$H_2$ abundance ratio with protostellar age. Given the uncertainties in both gas and solid mass, the data so far do not rule out ISM gas/dust ratios.

There are a few caveats to bear in mind regarding these simple mass correction factors. First, real disks evolve at different rates: a disk with a high incident cosmic-ray flux loses CO more quickly than a disk shielded by a "T-Tauriosphere" that deflects cosmic rays (Cleeves et al., 2013a, 2015). Even if star ages could be measured perfectly, the ages alone do not give enough information about the chemical evolutionary stage of the disk to compute a CO/$H_2$ ratio. In other words, our line profile diagnostics are measuring a "chemical age." Comparison of $^{13}$CO and C$^{18}$O line profiles gives an empirical diagnostic of the level of CO chemical depletion .

Second, chemical depletion of CO operates on a million-year timescale. If episodic

accretion of the type observed in FU Orionis outbursts happens during the T-Tauri phase at intervals smaller than $\sim$ 1Myr (e.g., Dunham et al., 2010; Kim et al., 2012; Martin et al., 2012; Green et al., 2013), desorption of $CO_2$ ice followed by $CO_2$ dissociation from cosmic ray-induced photons could raise the CO gas abundance throughout the disk, not just in the inner 20 AU as in our current model disk. Cieza et al. (2016b) have already proposed chemical alteration in the disk surrounding V883 Ori, which is now mid-outburst. We have not modeled FU Orionis outbursts—our model T-Tauri star evolves smoothly on the Hayashi track.

Other processes may further deplete CO in the outer regions of disks. For example, Xu et al. (2017) describe a process of "runaway freeze-out", which considers vertical transport at fixed radii. They find that higher layers, too warm for freeze-out, can become depleted by transport to the colder, lower layers. Kama et al. (2016b) suggest the same mechanism to explain the low atomic C and O abundances in the TW Hya disk. Applied to CO, the vertical transport/freezeout effect would primarily act at larger radii than we consider and affect primarily the emission from the more common, hence more optically thick, isotopes. Applied to the complex organics that sequester the carbon in our models, runaway freezeout could remove even more carbon from the gas phase, allowing for even higher $H_2$ masses to be consistent with observed gas-phase carbon abundances.

Our model's growing CO abundance in the inner disk and CO chemical depletion in the outer disk would be observationally almost identical to a disk with CO frozen onto grain surfaces in the outer disk, followed by inward radial drift of the grains and desorption of CO in the warm inner disk. The radial-transport effect, first applied to water ice, has been suggested on theoretical (Ciesla & Cuzzi, 2006; Du et al., 2015) and observational (Hogerheijde et al., 2011; Kama et al., 2016a) grounds, diagnosed from the presence of rings of small hydrocarbon chains (Bergin et al., 2016) and ammonia gas (Salinas et al., 2016) in the outer disk of TW Hya, and inferred in cases where C/O$>$ 1 (Bergin et al., 2016). Robust temperature measurements in the outer disk would be required to distinguish between chemical CO chemical depletion and CO freezeout followed by grain inspiral.

## 3.8 Conclusions

Our key findings and suggestions for observing strategies are summarized below.

1. CO abundance varies both with distance from the star and as a function of time as CO is dissociated and the carbon gets sequestered in organic molecules that freeze onto grain surfaces (chemical depletion) on a million year time scale (§3.2). CO chemical depletion will cause very large underestimates in gas mass and gas-to-dust ratios when CO observations are used. One would need to correct for the chemical depletion of CO in order to correctly estimate the disk gas mass. The CO abundance correction factor ranges from 3 to 8 for the models we have run (§3.4).

2. Even though CO is destroyed by ionized helium throughout most of the disk, it has a higher-than-interstellar abundance in the inner 20 AU of the disk, where the temperature is relatively high. Adopting a constant $T = 20$ K for the CO reservoir will underestimate gas masses by a further factor of about 2 (§3.4).

3. The high CO abundance in the inner disk also results in high optical depth even for the mostly optically thin isotopologue we investigated ($C^{17}O$), and one could underestimate the disk gas mass due to the optical depth effect even after correcting for the CO chemical depletion in the outer disk and using the correct CO-averaged temperature (§3.4).

4. The CO-abundance time evolution also introduces a disk age-mass degeneracy—a massive, old disk may look similar to a young, less massive one in CO rare isotopologue emission (§3.5).

5. One can diagnose CO chemical depletion by comparing the line intensity ratios (§3.6.1) or emission line profiles of multiple isotopologues (§3.6.2). If the disk is spatially resolved, one can also use spatial distribution of CO beyond 20 AU to probe the chemical depletion of CO. (§3.6.3).

6. Very different CO optical depths in different parts of the disk produce a complicated rotation diagram that does not probe the disk temperature well. One would underestimate the average temperature of CO molecules by deriving it from the lowest two J values (§3.11.1).

7. Higher-$J$ lines underestimate the disk mass by more than do lower-$J$ lines. The higher-$J$ lines miss low temperature gas. We suggest using low excitation lines (e.g., $J = 1 \rightarrow 0$) to estimate the disk mass to minimize the temperature and optical depth effects. (§3.11.2).

8. The strategy that comes closest to recovering the correct mass for our models is to use the formulae from Miotello et al. (2016) *and* to divide by the $f_{CO}$ from our models (§3.4).

9. If we correct the "best-guess" gas masses in Ansdell et al. (2016) by the smallest value of $f_{CO}$ (the value at 3 Myr for the 0.015 $M_\odot$ disk), 7 of the disks could have masses of the MMSN; if we apply our $f_{CO}$ correction to the maximum masses, 26 of 36 could reach the MMSN (§3.7). The age of Lupus is $3 \pm 2$ Myr (Alcalá et al., 2014), so this correction is reasonable. A recent survey of disks in Cha I suggest almost no disks with MMSN masses. While still problematic for planet formation models, correcting for CO chemical depletion suggests better numbers than finding that no disks contain the MMSN.

10. Given reasonable uncertainties in both gas and solid masses, many observed disks can have gas/dust ratios consistent with the ISM value of 100 (§3.7).

Work by MY, KW, SDR and NJT was supported by NASA grant NNX10AH28G and further work by MY and SDR was supported by NSF grant 1055910. This work was performed in part at the Jet Propulsion Laboratory, California Institute of Technology. NJT was supported by grant 13-OSS13-0114 from the NASA Origins of Solar Systems program. MY was supported by a Continuing Fellowship from the University of Texas at Austin. We acknowledge helpful input from L. Cleeves, E. Bergin, E. F. van Dishoeck, K. Öberg, J. Huang, M. Ansdell, and A. Kraus. We are grateful for Feng Long et al. sharing their paper in advance of publication, and Huang et al. sharing processed ALMA data for our model comparison.

## 3.9 Appendix: Sensitivity to model parameters

The effect of our assumption of LTE in the CO level populations and the fixed vertical grid are explored in the next two sub-sections.

### 3.9.1 LTE vs. NLTE

LIME is capable of computing energy level populations either in local thermodynamic equilibrium (LTE) or in the more complex non-LTE case, where the kinetic temperature and excitation temperature are different. In Paper 1, the lowest density found in the modeled region within 70 AU of the star is about $10^9$ hydrogen molecules per cubic centimeter. Even in the most diffuse regions of our model disk, the density should be high enough for collisions to dominate CO excitation so that LTE is a good approximation for the energy level population.

We demonstrate that the LTE approximation is appropriate for our model disk by comparing the results of LTE and non-LTE models for different CO isotopologues at multiple epochs. For each emission line of each isotopologue, the line profiles from the two models are indistinguishable. In figure 3.13 we show the worst case example of $C^{17}O$ J=6 − 5 emission at the beginning of the disk evolution. The high excitation energy of the J=6 − 5 transition means the LTE approximation requires a high collision rate and is hardest to satisfy, yet the differences between the LTE and non-LTE line profiles are still negligible.

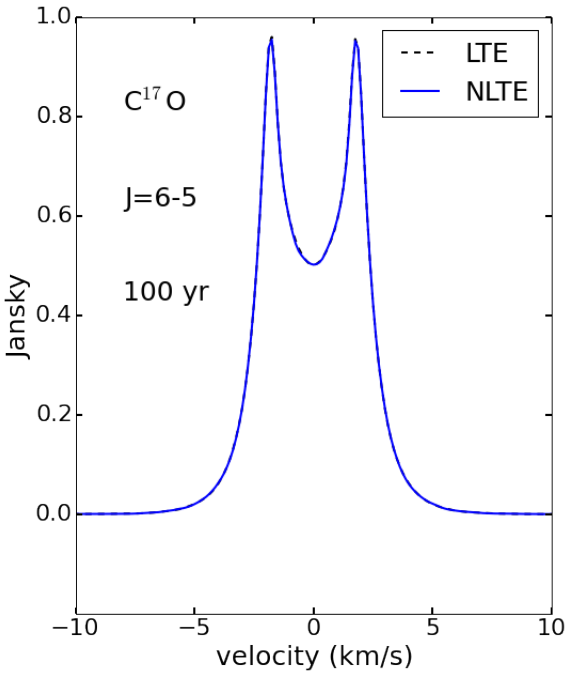


Figure 3.13: $C^{17}O$ J=2 − 1 rotational emission at the beginning of the evolution.

### 3.9.2 Definition of the disk surface

Another parameter that can influence the computed line profiles is the placement of the disk surface. In the disk models of Landry et al. (2013), on which the chemical models in Paper 1 are based, the top surface of the computational grid is placed at the layer where the Rosseland mean optical depth to the disk's own radiation, integrated downward from infinity, is 0.2. The $\tau = 0.2$ surface is located between one and two pressure scale heights above the disk midplane, depending on the distance from the star and time. Since most of the low-J CO emission comes from the disk interior where the bulk of the disk mass is located, the height of the grid surface should have minimal effect on the line profiles. For higher values of J, more of the emission would come from the warm surface and modeling line profiles accurately would require the computational grid to extend well into the tenuous disk atomsphere. Here we assess the effects of grid surface placement on our model emission line intensities and profiles.

The chemical model in Paper 1 uses a static grid that does not evolve with time. Grid cells are spaced logarithmically in radius $r$ and linearly in aspect ratio $z/r$. At the beginning of evolution, which roughly corresponds to the start of the T-Tauri phase, the disk has a high scale height due to heating from the luminous protostar. The scale height decreases throughout the 3Myr evolution due to both protostellar dimming and viscous dissipation. As the disk flattens, grid layers with high $z/r$ begin to empty out. To test the effect of surface placement on the radiative transfer calculation, we construct a new disk model by artificially removing the top three *filled* (not empty) $z/R$ layers from each time snapshot of our fiducial model from Paper 1. At six different epochs, we compute line profiles for the $1 \rightarrow 0$, $2 \rightarrow 1$, $3 \rightarrow 2$, $4 \rightarrow 3$, $5 \rightarrow 4$, and $6 \rightarrow 5$ transitions for all CO isotopologues using both the new "remove-top" model and the fiducial model. Removing emitting layers affects the peak intensities of the optically thin $C^{17}O$ emission lines more than any other isotopologue. To verify that our radiative transfer models capture essentially all of the disk emission, we demonstrate how the grid surface placement affects $C^{17}O$.

At the beginning of disk evolution, the top three grid layers contain very little mass and have little effect on the emission line intensity or profile (Figure 3.14, left panel). As the the disk cools and the top grid layers empty out, the mass contained in the filled grid layers increases. Line profiles from the fiducial and remove-top models differ the most after 3 Myr of evolution (Figure 3.14, right panel). Yet even at 3 Myr,

the difference in the $J = 3 \rightarrow 2$ peak intensity between the remove-top and the fiducial model would be difficult to distinguish in observations, and the normalized line profiles are almost identical.

The differences in peak intensities between the fiducial and remove-top models become significant for higher-J emission due to the higher energy needed to populate the upper state. For example, the peak intensity for $J = 6 \rightarrow 5$ differs by roughly 33% between the fiducial and remove-top models at 3 Myr of evolution. However, lower J lines ($J = 1 \rightarrow 0$ to $3 \rightarrow 2$) are more commonly used for disk studies. In this paper, we focus our line profile discussion on $J = 3 \rightarrow 2$ and $J = 2 \rightarrow 1$ transitions, which are the most observationally relevant transitions. For our purposes, we have adequately modeled the CO rare isotopologue emission, even though our models do not extend vertically to a large number of scale heights.

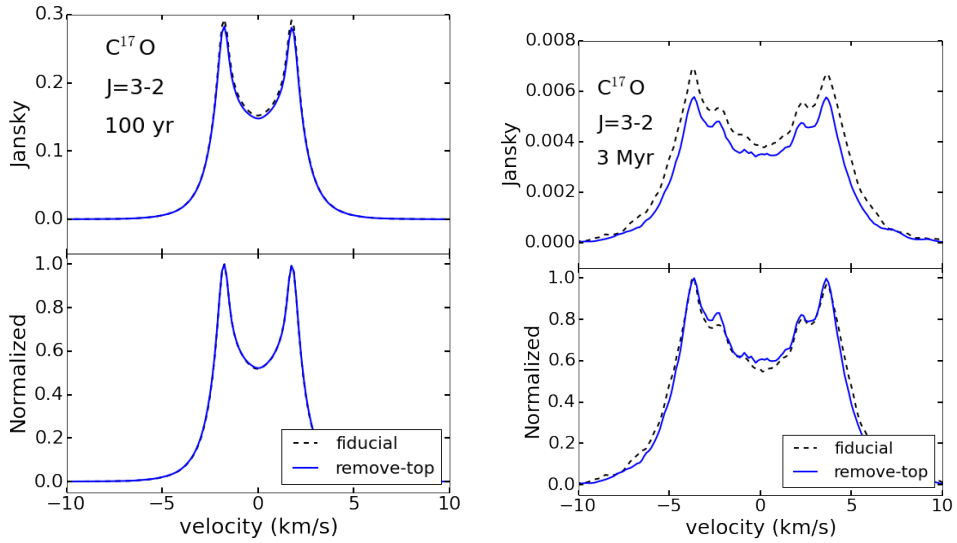


Figure 3.14: A comparison of J=3 − 2 emission from $C^{17}O$ between the fiducial models and models with the top-3 existing layers artificially removed. Left panels: the beginning of the evolution; right panels: the end of the evolution. The upper panels show the simulated emission lines and the lower panels show the line profiles normalized by the total line intensities. Removing the top-3 layers of the disk surface does not change the spectral line profiles at the beginning of the evolution. However, the mass contained in the surface layers increases as the disk surface moves closer to the midplane over time, and line intensities of the surface-removed model are slightly lower across all frequencies/velocities at the end of the evolution. The effects of removing the top 3 layers on the line profile remains negligible for low-J emission.

## 3.10 Appendix: Measuring disk mass from the integrated intensities of CO isotopologues

For optically thin emission lines, the total number of molecules per degenerate sublevel in the upper state can be written simply as

$$\frac{\mathcal{N}_J}{g_J} = \frac{L_J}{g_J A_J h\nu} \tag{3.3}$$

where $L_J$ is the line luminosity, $g_J$ is the degeneracy, $A_J$ is the Einstein A value for the transition from upper state with quantum number $J$, $h$ is Planck's constant, and $\nu$ is the frequency of the transition. $L_J$ is related to the integrated line flux $F_l$ as

$$L_J = F_l(\mathrm{c}gs) \times 4\pi D_{cm}^2 = 1.1964 \times 10^{20} \times F_l(\mathrm{J}y - km\ s^{-1})\ (\nu/c) D_{\mathrm{pc}}^2, \tag{3.4}$$

where $D_{cm}$ and $D_{\mathrm{pc}}$ are the star's distance in cm and pc, respectively, and $c$ is the speed of light. For the last part of Eq. 3.4 and Eq. 3.6, $\mathrm{F}_l$ is in the unit of $\mathrm{J}y - km\ s^{-1}$, $\mathrm{D}_{\mathrm{pc}}$ is in the unit of pc, and all the other values are in cgs units. The Einstein A value for rotational transitions from level $J$ to level $J-1$ is given by

$$A_J = \frac{64\pi^4}{3h} \times (\nu/c)^3 \times |\mu(J, J-1)|^2 = 3.13613 \times 10^{-7} \times (\nu/c)^3 \frac{J}{(2J+1)} {\mu_{\mathrm{D}}}^2 \tag{3.5}$$

where $|\mu(J, J-1)|$ is the electric dipole matrix element and $\mu_{\mathrm{D}}$ is the dipole moment measured in Debye ($10^{-18}$ esu-cm). Combining these, we can write

$$\frac{\mathcal{N}_J}{g_J} = 6.468 \times 10^{45} \frac{F_l(\mathrm{J}y - km\ s^{-1}) {D_{\mathrm{pc}}}^2}{{B_{\mathrm{GHz}}}^3 J^4 {\mu_{\mathrm{D}}}^2} \tag{3.6}$$

where $B_{\mathrm{GHz}}$ is the rotation constant in GHz. The values of $B_{\mathrm{GHz}}$ vary slightly with the isotopologue and are easily obtained from on-line sources, but for reference, $B_{\mathrm{GHz}} \approx 55$ to 58 GHz for the isotopes discussed here.

## 3.11 Appendix: Does a single temperature characterize the CO emission?

### 3.11.1 Temperature Estimates from Rotation Diagrams

A temperature estimate is required in order to evaluate the partition function that will translate observed intensities into gas column densities. While the disk temperature

can reach $\sim 1400$ K at the dust sublimation front (Muzerolle et al., 2003), Andrews & Williams (2005) and Andrews et al. (2013) suggest that most submillimeter emission comes from dust at $\sim 20 - 25$ K and a fixed temperature of 20 K for the gas is often used in the simplest methods to measure mass. Here we will use plots of level populations versus energy of the level above ground—called rotation diagrams for rotational transitions—to test whether CO in our model disk is well characterized by a single temperature. We calculate the rotation diagrams for the $0.015\,M_\odot$ disk and the $0.03\,M_\odot$ disk using the equations in Appendix 3.10, following the method of Green et al. (2013). Note that the emission must be optically thin (which is often assumed for CO isotopologues) for luminosity to be directly proportional to the upper state population.

Figure 3.15 shows the $^{13}$CO rotation diagram of our $0.015\,M_\odot$ model disk (left, circles) and our $0.03\,M_\odot$ model disk (right), both after 2 Myr of evolution. A gas reservoir with a single temperature would yield a straight line in $\ln(N_J/g_J)$ as a function of $E_{\rm up}$. Unfortunately, Figure 3.15 shows that no single temperature characterizes the CO level populations, consistent with *Herschel* observations of Herbig Ae/Be and T-Tauri disks by Meeus et al. (2013), Fedele et al. (2013), van der Wiel et al. (2014) and Fedele et al. (2016). Even when we construct an artificial disk with the same density and abundance structure as our 2 Myr models, but with a constant temperature enforced at all points (Figure 3.15, squares and triangles), the rotation diagram still appears to come from a disk with a range of temperatures because of the varying optical depth of different transitions. If we derive a temperature from the lowest two J values, the temperature is quite low—about 10 K. CO rotation diagrams, even for rare isotopologues, are not reliable ways to measure protostellar disk temperatures.

### 3.11.2 Inferred Mass Depends on the Transition Used

Because the temperature and optical depth are different in various parts of the disk, the mass estimation also depends on which isotopologue and which emission line is used. We show the mass estimated by different transitions and isotopologues at 100 yr, 2 Myr, and 3 Myr of the disk evolution in Figure 3.16. All models assume optically thin emission for simplicity. The estimated mass decreases as we use higher-J lines with higher excitation energy for the mass estimation. This is partially contributed

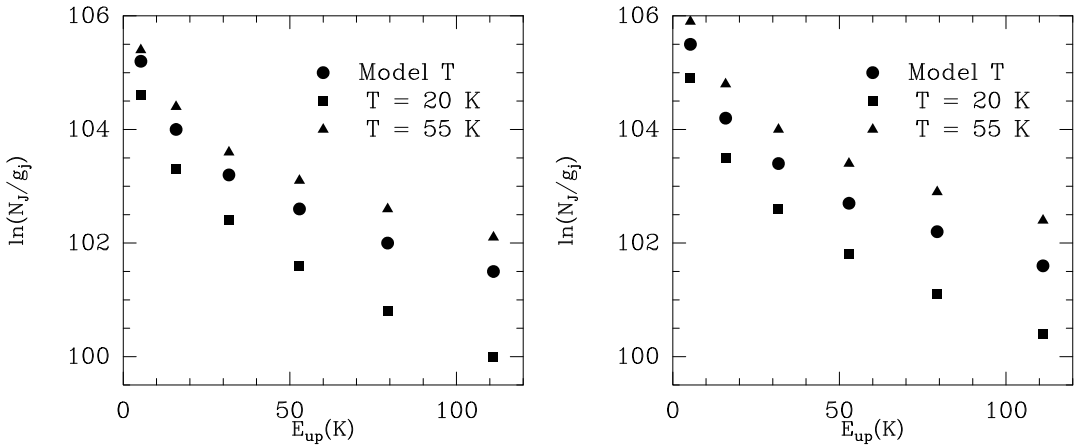


Figure 3.15: Rotation diagrams for $^{13}$CO for the disks with mass of $0.015\,M_{\odot}$ (left) and $0.03\,M_{\odot}$ (right) at 2 Myr. The circles are the values of the number of molecules per sublevel in the full model. The squares show values for the same model except that the gas temperature has been fixed at 20 K and the triangles show a model with $T = 55$ K.

by the large optical depth in the inner hot regions of the disk, partially because we are missing the low temperature CO that does not emit much at higher-J. Our models suggest that it is best to use lower $J$ transitions to measure disk mass.

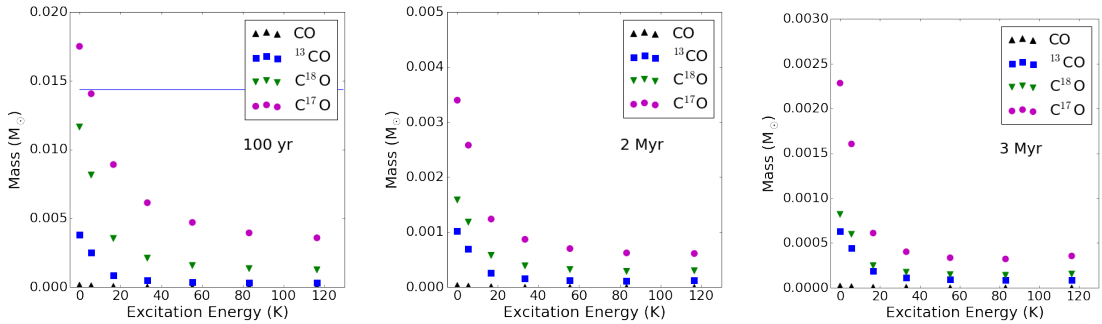


Figure 3.16: The mass estimated from various transitions and different isotopologues. Excitation energies are for the upper excitation state of each transition. The populations at the zero excitation energy are extrapolated from the higher energy populations with a three degree polynomial function. The actual disk mass is marked by the blue line in the 100 yr diagram (on the left), and is above the chart in plots for the 2 Myr and 3 Myr disks because the mass is hugely underestimated with the shown method. The actual disk masses in the input models at those three epochs are $0.0144\,M_{\odot}$, $0.0114\,M_{\odot}$ and $0.0107\,M_{\odot}$.

# Chapter Four: Can We Measure disk turbulence with peak-to-trough ratios of CO Lines?

Turbulence is the leading candidate for angular momentum transport in protoplanetary disks and therefore influences disk lifetimes and planet formation timescales. However, the turbulent properties of protoplanetary disks are poorly constrained observationally. Simon et al. (2015a) suggested that the ratio of the peak line flux to the flux at line center of the CO J=3-2 transition is a robust diagnostic of turbulence, while Flaherty et al. (2015a) found turbulent speeds in HD 163296 smaller than what fully-developed MRI would produce based on the Simon et al. (2015a) simulation results. Yet Simon et al. (2015a) and Flaherty et al. (2015a) assumed a constant $CO/H_2$ ratio of $10^{-4}$ in locations where CO is not frozen-out or photo-dissociated. Yu et al. (2016) found that the CO abundance varies both with distance from the star and as a function of time because CO molecules are gradually dissociated, with the liberated carbon forming complex organic molecules that freeze out on grain surfaces. This chemical depletion of CO affects the peak-to-trough ratios of CO and therefore complicates turbulence measurements in protoplanetary disks. We simulate the emission lines of CO based on chemical evolution models presented in Yu et al. (2016), and find that the peak-to-trough ratio changes as a function of time as CO is destroyed. Specifically, a CO-depleted disk with low turbulent velocity mimics the peak-to-trough ratios of a non-CO-depleted disk but with higher turbulent velocity. We suggest that disk observers and modelers take into account the possibility of CO depletion when using line peak-to-trough ratios to constrain the degree of turbulence in disks. Assuming a constant CO abundance can lead to underestimates of turbulent speeds in the disk by at least 0.2km/s.

## 4.1 Introduction

An angular momentum transfer mechanism is essential for the evolution of disks, the growth of stars, and the formation of planets. Throughout much of a T-Tauri disk, the combination of ionizing radiation and Keplerian shear should trigger the magne-

torotational instability (MRI; Balbus & Hawley, 1991, 1998; Hawley, 2001; Fromang & Nelson, 2006; Salmeron & Wardle, 2008). Yet some models that include non-ideal MHD effects predict MRI-driven accretion rates of order $\sim 10^{-9} M_\odot$ yr$^{-1}$ (Bai, 2011; Landry et al., 2013; Simon et al., 2013), which is about a factor of 10 below the typical T-Tauri disk accretion rate (Hartmann et al., 1998). An alternative to MRI turbulence comes from recent simulations showing that magnetic winds may drive angular momentum transfer in protoplanetary disks (Bai & Stone, 2013; Bai, 2013; Lesur et al., 2014; Gressel et al., 2015; Bai et al., 2016). In the magnetocentrifugal wind model, the disk remains laminar between 1 and 5 AU, with no significant turbulence. Since the gas velocity field controls both the sticking efficiency of colliding dust grains (e.g. Dominik & Tielens, 1997; Blum & Wurm, 2008; Birnstiel et al., 2010; Zsom et al., 2011) and the mass loss due to erosion or fragmentation in pebble collisions (e.g. Brauer et al., 2008; Birnstiel et al., 2009; Güttler et al., 2010; Kothe et al., 2010; Beitz et al., 2011), empirical measurements of turbulent speeds in disks would be extremely useful in developing theories of solid accretion, as well as understanding disk evolution.

Unfortunately, turbulent velocity profiles in disks are not well constrained.Flaherty et al. (2015a) observed CO emission lines in the HD 163296 disk with ALMA. The observations were interpreted as limiting turbulent speeds to levels far below what fully-developed MRI would produce, not enough to explain the star's high accretion rate of $5 \times 10^{-7} M_\odot$ yr$^{-1}$ (Mendigutía et al., 2013). Yet most turbulent speed measurements are model-dependent, and the HD 163296 disk may have complex CO chemistry that was not included in the Flaherty et al. (2015a) model. In a direct (non model-based) analysis of new ALMA CO, CN, and CS observations of TW Hydrae, plus archival data for TW Hydra and other sources, Teague et al. (2016) argue that almost all literature measurements of turbulent speeds—whether direct or model-based—should be interpreted as upper limits due to ALMA's 3% flux calibration accuracy. According to Teague et al. (2016), firm detections of turbulent motion require a ratio of turbulent speed to sound speed of $v_{\rm turb}/c_s 0.1$. Here we introduce another cautionary note by demonstrating how complexities in the spatial distribution of CO abundance can affect line shapes and complicate turbulent speed measurements.

Rotational emission lines from disks naturally form double-peaked profiles with a "trough at the systemic velocity. Based on models of MRI-active disks, Simon et al. (2015a) found the ratio of the peak line flux to the flux at the line center (peak-

to-trough ratio) to be a robust diagnostic of the MRI turbulence. However, Simon et al. (2015a) and Flaherty et al. (2015a) assumed a constant $CO/H_2$ ratio of $10^{-4}$ in locations where CO is not frozen-out or photo-dissociated. Our chemical evolution models (Yu et al. (2016), hereafter Paper 1) indicate that the CO abundance is a complex function of both radius and time, and CO abundance gradients may affect the peak-to-trough ratio of CO emission lines. This paper examines the effects of CO depletion on peak-to-trough ratios and turbulent speed measurements. We summarize the results of the thermal-chemical models in section 4.2, and describe the molecular line radiative transfer models in section 4.3. We discuss the implications of CO chemical depletion for line profiles and turbulent speed measurements in section 4.4. Finally, we examine the changes in peak-to-trough ratio as the disk evolves in section 4.5.

## 4.2 Thermal-chemical models

We adopt the thermo-chemical model from Paper 1 and Yu et al. (2017) (hereafter Paper 2) as the basis for this study. Paper 1 presented the chemical evolution of a $0.015\,M_\odot$ disk around a Solar-type star for 3 Myr, and Paper 2 introduced the model of a $0.03\,M_\odot$ disk, following the same modeling procedures as used for the $0.015\,M_\odot$ disk model. We summarize the key results of the two models in this section and refer readers to our previous papers for details.

Landry et al. (2013) presented the mass distributions and temperatures, considering only accretion heating, for both model disks, and we further calculated the stellar contribution to the disk heating with the dust radiative transfer code RADMC [1] in Paper 1 and Paper 2. We then ran the chemical reaction network locally at each independent (r, z) grid point for 3 Myr, following the viscous evolution of the disk and the evolution of the central star along the Hayashi track. No mixing is included in the model; we assume the chemical reaction timescale to be much shorter than the viscous timescale, which is true for freezeout, desorption, and grain-surface reactions, but which may fail for gas-phase reactions. Each disk gridpoint starts with gas and ice abundances resulting from a 1 Myr simulation of the chemical evolution of a

[1] http://www.ita.uni-heidelberg.de/ dullemond/software/radmc-3d/; developed by C. Dullemond

parent molecular cloud; as a result, a substantial fraction of the carbon is tied up in $CO_2$ and other ices at the start of disk evolution.

The chemical evolution models include C, H, O, N based on the UMIST database RATE06 (Woodall et al., 2007). Woods & Willacy (2009) extended the network to include C isotopes, and we included both C and O isotopes in Paper I. The chemical models follow the chemistry of 588 species, 414 gas-phase and 174 ices for 3Myr from the beginning of the T-Tauri phase. The reaction network contains gas-phase reactions, grain-surface reactions, freezeout, thermal desorption, and reactions triggered by UV, X-rays, and cosmic rays, such as isotope-selective photodissociation.

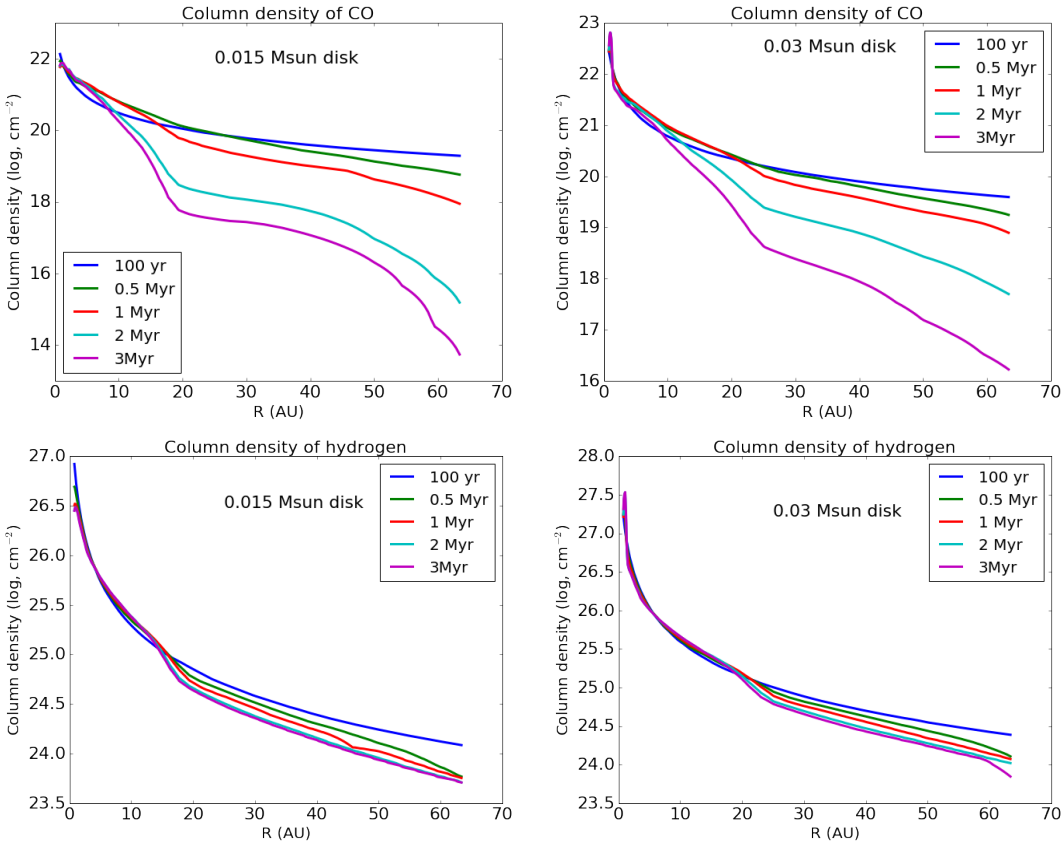


Figure 4.1: Column densities of CO (upper panels) and $H_2$ (lower panels) as a function of disk radius (R) in different stages of the disk evolution. Results for the $0.015\,M_\odot$ model are shown on the left and the results for the $0.03\,M_\odot$ model are on the right.

The luminosity of the central star ranges from $12\,L_\odot$ to about $0.8\,L_\odot$ over the 3Myr evolution. sDue to efficient heating from the central star, CO does not freeze

in our modeled region—the inner 70 AU of the disk—at any time in the 3 Myr of evolution. However, CO is depleted beyond 20 AU from the central star due to the formation of complex organic molecules, a process that we call chemical depletion. The CO chemical depletion is driven by ionization of helium from X-rays and cosmic rays and happens over a million-year time scale. As a result, the CO abundance changes both with location in the disk and with time. We show the column density as a function of disk radius for CO and $H_2$ at different stages of the disk evolution for both the $0.015\,M_\odot$ and the $0.03\,M_\odot$ disks in Fig. 4.1. The column density of CO drops significantly beyond 20 AU in both disks after roughly a million years of disk evolution, while the radial profile of the $H_2$ column density changes very little over time. The small change in $H_2$ column density is caused mostly by the pileup of material in the MRI dead zone (see paper 1 for details), while the change in CO column density is caused by the gradual chemical depletion of CO, with the liberated carbon atom forming complex species which then freeze, sequestering carbon in organic ices. The thermal-chemical model results are qualitatively similar for the disks of two masses (Papers 1 and 2). The chemical depletion timescale is slightly longer for the $0.03\,M_\odot$ disk because the higher column density decreases the ionization fraction—and thus the abundance of ionized helium—in the midplane. To complicate matters, while the outer disk is losing its CO, the abundance of CO simultaneously increases with time at small radii, as $CO_2$ ice is converted to CO gas.

The net result of our chemical models is that CO becomes severely depleted well inside the CO freeze-out radius in disks with masses above the minimum needed to form planetary systems. Similar effects have been seen in other chemical evolution calculations (Aikawa et al. 1999; Furuya & Aikawa 2014; Walsh et al. 2014; Bergin et al. 2014). A discussion of the similarities and differences between our models and other work can be found in paper 2.

## 4.3 Line radiative transfer models

After modeling disk thermal and chemical structures as functions of time, we build molecular line radiative transfer models to simulate observational properties of the disk. We use the publicly available code LIME (Brinch & Hogerheijde, 2010, LIne Modeling Engine), and adopt the energy levels and collision rates from the Leiden

Atomic and Molecular Database (LAMDA)[2]. As a first order approximation, we do not consider the hyperfine splitting in $C^{17}O$ emission.

We model emission from within 70AU of the central star, which corresponds to a 1″ beam diameter for an assumed distance of 140pc from the Sun. We consider line broadening due to Keplerian rotation, thermal velocity and micro-turbulence. Thermal velocities are calculated assuming a Maxwell-Boltzmann speed distribution based on the disk's temperature structure from Paper 1. We assume an isotropic Maxwell-Boltzmann speed distribution with RMS of 100m/s everywhere in the disk for the micro-turbulence in the fiducial models, and discuss effects of varying both the RMS turbulent speed and its radial and vertical profile in later sections. To compute the level populations, we set a minimum scale of 0.07AU to guarantee sub-pixel sampling of both Keplerian speeds and CO abundance gradients. We first generate the synthetic datacube of intensity as a function of $x$, $y$, and velocity for a disk around a $0.95\,M_{\odot}$ star at 30° inclination, similar to the disk surrounding AS 209. In velocity space, the spectra have 300 channels of 125m/s resolution. At any specific velocity, the synthetic image contains $600 \times 600$ pixels of $0.003'' \times 0.003''$ in size. Finally, we generate the synthetic spectra presented here by integrating each velocity component over a square with 1.2″ sides ($400 \times 400$ pixels), larger than the angular size of the disk. The pixels not covered by the disk contribute no flux and are included simply for ease of integration—here we assume that the sky background contains negligible flux compared with the disk at all wavelengths.

Our current models assume that the gas temperature is the same as the dust temperature. As we demonstrated in the Appendix of Paper 2, this is a valid assumption for $J = 3 \rightarrow 2$ and $J = 2 \rightarrow 1$. However, the difference between the gas and dust temperature would need to be considered in order to use our models to fit high-J spectral lines, which are dominated by emission from the disk surface. For the rest of the paper, we focus our line profile discussion on the $J = 3 \rightarrow 2$ and $J = 2 \rightarrow 1$ transitions, which are the most commonly observed. We assume LTE for energy level populations, an assumption that we have justified in the Appendix of Paper 2.

[2]http://home.strw.leidenuniv.nl/ moldata/

## 4.4 Effects of CO depletion and turbulent velocities on CO line profiles

We show the time evolution of the CO $J = 3 \rightarrow 2$ line from our fiducial disk on the left side of Figure 4.2. Simulated emission lines from LIME are plotted in the upper panel of each plot, and the profiles normalized to the peak intensities are shown in the lower panels. The total intensities decline with time dramatically, the line profiles become broader, and the relative contribution from the line center decreases over time. The line's broadening over time occurs because CO depletion happens primarily in the outer part of the disk where Keplerian velocities are small, so the fraction of radiation from the high-velocity line wings increases with time. Moreover, new CO forms from $CH_3$ and $CO_2$ at small radii, further increasing the contribution of the line wings. The bottom-left panel of Figure 4.2 shows that the peak-to-trough ratio of CO $J = 3 \rightarrow 2$ must increase as the fiducial disk evolves.

### 4.4.1 Effects of the chemical depletion of CO

To isolate the effect of chemical depletion of CO on emission line profiles from effects caused by the evolution of disk density and temperature, we introduce models with constant CO abundance throughout the disk—assuming all available carbon is in the form of CO gas. The abundance of CO normalized to the total proton number density is $7.21 \times 10^{-5}$. All the other properties of the constant CO models are the same as in the fiducial model. The time evolution of the CO $J = 3 \rightarrow 2$ line for the constant CO model are shown on the right of Figure 4.2 for comparison. The models with constant CO predict a much smaller decrease in integrated line intensity with time than do the fiducial models. As most easily seen in the normalized profiles (lower panels), the peak-to-trough ratio changes much more in the fiducial models, which account for chemical depletion, than in the constant CO models.

### 4.4.2 Effects of varying RMS turbulent speed and radial/vertical speed profile

Next, we want to isolate the effect of turbulent velocities on line profiles. All models shown in Figure 4.2 include a microturbulent velocity field with RMS of 0.1km/s. To

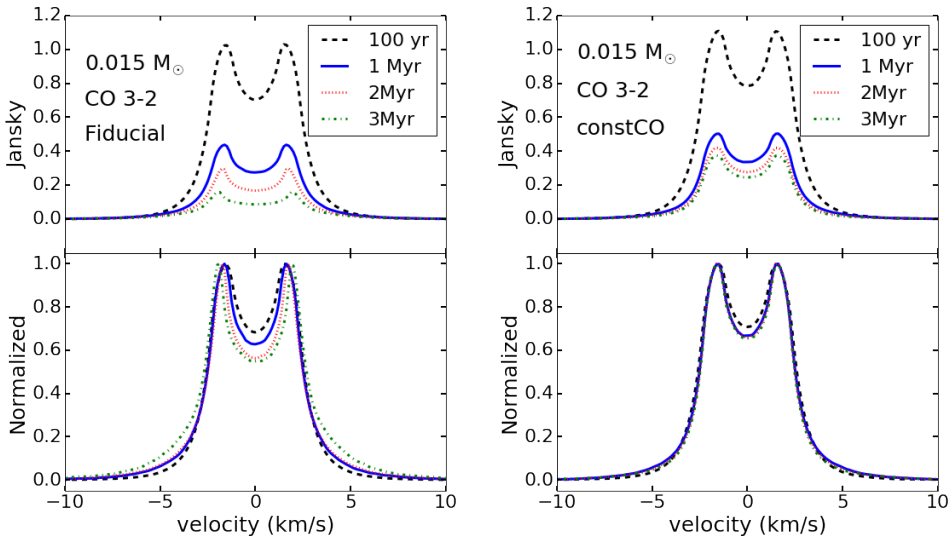


Figure 4.2: Time evolution of the CO $J = 3 \rightarrow 2$ line. Results from the fiducial model with $0.015\,M_{\odot}$ are on the left, and results from the constant CO model of the same mass are on the right. The top panels show the simulated lines from LIME, and the lower panels show the line profiles normalized to the peak intensity of each line. In both models, emission becomes weaker over time as the disk cools. The relative contribution from the line center also decreases over time in the fiducial model with CO chemical depletion, while normalized line profiles in the constant CO model remain the same for the last 2 Myr of the disk evolution.

distinguish the effects of CO depletion from the effects of RMS turbulent speed on CO line profiles and therefore the peak-to-trough ratios, we simulate CO $J = 3 \rightarrow 2$ emission for a 2 Myr disk with a range of RMS micro-turbulent velocities.

We show the line profiles from both the $0.015M_{\odot}$ and the $0.03M_{\odot}$ fiducial disk models at the 2 Myr time snapshot, with varying micro-turbulent velocities, in Fig 4.3. In both disks, the increase of micro-turbulent velocity leads to increased contributions from the line center, resulting in smaller peak-to-trough ratios. Similar effects were found by Simon et al. (2015a)—for a single time snapshot of the disk model, the peak-to-trough ratio decreases with increasing microturbulent velocity. Integrated emission increases with RMS turbulent speed due to the decrease of the opacity by spreading the absorbers in velocity space.

Besides the magnitude of the RMS turbulent speed, the radial and vertical profile of the turbulence speed can also make a difference to the line profile and the peak-to-trough ratio. Landry et al. provide the spatial distribution in $(r, z)$ of the RMS

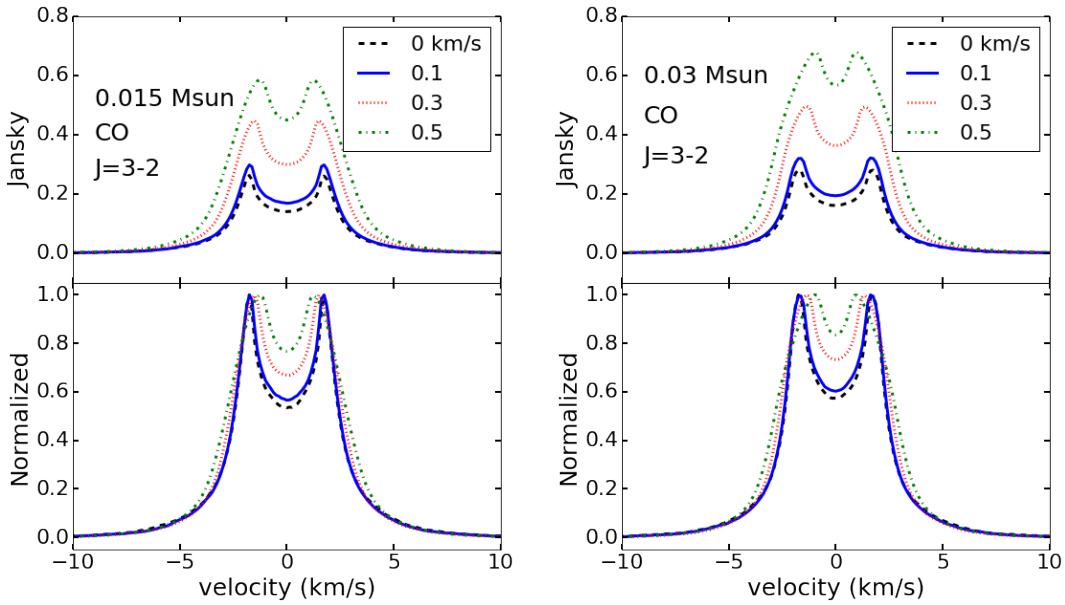


Figure 4.3: The line profiles of CO for a 2 Myr disk with various micro-turbulent velocities. The $0.015\,M_{\odot}$ model is on the left and the $0.03\,M_{\odot}$ model is on the right. In both disks, the increase of micro-turbulent velocity increases the relative contribution from the line center, resulting in a decreasing peak-to-trough ratio.

turbulent speed in each grid cell as a function of time in the form of $\alpha$, where the 1D turbulent velocity is $v_{tur} = \sqrt{3}\alpha \times C_s$, with $C_s$ as the local sound speed. We include the turbulent velocity $(r, z)$ profile for the $0.015 M_{\odot}$ disk at 2 Myr to see the effect of incorporating non-uniform turbulent velocities in Figure 4.4. The Landry et al. (2013) model predicts a nearly quiescent midplane dead zone from 2-20 AU, with low turbulent speeds on the disk surface that generate an accretion rate onto the star of $\sim 10^{-9}\,M_{\odot}$ yr$^{-1}$. The overall low turbulent speeds provide the slightly higher peak-to-trough ratio than seen in the model with 100m/s RMS turbulent speed throughout the disk.

## 4.5 Time evolution of the peak-to-trough ratio

Figure 4.2 shows that disks with the same mass distribution and ionization environment will have different CO emission line profiles if observed at different ages. We calculate peak-to-trough ratios as a function of time and plot those of the J=3 − 2 lines in Figure 4.5. In the fiducial model, the CO peak-to-trough ratio increases from

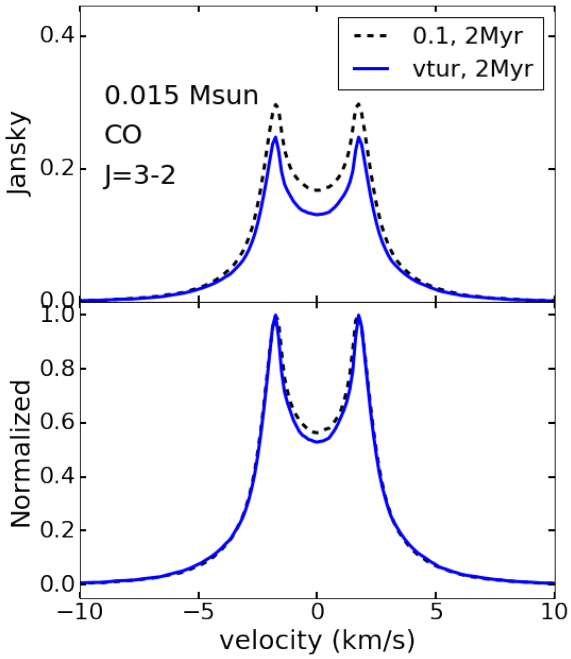


Figure 4.4: The line profiles of CO for a 2 Myr disk with the turbulent profile from the MRI model and a constant RMS speed of 0.1km/s.

about 1.45 to 1.85 as the disk evolves. The change over time is comparable to the increase of peak-to-trough ratio caused by the decrease of turbulent velocities by a factor of 2 to 3, as found in both Simon et al. (2015a) and Section 4.4.2. The growth of the high-velocity line wings induced by chemical evolution can masquerade as a decrease in RMS turbulent speed with time if peak-to-trough ratio is taken as an indicator of only thermal and turbulent speed.

### 4.5.1 Assuming a constant CO abundance leads to underestimates of turbulent speed

Would an observer misinterpret the high peak-to-trough ratios predicted in our models as signatures for low turbulent velocities? To answer this question, we calculate both constant CO models and fiducial models with chemical depletion, incorporating a range of turbulent velocities. We then consider how observers would interpret peak-to-trough ratios with no prior knowledge of disk chemical composition. The evolution tracks of the peak-to-trough ratio assuming no CO depletion with various

turbulent velocities are shown alongside those of the fiducial model in Fig. 4.5.

The peak-to-trough ratio increases slowly over time even without the effect of CO chemical depletion. During the first million years of evolution, this is due to significantly disk cooling as the star dims along the Hayashi track. Both the decrease of emitting area and the disk cooling contribute to the increase in peak-to-trough ratio later in the evolution. However, the peak-to-trough ratio increases much faster in our fiducial model with CO depletion. While the fiducial model mimics the peak-to-trough ratios of models with lower turbulent velocities in the first million years of evolution, it produces peak-to-trough ratios higher than what could be explained by the grid of constant CO and constant turbulent velocity models after 1 Myr. Observations that yield peak-to-trough ratios higher than those produced by a disk with constant CO abundance and zero microturbulence might indirectly indicate CO chemical depletion.

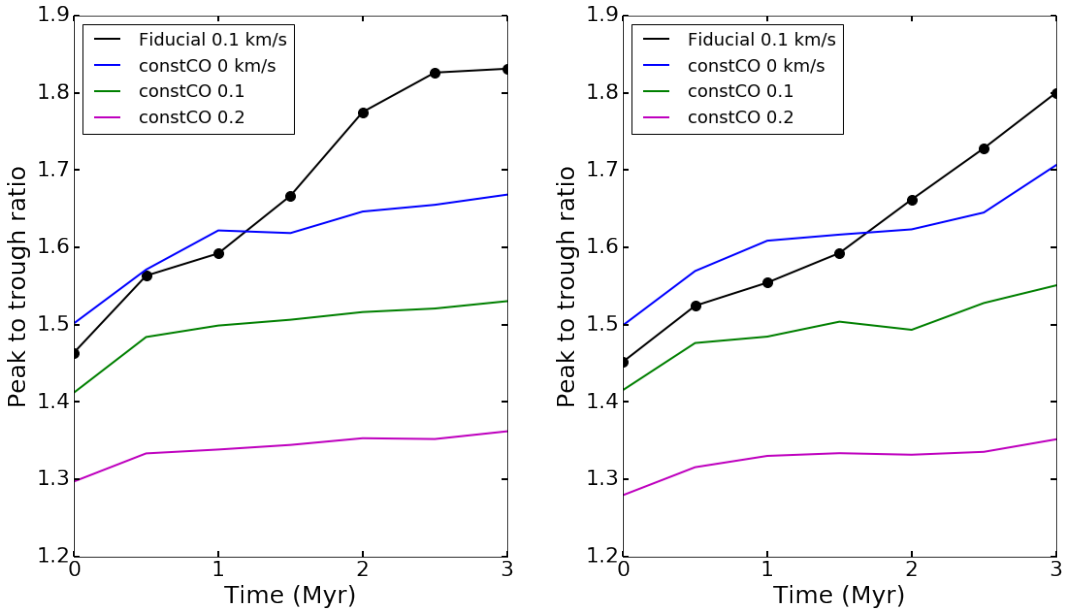


Figure 4.5: The time evolution of the peak-to-trough ratios of the CO $J = 3 \rightarrow 2$ line. The $0.015\,M_{\odot}$ disk is plotted on the left and the $0.03\,M_{\odot}$ model is on the right. The black lines are the fiducial model (with CO chemical depletion, and turbulent velocity of 0.1km/s). For comparison, we plot the peak-to-trough ratio predicted assuming a constant CO abundance with different turbulence velocities in blue, green and magenta.

We further illustrate the uncertainties in estimating the turbulent velocity using

peak-to-trough ratios by plotting the peak-to-trough ratios from different models against the turbulent velocities used to set up each model. The peak-to-trough ratios of the CO $J = 3 \rightarrow 2$ line from the fiducial model (with CO chemical depletion) and constant CO models with turbulent velocities of $0, 0.1$ and 0.2km/s are shown in Figure 4.6. The scatter of points within the same model is produced by time evolution of the disk. Models with the same turbulent velocity can produce a wide range of peak-to-trough ratios as evolution increases the peak-to-trough ratio. By assuming a constant $CO/H_2$ abundance ratio, one can easily conclude that there is no turbulence in a CO-depleted disk with an RMS turbulent velocity of 0.2km/s. For example, a 1 Myr old with constant CO abundance and no turbulence has the same peak-to-trough ratio as a 2 Myr disk with chemical CO depletion (fiducial model) and a turbulent velocity of 0.2km/s.

### 4.5.2 Effects of inclination

So far we have set a 30 degree inclination for our model disk, while Simon et al. (2015a) assumed a 44 degree inclination. The peak-to-trough ratios presented here are therefore smaller than values presented in Simon et al. (2015a). To directly compare our model results with the predictions of Simon et al. (2015a), we compute the peak-to-trough ratios of CO $J = 3 \rightarrow 2$ for the 0.015 $M_\odot$ disk at a 44 degree inclination, assuming a constant CO abundance and zero turbulent velocities. We choose to compare models with zero turbulent velocities and a constant CO abundance to minimize the differences between this experiment and the low turbulent velocity models in Simon et al. (2015a). The peak-to-trough ratios are plotted as the red lines in Fig. 4.7. Comparing the blue and red lines in the figure, we can see that changing the inclination from 30 to 44 degrees increases the peak-to-trough ratios by about 0.3. Translating the peak-to-trough ratio into meaningful information about the turbulent velocity requires detailed knowledge of the disk inclination.

## 4.6 Conclusion

We demonstrate how the thermal and chemical evolution of a protoplanetary disk complicates the measurement of the turbulent velocity—a fundamental disk property that controls the first stages of planet formation as grains assemble into pebbles. We

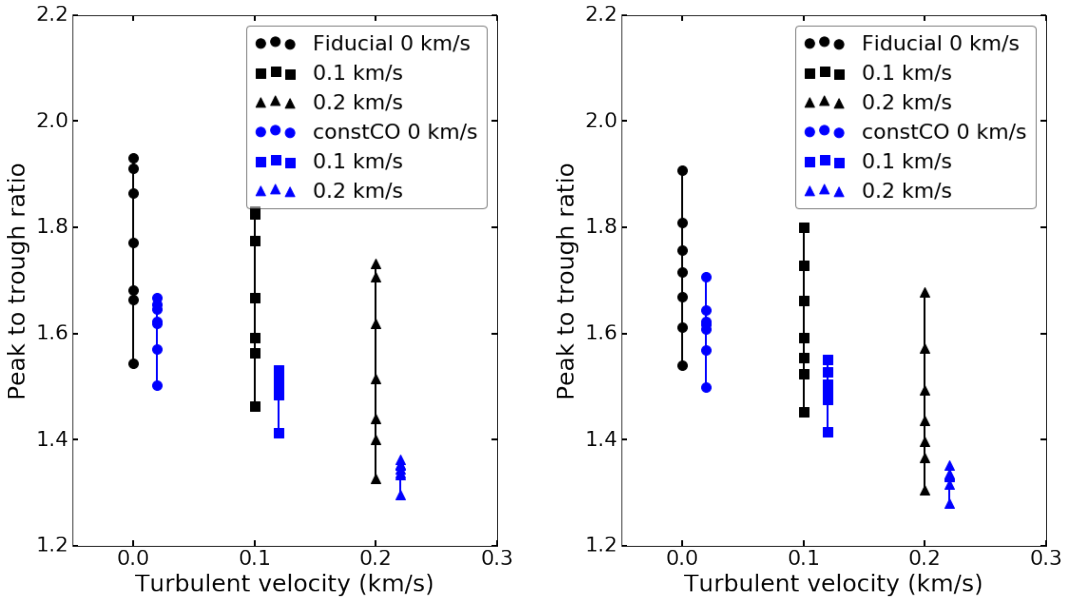


Figure 4.6: The peak-to-trough ratios of the CO $J = 3 \rightarrow 2$ line for the fiducial and constant CO models. The constant CO models are displaced slightly to the right in each case for clarity. The $0.015\,M_{\odot}$ disk is plotted on the left and the $0.03\,M_{\odot}$ model is on the right. We plot the peak-to-trough ratios from the fiducial model (with CO chemical depletion, and turbulent velocity of 0.1km/s) and constant CO models with turbulent velocities of $0, 0.1$ and 0.2km/s. The increase of the peak-to-trough ratio over time is produced by time evolution of the disk. Models with the same turbulent velocity can produce a wide range of peak-to-trough ratios as the peak-to-trough ratio increases with time. One can easily conclude zero turbulence from a disk with CO depletion and a true turbulent velocity of 0.1km/s if assuming a constant CO abundance. Similarly, among disks with constant CO abundance, an old disk with $v_{tur} = 0.1$km/s produces the same peak-to-trough ratio as a young disk with no turbulence.

show that the peak-to-trough ratio could vary by up to 25% due to the disk evolution over time, as the CO abundance distribution changes and the disk cools. One would underestimate the RMS turbulent speed by as much as 200m/s by assuming a constant $CO/H_2$ abundance ratio in a disk with chemical CO depletion. Even when chemical depletion is not operating, simple disk cooling as the star evolves can give the same observed peak-to-trough ratio to an old disk with $v_{tur} = 0.1$km/s and a young disk with no turbulence.

Quick observations of the abundant $^{12}C^{16}O$ molecule are, by themselves, inadequate diagnostics of disk turbulence: more detailed information about the disk tem-

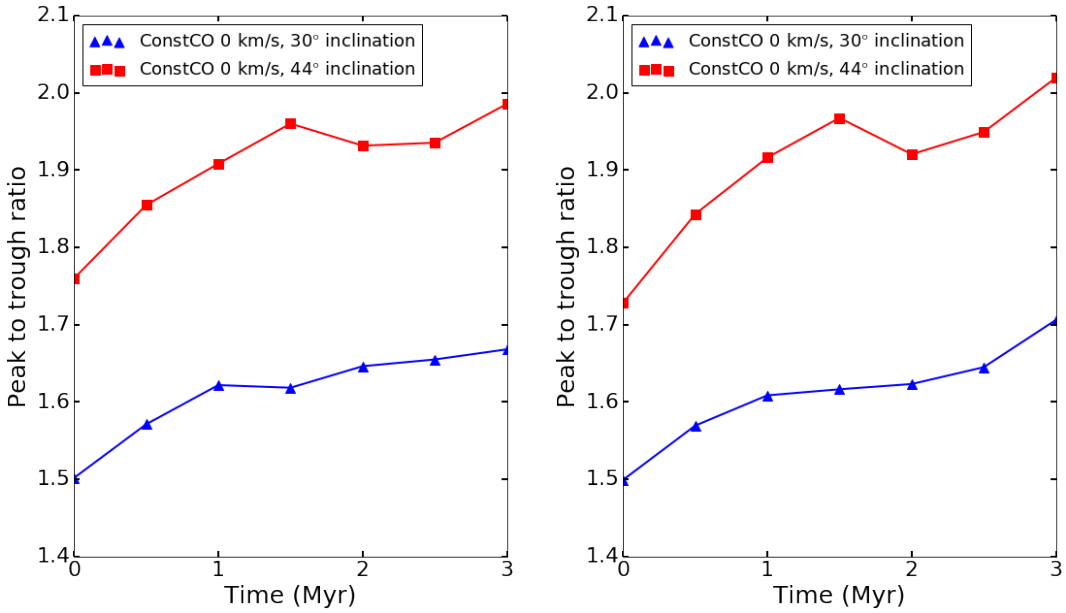


Figure 4.7: Comparison of the peak-to-trough ratios of the CO $J = 3 \rightarrow 2$ line with 30 and 44 degree inclinations. The $0.015\,M_{\odot}$ disk is plotted on the left and the $0.03\,M_{\odot}$ model is on the right. To avoid the complications of other factors, we compare the models with a constant CO abundance and zero turbulent velocities. By changing the inclination from 30 to 44 degrees, the peak-to-trough ratios increase about 0.3.

perature and CO abundance distribution is required. Deeper observations of multiple isotopologues can help constrain the CO abundance distribution (Paper 2). In disks where the normalized line profiles are substantially wider for the rare isotopologues $C^{17}O$ and $C^{18}O$ than for CO and $^{13}CO$, chemical depletion is well underway and the $CO/H_2$ abundance ratio is not constant. A clear measurement of the RMS turbulent speed from CO emission lines would require spatially resolved observations of multiple isotopologues and, ideally, multiple transitions in order to map the temperature and abundance of the CO gas as a function of $(r, z)$. Considering uncertainties in CO abundance distributions and disk temperature structures, disks may be more turbulent than currently estimated.

Work by MY, KW, SDR and NJT was supported by NASA grant NNX10AH28G and further work by MY and SDR was supported by NSF grant 1055910. This work was performed in part at the Jet Propulsion Laboratory, California Institute of Technology. NJT was supported by grant 13-OSS13-0114 from the NASA Origins of Solar Systems program. MY was supported by a Continuing Fellowship from the

University of Texas at Austin. We acknowledge helpful input from J. Simon, E. Bergin and J. Lacy.

RADMC (http://www.ita.uni-heidelberg.de/ dullemond/software/radmc-3d/), LIME (Brinch & Hogerheijde, 2010)

# Chapter Five: Conclusion

In this dissertation, we discussed a few aspects of protoplanetary disks and attempted to connect the observational tracers to theoretical predictions.

We first developed chemistry models that include a comprehensive reaction network and various C and O isotopes based on MRI-active disks. We followed thermal, dynamical and chemical evolutions of the disks over a typical protoplanetary disk lifetime of three million years. The models started with a molecular cloud model where a significant amount of C was in $CO_2$ ice. We found that CO is not the most abundant carbon-bearing molecule in protoplanetary disks; instead, a significant fraction of CO molecules react into complex organic molecules and freeze onto the grain surface. This leads to the depletion of CO over a few million years in regions where the temperature is not low enough for CO itself to freeze out.

We then evaluated observational consequences of chemically-evolving disks with molecular line radiative transfer models. Due to a combination of CO depletion and concentration of CO in the inner 20AU of the disk, one would underestimate disk masses with CO observations by more than an order of magnitude. Ionization is the determining factor of the CO depletion time scale, so one would need to constrain the "chemical age" of the disk in order to correct for the CO depletion effect. We recommended three strategies to reach factor of a few accuracy for CO-based disk mass measurements: (1) elect the low-J transitions; (2) observe multiple CO isotopologues and use either intensity ratios or normalized line profiles to diagnose CO chemical depletion; and (3) use spatially resolved observations to measure the CO abundance distribution. Our results help to explain recently observed low gas-to-dust ratios in protoplanetary disks (Ansdell et al., 2016; Long et al., 2017) and the decrease of CO column density at a few tens of AU from the central star (Schwarz et al., 2016). We provided solutions to adjust for the CO depletion effect in disk mass measurements to reach a factor of a few accuracy.

Finally, we discussed another fundamental disk property that is important for planet formation - the turbulent velocity. The degree of turbulence determines the dissipation timescale of the disk - therefore the time available for planet formation. The turbulent velocity also affects the coagulation and migration of dust grains,

which are important for the formation of rocky planet cores. Peak-to-trough ratios of CO rotational lines have been proposed as a robust probe of turbulent velocities. However, we showed that the peak-to-trough ratio could vary by 25% due to the uncertainties in the degree of CO depletion. One would underestimate the degree of turbulence if the chemical depletion of CO is not properly accounted for.

# Bibliography


Aikawa, Y., Umebayashi, T., Nakano, T., & Miyama, S. M. 1997, ApJ, 486, L51

—. 1999, ApJ, 519, 705

Alcalá, J. M., Natta, A., Manara, C. F., et al. 2014, A&A, 561, A2

Alexander, R., Pascucci, I., Andrews, S., Armitage, P., & Cieza, L. 2014, Protostars and Planets VI, 475

Alexander, R. D., Clarke, C. J., & Pringle, J. E. 2006, MNRAS, 369, 229

Ali-Dib, M., Mousis, O., Petit, J.-M., & Lunine, J. I. 2014a, ApJ, 785, 125

—. 2014b, ApJ, 793, 9

ALMA Partnership, Brogan, C. L., Pérez, L. M., et al. 2015, ApJ, 808, L3

Andrews, S. M., Rosenfeld, K. A., Kraus, A. L., & Wilner, D. J. 2013, ApJ, 771, 129

Andrews, S. M., & Williams, J. P. 2005, ApJ, 631, 1134

—. 2007, ApJ, 659, 705

Andrews, S. M., Wilner, D. J., Hughes, A. M., et al. 2012, ApJ, 744, 162

Ansdell, M., Williams, J. P., van der Marel, N., et al. 2016, ApJ, 828, 46

Audard, M., Ábrahám, P., Dunham, M. M., et al. 2014, Protostars and Planets VI, 387

Bai, X.-N. 2011, ApJ, 739, 50

—. 2013, ApJ, 772, 96

Bai, X.-N., & Goodman, J. 2009, ApJ, 701, 737

Bai, X.-N., & Stone, J. M. 2013, ApJ, 769, 76

Bai, X.-N., Ye, J., Goodman, J., & Yuan, F. 2016, ApJ, 818, 152

Balbus, S. A., & Hawley, J. F. 1991, ApJ, 376, 214

—. 1998, Reviews of Modern Physics, 70, 1

Banzatti, A., Testi, L., Isella, A., et al. 2011, A&A, 525, A12

Beitz, E., Güttler, C., Blum, J., et al. 2011, ApJ, 736, 34

Bergin, E. A., Cleeves, L. I., Crockett, N., & Blake, G. A. 2014, Faraday Discussions, 168, arXiv:1405.7394

Bergin, E. A., Du, F., Cleeves, L. I., et al. 2016, ApJ, 831, 101

Bergin, E. A., Cleeves, L. I., Gorti, U., et al. 2013, Nature, 493, 644

Birnstiel, T., & Andrews, S. M. 2014, ApJ, 780, 153

Birnstiel, T., Dullemond, C. P., & Brauer, F. 2009, A&A, 503, L5

—. 2010, A&A, 513, A79

Birnstiel, T., Ormel, C. W., & Dullemond, C. P. 2011, A&A, 525, A11

Blum, J., & Wurm, G. 2008, ARA&A, 46, 21

Boneberg, D. M., Panić, O., Haworth, T. J., Clarke, C. J., & Min, M. 2016, MNRAS, 461, 385

Brauer, F., Dullemond, C. P., & Henning, T. 2008, A&A, 480, 859

Brinch, C., & Hogerheijde, M. R. 2010, A&A, 523, A25

Bruderer, S., van Dishoeck, E. F., Doty, S. D., & Herczeg, G. J. 2012, A&A, 541, A91

Bryden, G., Beichman, C. A., Carpenter, J. M., et al. 2009, ApJ, 705, 1226

Chapillon, E., Guilloteau, S., Dutrey, A., & Piétu, V. 2008, A&A, 488, 565

Chiang, E. I., & Goldreich, P. 1997, ApJ, 490, 368

Ciesla, F. J., & Cuzzi, J. N. 2006, Icarus, 181, 178

Cieza, L. A., Casassus, S., Tobin, J., et al. 2016a, Nature, 535, 258

—. 2016b, Nature, 535, 258

Cleeves, L. I. 2016, ApJ, 816, L21

Cleeves, L. I., Adams, F. C., & Bergin, E. A. 2013a, ApJ, 772, 5

Cleeves, L. I., Adams, F. C., Bergin, E. A., & Visser, R. 2013b, ApJ, 777, 28

Cleeves, L. I., Bergin, E. A., Qi, C., Adams, F. C., & Öberg, K. I. 2015, ApJ, 799, 204

Cody, A. M., Hillenbrand, L. A., David, T. J., et al. 2017, ApJ, 836, 41

D'Angelo, G., Weidenschilling, S. J., Lissauer, J. J., & Bodenheimer, P. 2014, Icarus, 241, 298

D'Antona, F., & Mazzitelli, I. 1994, ApJS, 90, 467

Dartois, E., Dutrey, A., & Guilloteau, S. 2003, A&A, 399, 773

Dodson-Robinson, S. E., & Bodenheimer, P. 2010, Icarus, 207, 491

Dodson-Robinson, S. E., Willacy, K., Bodenheimer, P., Turner, N. J., & Beichman, C. A. 2009, Icarus, 200, 672

Dominik, C., & Tielens, A. G. G. M. 1997, ApJ, 480, 647

Drozdovskaya, M. N., Walsh, C., van Dishoeck, E. F., et al. 2016, MNRAS, 462, 977

Du, F., Bergin, E. A., & Hogerheijde, M. R. 2015, ApJ, 807, L32

Dullemond, C. P., & Dominik, C. 2004, A&A, 421, 1075

—. 2005, A&A, 434, 971

Dunham, M. M., Evans, II, N. J., Terebey, S., Dullemond, C. P., & Young, C. H. 2010, ApJ, 710, 470

Dunham, M. M., & Vorobyov, E. I. 2012, ApJ, 747, 52

Dutrey, A., Guilloteau, S., & Simon, M. 2003, A&A, 402, 1003

Favre, C., Cleeves, L. I., Bergin, E. A., Qi, C., & Blake, G. A. 2013, ApJ, 776, L38

Fedele, D., Bruderer, S., van Dishoeck, E. F., et al. 2013, ApJ, 776, L3

Fedele, D., van Dishoeck, E. F., Kama, M., Bruderer, S., & Hogerheijde, M. R. 2016, A&A, 591, A95

Flaherty, K. M., Hughes, A. M., Rosenfeld, K. A., et al. 2015a, ApJ, 813, 99

—. 2015b, ApJ, 813, 99

France, K., Schindhelm, E., Bergin, E. A., Roueff, E., & Abgrall, H. 2014, ApJ, 784, 127

Fromang, S., & Nelson, R. P. 2006, A&A, 457, 343

Furuya, K., & Aikawa, Y. 2014, ApJ, 790, 97

Garaud, P., Meru, F., Galvagni, M., & Olczak, C. 2013, ApJ, 764, 146

Garmire, G., Feigelson, E. D., Broos, P., et al. 2000, AJ, 120, 1426

Garrod, R. T., & Pauly, T. 2011, ApJ, 735, 15

Gorti, U., Liseau, R., Sándor, Z., & Clarke, C. 2016, Space Sci. Rev., arXiv:1512.04622

Graedel, T. E., Langer, W. D., & Frerking, M. A. 1982, ApJS, 48, 321

Gredel, R., Lepp, S., Dalgarno, A., & Herbst, E. 1989, ApJ, 347, 289

Green, J. D., Evans, II, N. J., Kóspál, Á., et al. 2013, ApJ, 772, 117

Gressel, O., Turner, N. J., Nelson, R. P., & McNally, C. P. 2015, ApJ, 801, 84

Grevesse, N., & Sauval, A. J. 1998, Space Sci. Rev., 85, 161

Guilloteau, S., Dutrey, A., Piétu, V., & Boehler, Y. 2011, A&A, 529, A105

Güttler, C., Blum, J., Zsom, A., Ormel, C. W., & Dullemond, C. P. 2010, A&A, 513, A56

Habing, H. J. 1968, Bull. Astron. Inst. Netherlands, 19, 421

Haisch, Jr., K. E., Lada, E. A., & Lada, C. J. 2001, ApJ, 553, L153

Hartmann, L., Calvet, N., Gullbring, E., & D'Alessio, P. 1998, ApJ, 495, 385

Hawley, J. F. 2001, ApJ, 554, 534

Hayashi, C. 1981, Progress of Theoretical Physics Supplement, 70, 35

Henning, T., & Stognienko, R. 1996, A&A, 311, 291

Hogerheijde, M. R., Bergin, E. A., Brinch, C., et al. 2011, Science, 334, 338

Hollenbach, D., Kaufman, M. J., Bergin, E. A., & Melnick, G. J. 2009, ApJ, 690, 1497

Hollenbach, D. J., Yorke, H. W., & Johnstone, D. 2000, Protostars and Planets IV, 401

Hubickyj, O., Bodenheimer, P., & Lissauer, J. J. 2005, Icarus, 179, 415

Ida, S., & Lin, D. N. C. 2004, ApJ, 616, 567

Igea, J., & Glassgold, A. E. 1999, ApJ, 518, 848

Isella, A., Carpenter, J. M., & Sargent, A. I. 2010, ApJ, 714, 1746

Kama, M., Bruderer, S., Carney, M., et al. 2016a, A&A, 588, A108

Kama, M., Bruderer, S., van Dishoeck, E. F., et al. 2016b, A&A, 592, A83

Kim, H. J., Evans, II, N. J., Dunham, M. M., Lee, J.-E., & Pontoppidan, K. M. 2012, ApJ, 758, 38

Kothe, S., Güttler, C., & Blum, J. 2010, ApJ, 725, 1242

Kraus, A. L., & Ireland, M. J. 2012, ApJ, 745, 5

Landry, R., Dodson-Robinson, S. E., Turner, N. J., & Abram, G. 2013, ApJ, 771, 80

Langer, W. D., & Penzias, A. A. 1993, ApJ, 408, 539

Lee, H.-H., Herbst, E., Pineau des Forets, G., Roueff, E., & Le Bourlot, J. 1996, A&A, 311, 690

Lesur, G., Kunz, M. W., & Fromang, S. 2014, A&A, 566, A56

Lissauer, J. J., Hubickyj, O., D'Angelo, G., & Bodenheimer, P. 2009, Icarus, 199, 338

Long, F., Herczeg, G. J., Pascucci, I., et al. 2017, ArXiv e-prints, arXiv:1706.03320

Martin, R. G., Lubow, S. H., Livio, M., & Pringle, J. E. 2012, MNRAS, 423, 2718

Mathis, J. S., Rumpl, W., & Nordsieck, K. H. 1977, ApJ, 217, 425

McClure, M. K., Bergin, E. A., Cleeves, L. I., et al. 2016, ApJ, 831, 167

Meeus, G., Salyk, C., Bruderer, S., et al. 2013, A&A, 559, A84

Mendigutía, I., Brittain, S., Eiroa, C., et al. 2013, ApJ, 776, 44

Miotello, A., Bruderer, S., & van Dishoeck, E. F. 2014, A&A, 572, A96

Miotello, A., van Dishoeck, E. F., Williams, J. P., et al. 2016, ArXiv e-prints, arXiv:1612.01538

—. 2017, A&A, 599, A113

Mortier, A., Oliveira, I., & van Dishoeck, E. F. 2011, MNRAS, 418, 1194

Muzerolle, J., Calvet, N., Hartmann, L., & D'Alessio, P. 2003, ApJ, 597, L149

Öberg, K. I., Boogert, A. C. A., Pontoppidan, K. M., et al. 2011a, ApJ, 740, 109

Öberg, K. I., Guzmán, V. V., Furuya, K., et al. 2015, Nature, 520, 198

Öberg, K. I., Murray-Clay, R., & Bergin, E. A. 2011b, ApJ, 743, L16

Oliveira, I., Pontoppidan, K. M., Merín, B., et al. 2010, ApJ, 714, 778

Pérez, L. M., Carpenter, J. M., Chandler, C. J., et al. 2012, ApJ, 760, L17

Pérez, L. M., Chandler, C. J., Isella, A., et al. 2015, ApJ, 813, 41

Piso, A.-M. A., Öberg, K. I., Birnstiel, T., & Murray-Clay, R. A. 2015, ApJ, 815, 109

Pollack, J. B., Hubickyj, O., Bodenheimer, P., et al. 1996, Icarus, 124, 62

Pollack, J. B., McKay, C. P., & Christofferson, B. M. 1985, Icarus, 64, 471

Qi, C., D'Alessio, P., Öberg, K. I., et al. 2011, ApJ, 740, 84

Qi, C., Öberg, K. I., & Wilner, D. J. 2013a, ApJ, 765, 34

Qi, C., Öberg, K. I., Wilner, D. J., et al. 2013b, Science, 341, 630

Robrade, J., Güdel, M., Günther, H. M., & Schmitt, J. H. M. M. 2014, A&A, 561, A124

Salinas, V. N., Hogerheijde, M. R., Bergin, E. A., et al. 2016, A&A, 591, A122

Salmeron, R., & Wardle, M. 2008, MNRAS, 388, 1223

Schwarz, K. R., Bergin, E. A., Cleeves, L. I., et al. 2016, ApJ, 823, 91

Semenov, D., Henning, T., Helling, C., Ilgner, M., & Sedlmayr, E. 2003, A&A, 410, 611

Shakura, N. I., & Sunyaev, R. A. 1973, A&A, 24, 337

Simon, J. B., Armitage, P. J., & Beckwith, K. 2011, ApJ, 743, 17

Simon, J. B., Bai, X.-N., Armitage, P. J., Stone, J. M., & Beckwith, K. 2013, ApJ, 775, 73

Simon, J. B., Hughes, A. M., Flaherty, K. M., Bai, X.-N., & Armitage, P. J. 2015a, ApJ, 808, 180

—. 2015b, ApJ, 808, 180

Smith, R. L., Pontoppidan, K. M., Young, E. D., Morris, M. R., & van Dishoeck, E. F. 2009, ApJ, 701, 163

Soderblom, D. R., Hillenbrand, L. A., Jeffries, R. D., Mamajek, E. E., & Naylor, T. 2014, Protostars and Planets VI, 219

Stewart, S. T., & Leinhardt, Z. M. 2012, ApJ, 751, 32

Tazzari, M., Testi, L., Ercolano, B., et al. 2015, ArXiv e-prints, arXiv:1512.05679

Teague, R., Guilloteau, S., Semenov, D., et al. 2016, A&A, 592, A49

Telleschi, A., Güdel, M., Briggs, K. R., Audard, M., & Scelsi, L. 2007, A&A, 468, 443

Thommes, E. W., Duncan, M. J., & Levison, H. F. 2002, AJ, 123, 2862

Thommes, E. W., Matsumura, S., & Rasio, F. A. 2008, Science, 321, 814

Tsiganis, K., Gomes, R., Morbidelli, A., & Levison, H. F. 2005, Nature, 435, 459

Umebayashi, T., & Nakano, T. 1981, PASJ, 33, 617

—. 2009, ApJ, 690, 69

van der Wiel, M. H. D., Naylor, D. A., Kamp, I., et al. 2014, MNRAS, 444, 3911

van Dishoeck, E. F., & Black, J. H. 1988, ApJ, 334, 771

van Zadelhoff, G.-J., van Dishoeck, E. F., Thi, W.-F., & Blake, G. A. 2001, A&A, 377, 566

Visser, R., van Dishoeck, E. F., & Black, J. H. 2009a, A&A, 503, 323

Visser, R., van Dishoeck, E. F., Doty, S. D., & Dullemond, C. P. 2009b, A&A, 495, 881

Vorobyov, E. I., & Basu, S. 2015, ApJ, 805, 115

Wada, K., Tanaka, H., Suyama, T., Kimura, H., & Yamamoto, T. 2008, ApJ, 677, 1296

—. 2009, ApJ, 702, 1490

Walsh, C., Millar, T. J., Nomura, H., et al. 2014, A&A, 563, A33

Walsh, C., Loomis, R. A., Öberg, K. I., et al. 2016, ApJ, 823, L10

Weidenschilling, S. J. 1977, Ap&SS, 51, 153

Williams, J. P., & Best, W. M. J. 2014, ApJ, 788, 59

Williams, J. P., & Cieza, L. A. 2011, ARA&A, 49, 67

Windmark, F., Birnstiel, T., Ormel, C. W., & Dullemond, C. P. 2012, A&A, 544, L16

Woodall, J., Agúndez, M., Markwick-Kemper, A. J., & Millar, T. J. 2007, A&A, 466, 1197

Woods, P. M., & Willacy, K. 2009, ApJ, 693, 1360

Xu, R., Bai, X.-N., & Öberg, K. 2017, ApJ, 835, 162

Yu, M., Evans, II, N. J., Dodson-Robinson, S. E., Willacy, K., & Turner, N. J. 2017, ApJ, 841, 39

Yu, M., Willacy, K., Dodson-Robinson, S. E., Turner, N. J., & Evans, II, N. J. 2016, ApJ, 822, 53

Zsom, A., Ormel, C. W., Dullemond, C. P., & Henning, T. 2011, A&A, 534, A73

Zsom, A., Ormel, C. W., Güttler, C., Blum, J., & Dullemond, C. P. 2010, A&A, 513, A57